THEORETICAL AND NUMERICAL SIMULATION OF NON-NEWTONIAN FLUID FLOW IN PROPPED FRACTURES

A Dissertation

by

LIANGCHEN OUYANG

Submitted to the Office of Graduate and Professional Studies of
Texas A&M University
in partial fulfillment of the requirements for the degree of

DOCTOR OF PHILOSOPHY

Chairs of Committee,	Ding Zhu
Committee Members,	A. Daniel Hill
	Eduardo Gildin
	Hamn-Ching Chen
Head of Department,	A. Daniel Hill

December 2013

Major Subject: Petroleum Engineering

ABSTRACT

The flow of non-Newtonian fluids in porous media is important in many applications, such as polymer processing, heavy oil flow, and gel cleanup in propped fractures. Residual polymer gel in propped fractures results in low fracture conductivity and short effective fracture length, sometimes causing severe productivity impairment of a hydraulically fractured well. Some residual gels are concentrated in the filter cakes built on the fracture walls and have much higher polymer concentration than the original gel. The residual gel exhibits a higher yield stress, and is difficult to remove after fracture closure. But non-Newtonian fluid has complicated rheological equation and its flow behavior in porous media is difficult to be described and modeled. The Kozeny-Carman equation, a traditional permeability-porosity relationship, has been popularly used in porous media flow models. However, this relationship is not suitable for non-Newtonian fluid flow in porous media.

At first, I studied polymer gel behavior in hydraulic fracturing theoretically and experimentally. I developed a model to describe the flow behavior of residual polymer gel being displaced by gas in parallel plates. I developed analytical models for gas-liquid two-phase stratified flow of Newtonian gas and non-Newtonian residual gel to investigate gel cleanup under different conditions. The concentrated gel in the filter cake was modeled as a Herschel-Buckley fluid, a shear-thinning fluid following a power law relationship, but also having a yield stress.

Secondly, I used a combination of analytical calculations and 3D finite volume simulation to investigate the flow behavior of Herschel-Bulkley non-Newtonian fluid flow through propped fractures. I developed the comprehensive mathematical model, and then modified the model based on numerical simulation results. In the simulations, I developed a micro pore-scale model to mimic the real porous structure of flow channel in propped fractures. The correlation of pressure gradient and superficial velocity was investigated under the influence of primary parameters, such as yield stress, power law index, and consistency index. I also considered the effect of proppant packing arrangement and proppant diameter. The Herschel-Bulkley model was used with an appropriate modification proposed by Papanastasiou to avoid the discontinuity of the apparent viscosity and numerical difficulties.

DEDICATION

To my parents, wife and daughter

ACKNOWLEDGEMENTS

I would like to express my deepest gratitude to my advisors, Dr. Ding Zhu and Dr. A. Daniel Hill, for their guidance and support throughout the course of this research. As well, I would like to extend my appreciation to Dr. Eduardo Gildin and Dr. Hamn-Ching Chen for serving as my committee members.

Thanks also go to my colleagues in our research group. I also want to thank my friends and the department faculty and staff for making my time at Texas A&M University a great experience. I would like to acknowledge the financial support from the Research Partnership to Secure Energy for America, RPSEA.

Finally, thanks to my father and mother for their encouragement and to my wife for her patience and love.

NOMENCLATURE

C	Consistency factor, $Pa \cdot s^n$
d	Proppant diameter, L, m
k	Permeability, L^2, md [m^2]
L	Length of the porous media/core, L, m
m	Stress growth exponent
n	Flow behavior index, dimensionless
p	Pressure, m/Lt^2, psi [Pa]
q	Flow rate, L^3/t, bbl/min
Q	Total elastic energy, m/Lt^2, Pa
r	Distance from the center of the capillary tube/slot, L, m
R	Radius of the capillary tube/slot, L, m
R_G	Distance from interface of gas and filter cake to the center of the slot, L, m
R_{YS}	Distance from interface of yielded and unyielded zone to the center of the slot, L, m
u	Average velocity, L/t, m/s
v	Velocity, L/t, m/s
w	Fracture width, L, in. [m]
x_f	Fracture half-length, L, in.
γ	Shear rate, 1/s

ε	Strain component
μ	Fluid viscosity, m/Lt, cp [Pa-s]
π	Constant
ρ	Density, m/L^3, kg/m^3
τ	Shear stress, m/Lt^2, Pa
τ_0	Initial yield stress, m/Lt^2, Pa
ϕ	Porosity
Δ	As a prefix for difference

Subscript

G	Gas
B	Bingham
PL	Power Law
HB	Herschel-Bulkley
FC	Filter Cake
SC	Simple Cubic
BCC	Body Centered Cubic
BCC2	Body Centered Cubic with two diameters
FCC	Face Centered Cubic

TABLE OF CONTENTS

Page

LIST OF FIGURES

Page

Page

Page

Page

LIST OF TABLES

Page

CHAPTER I

INTRODUCTION

1.1 Background

One of the effective methods to satisfactory gas recovery in unconventional gas reservoirs is to create a long, conductive hydraulic fracture. Hydraulic fracturing has been studied for a long time and used widely. To create a long conductive hydraulic fracture in unconventional gas reservoirs, it is necessary to pump a large amount of viscous fluid with proppant deep into the fracture. The highly viscous fluid ensure effective proppant transportation and the proppant is used to maintain fracture widths after the hydraulic fracture closes. Fracture fluids, incorporating the complex non-Newtonian rheology, damage the proppant pack as a drawback. In additional, as water leaks off into the matrix, some gel is dehydrated, forming a filter cake on the fracture face. Filter cake can have much higher concentration than the original fracture fluid, resulting in a large yield stress. The residual gel in propped fractures exists in two forms: original gel inside the fracture and filter cake on the surface of the fracture wall. The residual gel can be difficult to clean up. It decreases gas production rate by reducing fracture conductivity and effective fracture length. After the fracture close, the residual fracturing fluid in the proppant pack is the major cause of fracture damage in tight gas reservoirs.

However, in propped fractures, the flow behavior of non-Newtonian fluid with complicated rheology is not clearly understood. Because of the complexity of problem, it requires a combination of experimental study, theoretical modeling and numerically

calculation to simulate the mechanical process of non-Newtonian fluid cleanup in propped fractures. The objectives of this research are to investigate the effects of mechanical behavior of gel cleanup, calculate conductivity that influences propped fracture performance, and develop new flow correlations of non-Newtonian fluid for industrial use. The next section will review the literature about non-Newtonian fluid cleanup in fracutures.

1.2 Literature Review

The polymer molecules are too large to invade the formation because pore sizes are small. Hence, as liquid phase leaks off, the residual gels are concentrated in the filter cakes built on the fracture walls and have much higher polymer concentration than the original gel. The residual gel concentration can be as high as 20 times the initial concentration of the original gel (Economides and Nolte, 2000). The residual gel exhibits a higher yield stress and is difficult to remove after fracture closure. It is required to model fracture fluid flow at a small scale to describe the mechanical processes of fracture cleanup and to investigate the effect of the filter cake on gas recovery in tight reservoirs.

Samuelson and Constien (1996) measured, in laboratory, fracture conductivity and residual polymer analysis for degraded fracture gel at temperatures above 180 ˚F. They provided a relationship of fracture permeability with volume of polymer recovered. The results show that fracture fluid recovery ranges from 26% to 44% depending on the breaker and other additives. The fracture fluid behaves like a solid if the pressure

gradient is below the yield stress, and residual polymer reduces the permeability and porosity of the fracture pack. The ratio of fouled fracture permeability over original permeability is related to the fraction of pore space occupied by the residual polymer.

Voneiff et al. (1996) used a commercial 2D, three-phse black-oil numerical simulator to model fracture-fluid cleanup. They presented a sensitivity analysis finding that unbroken fracture fluids can decrease gas well recoverable reserves by 30% and lower the initial gas rate by up to 80% in a tight-gas well. They concluded that the fracture gel must break to a viscosity of 50 cp or less to maximize the gas recovery. But they used Newtonian fluid properties for unbroken gel in the proppant pack.

By incorporating the yield stress concept, May et al. (1997) provided good agreement between the observed production history and numerical simulated production behavior. The effective fracture length depends on the yield stress of the fracture fluid. They showed that the relationship between the hydraulic radius in a capillary and the hydraulic radius in porous media can be shown to be:

$$R_c = \frac{D_p}{3(1-\phi)} \tag{1.1}$$

where R_c is the hydraulic radius of the capillary in meter, D_p is the particle diameter in meter and Φ is the porosity. Based on the Herschel-Bulkley model, they derived the effective viscosity, which reflects the equivalent viscosity of a non-Newtonian fluid flowing at the same velocity as its Newtonian counterpart. For multiphase problems, the effective viscosity is extended by replacing permeability with the relative permeability and porosity with the effective porosity.

$$\mu_{eff} = \frac{K'}{12}\left(9 + \frac{3}{n'}\right)^{n'} \left(150C\phi\left(S_p - S_{pirr}\right)kk_{rp}\right)^{\frac{1-n'}{2}} \tag{1.2}$$

where K is fluid consistency index in $kg \cdot s^{n-2}$, C is the tortuosity constant, S_{pirr} is the irreducible saturation for respective phase and k_{rp} is the relative permeability in m^2.

Balhoff and Miller (2005) derived an analytical model to investigate the cleanup by sensitivity analysis to determine the effect of three dimensionless parameters (reservoir to fracture mobility permeability ratio, ratio of clean to fouled and dimensionless yield stress). In their model, the fracture is split into two sections, a clean section with higher permeability and a fouled section with lower permeability. But some other authors suggest there doesn't have such interface exist. Balhoff and Thompson (2004) used a random packing to model a small part of the propped fracture. They used the network model to describe a cleanup process of a Newtonian fluid displacing a non-Newtonian fluid. The model has been coupled with a reservoir model to investigate the effect of different factors on non-Newtonian fluid cleanup. Balhoff and Thompson (2006) developed a simple network model for the flow of power-law and Ellis fluids in porous media. In the model, a parameter β, which represent the tortuosity of the porous media, was used to match the experimental data.

Yi (2004) developed an analytical Buckley-Leverett type model for displacement of non-Newtonian Herschel-Bulkley fluid by Newtonian fluid. They used this model to investigate the effect of yield stress and other rheological parameters on fracturing gel displacement efficiency. In Yi's model, the effective viscosity is described as below:

$$\mu_{eff} = \frac{K'}{12}\left(9 + \frac{3}{n'}\right)^{n'} \left(72C\phi\left(S_{nn} - S_{ir,nn}\right)kk_{rnn}\right)^{\frac{1-n'}{2}} \tag{1.3}$$

The two ancillary equations for two-phase flow are:

$$p_c = p_{ne} - p_{nn} \tag{1.4}$$

$$S_{ne} + S_{nn} = 1 \tag{1.5}$$

where p_c is the capillary pressure, p_{ne} is the pressure for Newtonian fluid, p_{nn} is the pressure for non-Newtonian fluid, S_{ne} is the saturation for Newtonian fluid and S_{nn} is the saturation for non-Newtonian fluid. As shown in **Fig. 1.1**, the effective viscosity becomes infinite at a critical non-Newtonian fluid saturation. The increasing of yield stress leads to the increasing of the critical saturation.

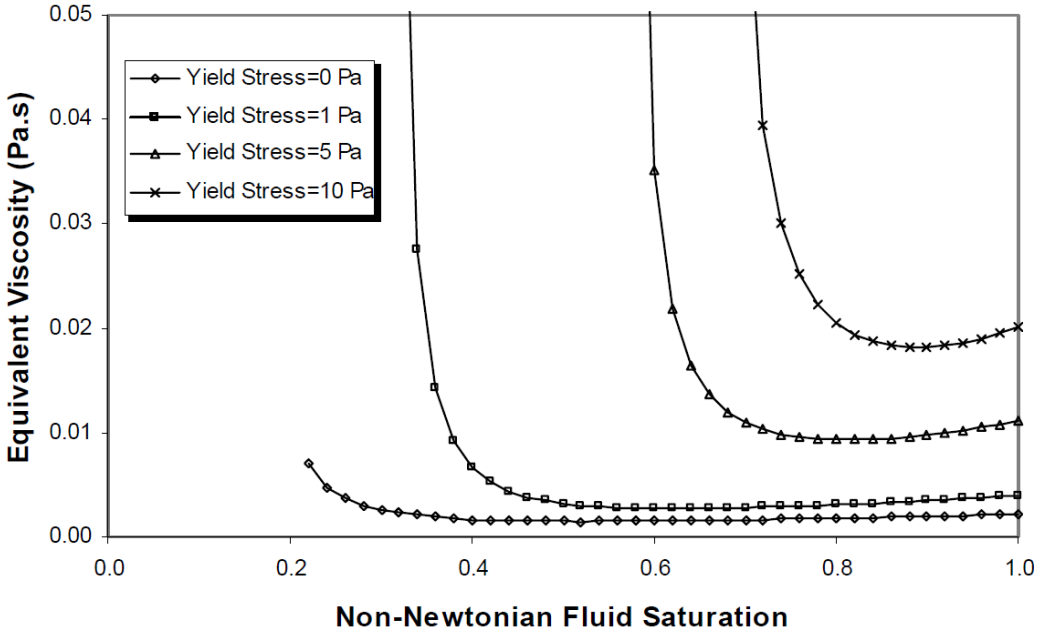

Fig. 1.1 The effective viscosity of non-Newtonian fluid (From Yi, 2004).

Other results show that high values of consistency index, yield stress and power law index lead to low displacement efficiency, and non-Newtonian fluid will not flow if the pressure gradient is smaller than a critical pressure gradient. However, the complex three-phase cleanup flow process of water, gas, and fracturing fluid cannot be accurately described using the Buckley-Leveret model.

Wang et al. (2008) incorporated Yi's model in a 3D, three-phase reservoir simulator to test the effect of reservoir permeability and pressure, fracture length and conductivity, and yield stress on fracture fluid cleanup. They investigated the effects of proppant crushing, gel residue plugging, the formation of a filter cake, and non-Darcy flow. In their opinion, insufficient fracture fluid cleanup is the major cause of the poor performance of the propped fractures. A parametric analysis indicated that only 10% of the fracture length will clean up after a year, for a non-Newtonian fracture gel with a typical value of yield stress (10 pa). From the reservoir simulation results, **Fig 1.2** shows gas saturation maps for a non-Newtonian fluid with 20 Pa after one year. The figure shows the ratio of effective fracture length over propped fracture length is very short because, for non-Newtonian fluid with yield stress, the gel doesn't move until a minimum pressure gradient in the fracture is achieved.

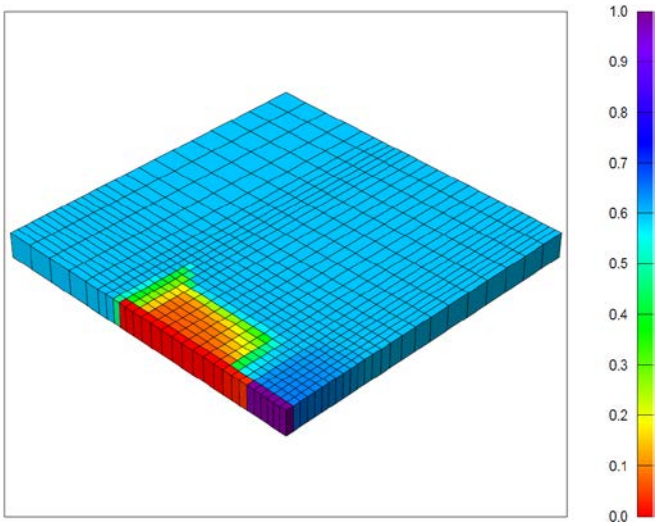

Fig. 1.2 Gas saturation map after 359 days for a non-Newtonian fluid (From Wang, 2008).

Friedel (2006) developed a non-Newtonian multi-phase fluid flow model for porous media to consider the effect of the yield stress. The author attained the tube flow velocity equation for a non-Newtonian Herschel-Bulkley fluid. The velocity profile of a Herschel-Bulkley fluid in a capillary tube is shown in **Fig. 1.3**. The characteristic feature is a plug zone in the center and a parabolic velocity profile towards the capillary walls.

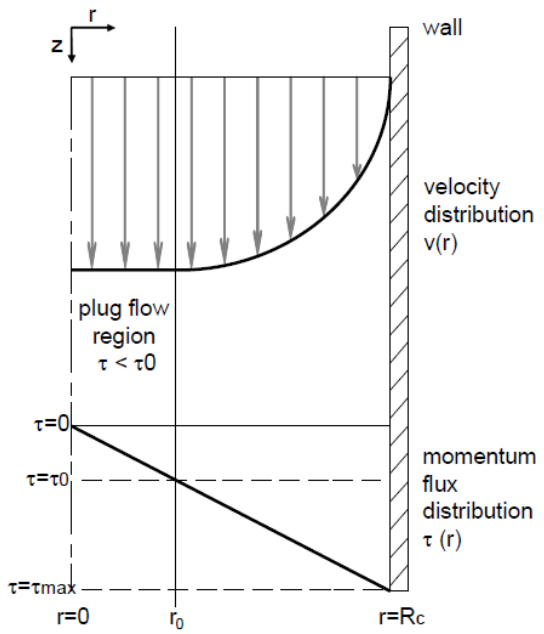

Fig. 1.3 Flow of a Herschel-Bulkley fluid in a single capillary tube. (From Friedel, 2006)

After the tube flow velocity was derived, the author tried to find a correlation ship to transform the tube flow to the porous media flow. The author first showed that the permeability of the porous media can be defined by means of the Carmen-Kozeny equation:

$$k = \frac{1}{72}\frac{\phi^3 D_p^2}{C(1-\phi)^2} \tag{1.6}$$

They also used the relationship between the hydraulic radius and the mean diameter for porous media, as shown below:

$$R_c = \frac{D_p}{3(1-\phi)} \tag{1.7}$$

By combing equations 1.6 and 1.7, the author attained the relationship of the porous-media flow and the capillary tube flow, Eq. 1.8.

$$R_c = \sqrt{\frac{8Ck}{\phi}} \tag{1.8}$$

The model has been used in a reservoir simulator and applied to typical clean up scenarios. From the reservoir simulation result, the author found that the residual gel severely decreases (typically 50%) the fracture conductivity and the production potential of a fractured well. The results show that the gel saturation has a close to linear distribution in fracture and there is no sharp interface between the residual fracturing fluid and the reservoirs fluids. This conclusion is against Balhoff and Miller's model (2005). However, in the process of deriving a non-Newtonian fluid flow model, they used the correlation of hydraulic radius and permeability for a Newtonian fluid. The misuse Newtonian fluid behavior is popular in the derivation of capillary bundle models for non-Newtonian fluid flow.

El-Khatib (2005) derived a mathematical model for power law fluid displacement in stratified reservoirs. Equationss are derived for the pseudo relative permeability as function of the average saturation. The author used the Kozeny-Carman equation directly for non-Newtonian fluids.

Ayoub et al. (2006a, b) measured the flow initiation pressure gradients by using a modified conductivity cell to allow polymer concentration via leakoff (building up the filter cake). The results highlight the crucial role played by the filter cake and show the ratio of the filter cake thickness to the fracture thickness plays a critical role in creating

significant yield stress effect. **Fig. 1.4** shows the non-Newtonian fluid doesn't move until the pressure gradient reach a flow initiation gradient of 3 psi/ft. The authors measured the flow initiation gradient in proppant packs of varying width and for different average polymer concentration. They suggested that the models used in fracturing simulators need to be modified to calculate the filter cake thickness instead of an average polymer concentration.

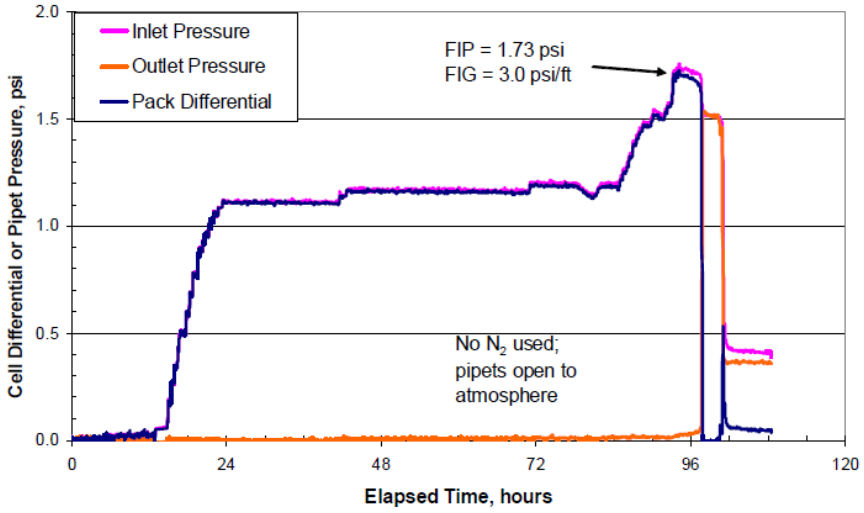

Fig. 1.4 Flow initiation of a non-Newtonian fluid (From Ayoub, 2006).

Chase and Dachavijit (2003) modified Ergun's equation (1952) to include the effect of yield stress. One parameter in their model needs to be empirically determined by experimental measure with yield stress fluids. They pumped the aqueous solutions of Carbopol 941 through a packed column of glass beads. The experiments are conducted over a range of flow rates for different concentration of Carbopol 941 to measure the

pressure drop. Their model results show that the yield stress has an important effect on the flow rate and cake growth rate.

Wang et al. (2005) measured the pressure gradient and flow rate for Zaoyuan heavy oil flow in porous media by injecting oil into the cores using a RUSKA pump. They found that Zaoyuan heavy oil has a viscoelastic property and a nonlinear viscoelasticity. The authors used the Herschel-Bulkley rheological equation to describe the heavy oil in a regression analysis method. Based on the Herschel-Bulkley model, they derived the general flow equation for steady, one-dimensional, radial flow for heavy oil. Some constants of the equation are attained from the rheological experiments. They suggested that the heavy oil experiment should be carried out under reservoir conditions to better understand heavy oil flowing in reservoirs.

Apiano et al. (2009) numerically simulated the flow behavior of non-Newtonian fluids in porous media. They studied the flow behavior of power-law fluid and Bingham fluid through three dimensional disordered porous media. They used modified permeability-like index and Reynolds number to describe the flow equation of power-law fluid. For Bingham fluids, they concluded that pore structure, yield stress and inertia would generate a combined condition of “enhanced flow”. However, the range of the yield stress was between 0.01 and 1 Pa, which is very small.

1.3 Problem Description

Hydraulic fracturing is one of the most effective and commonly used methods to enhance recovery in tight gas reservoirs. The key to producing gas from tight gas

reservoirs is to create a long, highly conductive hydraulic fracture to stimulate flow from the reservoir to the wellbore. To maintain conductivity in a fracture, it is important to pump sufficient quantities of propping agent into the fracture. In fracturing treatments, to evenly distribute proppant deeply into the fracture, we use fracture fluid with polymer which has high viscosity. However, these fracture fluids need to be cleaned up after the treatment. During the procedure of propped fracturing treatment, it is critical to ensure the effectiveness of the gel cleanup.

Residual polymer in the fracture can reduce the effective fracture permeability and porosity. In fact, if one computes effective fracture length of most wells, it is found that the effective length is less than the designed propped fracture length. The effective fracture length is often 10% to 50% of the propped fracture length. **Fig. 1.5** shows a common phenomenon in fracture treatment. Although we have a long created fracture length, the propped length is shorter than created length, because the proppant cannot reach the tip of the fracture. Due to high viscosity of fracture fluids, sometime it is difficult to flow fracture fluid back. This causes less effective fracture length.

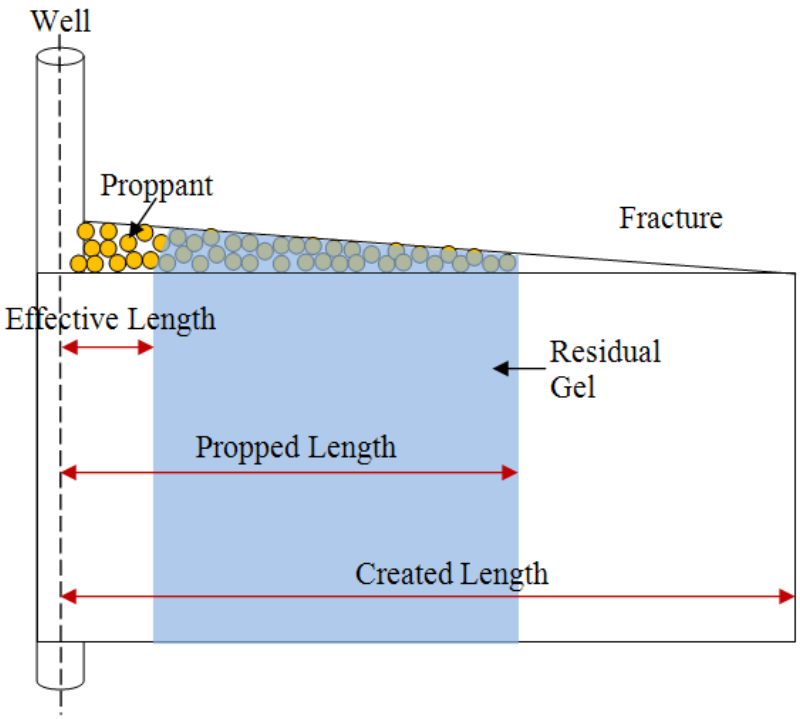

Fig. 1.5— The schematic of propped fracture.

Gel damage is a complex problem combining proppant pack damage inside fracture, filter cake deposition at the fracture walls, and fracture fluid invasion in the near-fracture formation. To understand the mechanism of gel damage, some lab experiments have focused on identifying the critical factors that result in low productivity after treatment. **Fig. 1.6** shows residual gel left in proppant pack after 35 ppt Carboxymethyl Hydroxypropyl Guar (CMHPG) with breaker in the conductivity cell after measuring long term conductivity. The white balls are proppants. **Fig. 1.7** shows the filter cake build on the fracture face after flowing 35 ppt CMHPG fluid during the fracture stimulation. As the liquid leaks into the matrix, the gel forms a filter cake on the fracture face. The filter cake can have much high polymer concentration than the

original fracture fluid, so the filter cake has a larger yield stress and viscosity, and therefore more difficulty to be cleaned up. They show that the majority of the damage are caused by residual gel and the filter cake that act to diminish the pack width and permeability of propped fracture.

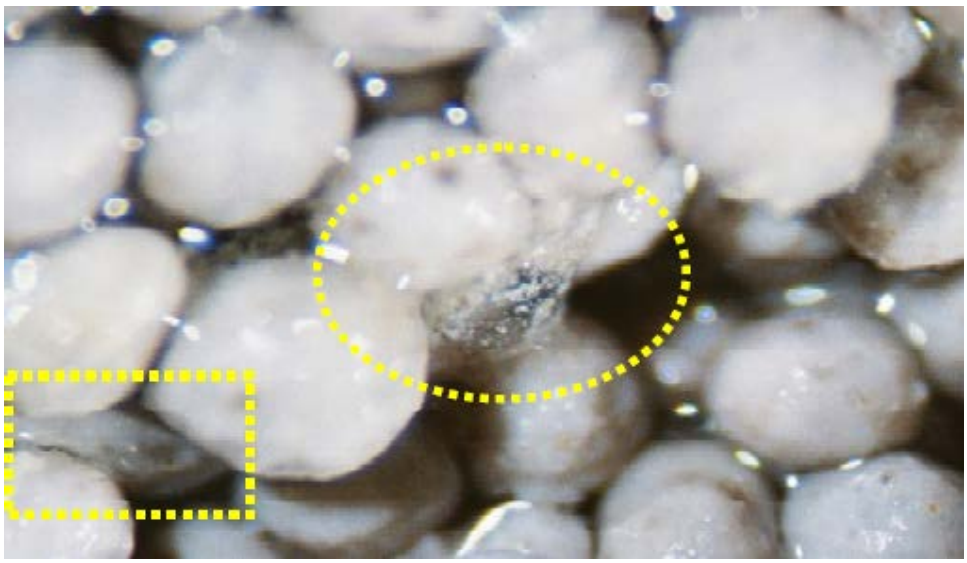

Fig. 1.6– Residual gel between proppants in conductivity cell (Palisch, T., Duenckel, R., and Bazen, L., 2007).

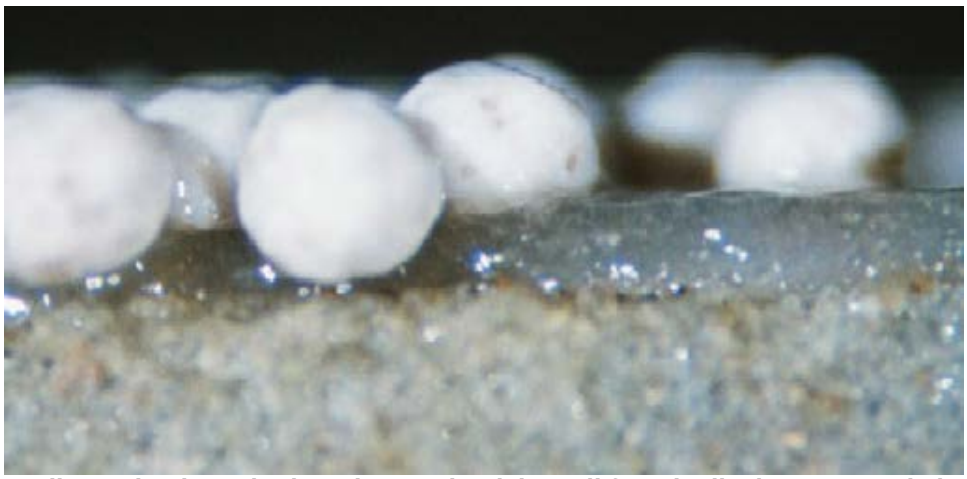

Fig. 1.7– Filter cake deposited on the conductivity cell face (Palisch, T., Duenckel, R., and Bazen, L., 2007).

The physical flow phenomenon of gel invasion in porous media is very complex and cannot be easily described in laboratory experiments. There is also evidence that before gel in a fracture can flow, a yield stress must be exceeded. Both of the complicated rheological behavior of gel and the pore structure in porous media post a challenge in modeling gel clean up. Some current research works used the correlation for Newtonian fluid in the mathematical model development of non-Newtonian fluid flow in porous media. This will lead to a misunderstanding for flow physical behavior and mis-prediction for gel cleanup effectiveness, propped fracture length and gas production. Thus, current models are not accurate at estimating propped fracture performance. If we can rigorously mathematically model and numerically simulate the physics of polymer behavior inside the fracture and better understand the problems, we can develop new methods for creating extensive, high conductive hydraulic fractures and accelerate the cleanup process for improved gas production in unconventional gas reservoirs.

1.4 Objectives

The objective of the research is to investigate the flow behavior of residual gel in propped fractures and develop mathematical models of non-Newtonian fluid flow to predict fracture conductivity. The cleanup of fracture fluids is a critical issue for propped fracture treatment, but it is difficulty to be understood. That is because the combination of complex flow channel of gels in propped fractures and the highly non-linear rheological behavior of fracture gel. The new fracture fluid cleanup models in low-permeability gas well fracturing will help for developing novel systematic treatment

design procedures to develop the next generation of hydraulic fracturing technology for these reservoirs.

In the first part of the research, the research work in this dissertation investigates mechanical process of the filter cake cleanup between two parallel cores. In this work we study polymer gel behavior in hydraulic fracturing theoretically and experimentally to describe the effect of the yield stress. We develop a mathematical model to describe the flow behavior of residual polymer gel being displaced by gas in parallel plates. A develop analytical model is developed for gas/liquid two-phase stratified flow of Newtonian gas and non-Newtonian residual gel to investigate gel cleanup under different conditions. The concentrated gel in filter cakes can be modeled as a Herschel-Bulkley fluid, a shear-thinning fluid following a power law relationship, but also having a yield stress. The parameters for the gel displacement model are evaluated by the experimental study. Based on the mathematical model, the critical flow back velocity is calculated, and then compared with the experimental result (Yango 2011).

The second part of the project studies the flow behavior of Herschel-Bulkley fluid in porous media at pore scale. We first model single-phase non Newtonian fluid flow through porous media. Combing with the analytical calculation, the mathematical model for describing the flow rate of Herschel-Bulkley fluid in porous media was attained. We investigated non-Newtonian fluid displacement by Newtonian fluid in porous media. By Computational Fluid Dynamics (CFD), we develop correlations of the flow velocity of non-Newtonian fluid as a function of the pressure gradient, the property of porous media and the rheological parameters of Herschel-Bulkley fluid. The models

have simple forms and can be easily incorporated into reservoir simulator to evaluate the effect of gel damage on gas production in unconventional reservoir. With the model, we can study the distributions of permeability along propped fracture.

The complexity of the numerical simulation lies in irregular flow channel and the instability of iteration. For such complicated structure of flow channel in propped fracture, it is difficult to generate a grid system and calculate a large amount of grids on computers. Reasonable simplifications for physical geometry of flow channel were made and appropriate boundary conditions were introduced for computational domain. GAMBIT, a pre-processing software package, was used to generate the grid system. FLUENT was used for numerical simulation. The instability of numerical iteration is caused by the complex rheological behavior of Herschel-Bulkley fluid. A modified Herschel-Bulkley model in FLUENT was used to enhance the stability of the numerical simulation.

In summary, the objectives of the research are:

1) Develop a mathematical model for filter cake clean up between two parallel cores.
2) Establishing a Computational Fluid Dynamics model to simulate non-Newtonian fluid flow behavior in porous media with realistic pore structure.
3) Examining the effects of key factors on the flow rate of non-Newtonian fluid, such as pressure gradient, yield stress, consistency index, power law index, proppant diameter and proppant packing arrangement way.

4) Developing a theoretical model of non-Newtonian fluid clean up in propped fractures to match the numerical stimulation result.

CHAPTER II

FILTER CAKE DISPLACEMENT*

2.1 Introduction

In propped fractures, residual polymer gel causes fracture fluid damage and lead to lower fracture conductivity and shorter effective fracture length. In the worst situation, it severely reduces the production rate. Some residual gels are concentrated in the filter cakes deposited on the fracture walls. The filter cake has much higher polymer concentration than the original gel, resulting in a higher yield stress, and is difficult to remove. It is difficult to understand, observe and describe the flow behavior of the filter cake in propped fractures. This problem is studied from a simplification: filter cake flow between two parallel cores without proppant. Although this is a simple case comparing with the reality, it makes us possible to study the effect of the yield stress of the filter cake. The results of the micro scale experiment and the corresponding model can be used in the reservoir simulator in the future.

The analytical solution to the problem has been fully studied and derived. Some basic concepts of the flow behavior of non-Newtonian fluid were attained from the derivation. The rheological behavior of the filter cake can be described by Herschel-Bulkley model having a yield stress. The yield stress of this material is a critical parameter influencing whether the gel can be removed from the fracture. From the finding of the experimental study (Yango 2011), a model was developed to describe the

* Reproduced with permission from "Theoretical and Experimental Modeling of Residual Gel Filter Cake Displacement in Propped Fractures" by Ouyang, L., Yango, T., Zhu, D. and Hill, A.D. 2011. *SPE Productoin & Operations*. Volume 27, Issue 4, Pages 363-370. Copyright 2011 by Society of Petroleum Engineers.

flow behavior of residual polymer gel being displaced by gas in parallel plates. Because of this specific nature of the Herschel-Bulkley, it usually has a solid or plug-like flow at some particular area. An analytical model for gas-liquid two-phase stratified flow of Newtonian gas and non-Newtonian residual gel was used in order to investigate gel cleanup under different conditions. The model developed shows that three flow regimes may exist in a slot, depending on the gas flow rate and the filter cake yield stress. At low gas velocities, the filter cake will be completely immobile. At higher gas velocity, the shear at the fracture wall exceeds the yield stress of the filter cake, and the gel is mobile, but with a plug flow region of constant velocity near the gas-gel interface. Finally, at high enough gas velocity, a fully developed velocity field in the gel is created.

2.2 Modeling Filter Cake Cleanup in Parallel Plates

The filter cake deposits on the surfaces of the fracture and the original gel occupies the center of the slot. Compared to the filter cake, the original gel has a much lower yield stress and is easier to clean up. If the pressure drop along the fracture is not large enough, the original gel will be cleaned up and the filter cake will be left on the surface of the rock. Thus, only gas flows between two filter cake surfaces. Otherwise, if the pressure drop is higher than a critical value, the filter cake will initiate flow. In this situation, there is two-phase stratified flow of Newtonian gas and non-Newtonian filter cake.

2.2.1 Shear Stress Distribution in Parallel Plates

To compare the modeling result with the experimental study, a similar domain is used to imitate a modified API fracture conductivity cell. The length of the test cell is 7 inches and the height is 1.61 inches. The fracture width is set to 0.25 inches. So the flow domain has a dimension of 7″×1.61″×0.25″. It is reasonable to reduce the flow to a two dimensional problem. The schematic of the force balance on a small fluid element in slot flow is shown in **Fig. 2.1**.

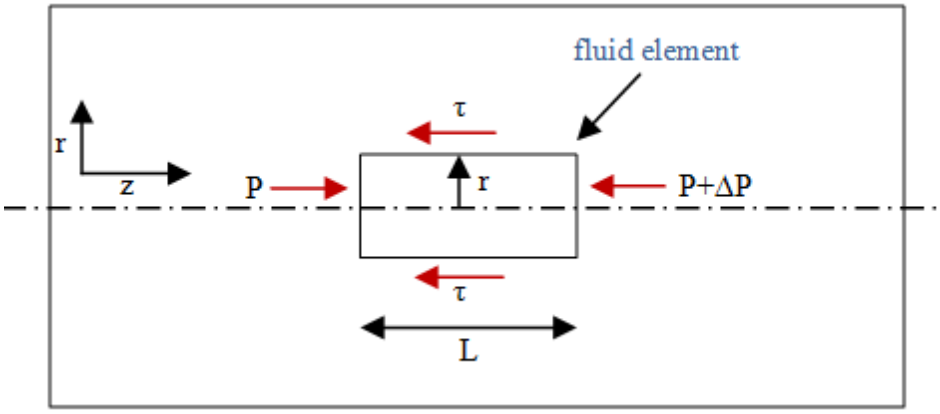

Fig. 2.1—The force balance on the fluid element in slot flow.

The equation for force balance in the z-direction on a small fluid element located at the distance, *r*, from the center can be written as:

$$p \cdot 2r = (p + \Delta p)2r + 2\tau L \qquad (2.1)$$

where the shear stress distribution is written as:

$$\tau = \frac{-\Delta p}{L} r \tag{2.2}$$

This equation can be used for laminar or turbulent flow, Newtonian or Non-Newtonian fluid, because it is only based on the force balance law and no additional assumptions have been made.

2.2.2 Rheology of Fracturing Fluid

To effectively carry proppant into the fracture, fracture fluids typically contain water-soluble gel that creates high viscosity. Guar gums and its derivatives are commonly used polymers for this purpose. The rheological behavior of the fracture fluid and the concentrated polymer filter cakes can be represented by non-Newtonian fluid.

Newtonian fluids have a direct linear proportionality between shear stress τ and shear rate γ.

$$\tau = \mu\gamma \tag{2.3}$$

where μ is the constant viscosity. Newtonian fluids have shear and time independent viscosity, but it might be impacted by other physical parameters, such as temperature and pressure. For a Newtonian fluid, the graph of shear stress versus shear rate is a straight line through the origin point.

Non-Newtonian fluids do not follow the linear relationship between shear stress and shear rate, due to nonlinearity or initial yield stress. Two of the most characteristic features of non-Newtonian fluid behavior are: viscosity depends on the shear rate and yield stress which requires a critical shear stress before the fluid can start to flow. The

generic rheological behavior of the non-Newtonian fluids is shown in **Fig. 2.2**. The figure presents rheological behavior of shear thinning, shear thickening and shear independent fluids, each with or without initial yield stress.

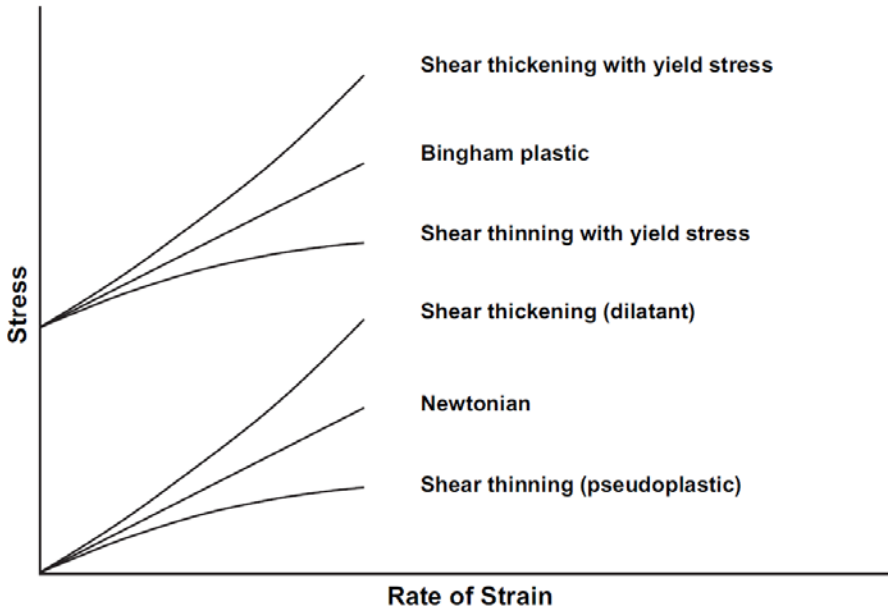

Fig. 2.2—Some typical rheological behavior of non-Newtonian fluids.

The power-law model is used to describe shear-thinning or shear-thickening behavior. The model is

$$\tau = C\gamma^n \tag{2.4}$$

where C is the consistency factor and n is the flow behavior index. For shear-thinning fluid (n<1), the viscosity decreases on decreasing shear rate.

Bingham model is for a fluid with a yield stress. The rheological equation of the Bingham model is shown by:

$$\tau = \tau_0 + \gamma \tag{2.5}$$

where τ_0 is the initial yield stress. The yield stress depends on surface property of the polymer, concentration of the polymer, and types of the ions in the fluid phase. The yield stress can decrease by some chemical treatment to break the bond valences or precipitate the cations. If the fluid has an initial yield stress, the flow unlikely happens across the entire domain. That is because, at certain specific zone, the shear stress is not larger enough to overcome the threshold value.

The Herschel-Bulkley model has both of the characteristic feature of power-law fluid and Bingham fluid. By choosing appropriate value for its three parameters, the Herschel-Bulkley model can describe the Newtonian and most of time-independent non-Newtonian fluid. The equation for the Herschel-Bulkley fluid is shown below:

$$\begin{cases} \gamma = 0 & |\tau| < \tau_0 \\ \gamma = \left(\dfrac{\tau - \tau_0}{C} \right)^{1/n} & |\tau| \geq \tau_0 \end{cases} \tag{2.6}$$

where τ_0 is the yield stress above which the fluid starts to flow, C is the consistency factor and n is the flow behavior index. The Herschel-Bulkley model reduces to the power-law model when $\tau_0 = 0$, to the Bingham model when $n = 1$, and to the Newtonian fluid when both of two conditions are satisfied.

The rheological behavior of the fracture fluid and the concentrated polymer filter cakes can be described by Herschel-Bulkley model. When pumping the slurry into the fracture, assuming that only the liquid phase can invade into the rock porous space, after leak off, the polymer concentration is higher. The concentrated gel deposited on the

fracture wall is called filter cake to distinguish it from the original gel. The rheology of the filter cake can be described by the Herschel-Bulkley model. The Herschel-Bulkley fluid element will have a shear rate only if the applied stress exceeds the yield stress. This means that there will be a solid plug-like core flowing or station and where the shear stress is smaller than the yield stress. The situation of the plug depends on the shear stress distribution. The yield stress of this model is a critical parameter that determines whether or not the fluid can be cleanup from the fractures.

2.2.3 Flow Equations under Different Physical Conditions

The general expression for the filter cake velocity profile can be obtained by combining the shear stress distribution equation in channel, Eq. 2.2, with the Herschel-Bulkley fluid's rheological equation, Eq. 2.6 with rearranging and integrating

$$\begin{cases} v_{HB}(r) = c_1 & |\tau| < \tau_0 \\ v_{HB}(r) = -\dfrac{(Ar-B)^{1+\frac{1}{n}}}{A\left(1+\dfrac{1}{n}\right)} + c_2 & |\tau| \geq \tau_0 \end{cases} \tag{2.7}$$

and

$$A = \frac{-\Delta p}{CL}, \qquad B = \frac{\tau_0}{C} \tag{2.8}$$

where C is the consistency factor of the filter cake. The constants c_1 and c_2 are determined by the boundary conditions.

There may exist three flow patterns in a slot, depending on the shear condition. At low pressure gradients (case 1), the value of the shear stress through the filter-cake

region is smaller than the yield stress. The filter cake is completely immobile and gas flows only between the two filter cakes, as seen in **Fig. 2.3**.

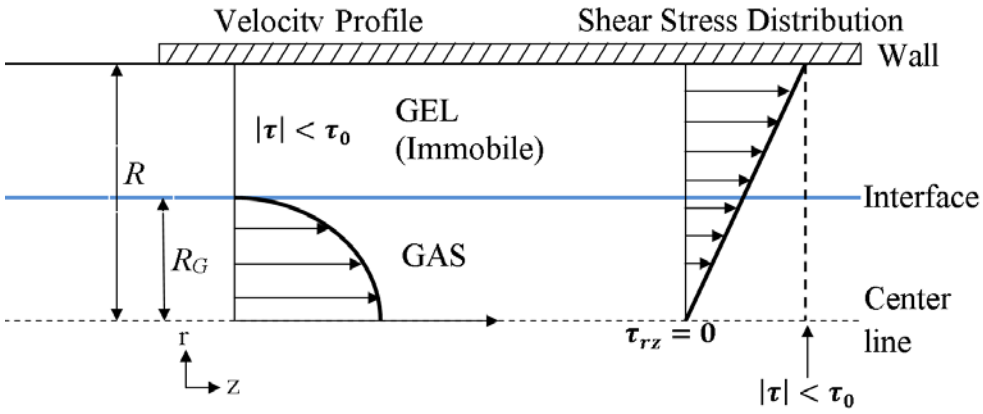

Fig. 2.3—Flow pattern for case 1 (Low pressure gradient).

The equation for gas velocity profile can be obtained by combining the shear stress distribution equation in channel, Eq. 2.2, with the Newtonian fluid's rheological equation, Eq. 2.3, rearranging it, and integrating. The equation for gas velocity profile is shown below:

$$v_G(r) = \frac{\Delta p}{L}\frac{1}{2\mu}r^2 - \frac{\Delta p}{L}\frac{1}{2\mu}R_G^2 \qquad (2.9)$$

where $\frac{\Delta p}{L}$ is the pressure gradient along the conductivity core (in Z direction), μ is the viscosity of Newtonian fluid, and R_G is the distance from the center line to the interface of Newtonian fluid (gas) and non-Newtonian fluid (filter cake).

For Case 1, the filter cake does not flow because the shear stress in the filter cake domain is smaller than the initial yield stress. The maximum shear stress occurs at the surface of the conductivity core. So the physical condition for case 1 is

$$-\frac{\Delta p}{L} < \frac{\tau_0}{R} \tag{2.10}$$

At moderate pressure gradients (Case 2), the shear stress is equal to the yield stress at some position in the filter cake region, R_{YS}, as seen in **Fig. 2.4**.

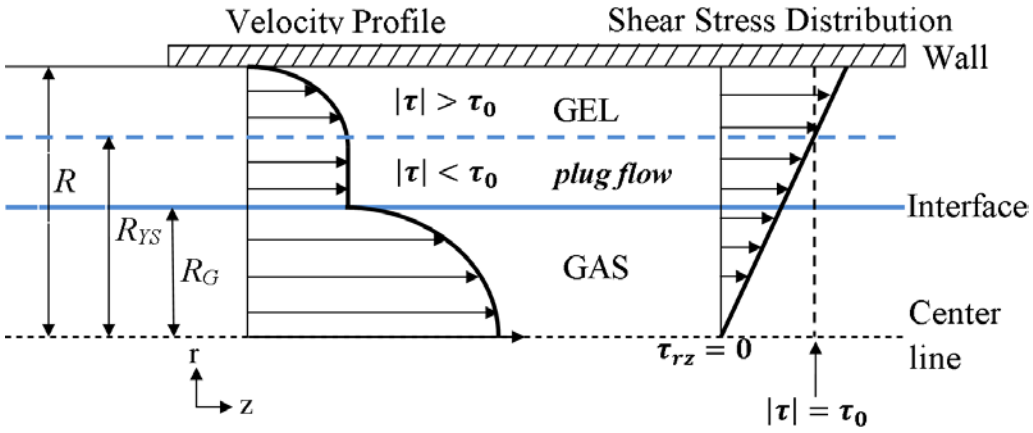

Fig. 2.4—Flow pattern for case 2 (Moderate pressure gradient).

Because shear stress increases linearly with increasing distance from the center of the slot, shear stress is larger than initial yield stress in the region of $R_{YS} < r < R$. This causes deformation of the filter cake in this area. In the region $R_G < r < R_{YS}$, the shear stress is smaller than the yield stress, so the shear rate is zero according to the specific feature of the rheological behavior of the Herschel-Bulkley fluid. This means that the gel

in this region is like a "solid". In other word, the filter cake keeps still or has a uniform velocity. Because the boundary condition of the velocity should be continuous at the interface of the filter cake and gas, the filter cake has a constant velocity. Hence, the velocity of the filter cake gradually increases from zero at the surface of the cell to a constant solid-plug velocity near the gas/gel interface. The situation that the shear stress is equal to the initial yield stress, R_{YS}, is determined.

$$R_{YS} = \frac{\tau_0 L}{-\Delta p} \tag{2.11}$$

The filter cake velocity profile within the region $R_{YS} < r < R$ can be obtained by solving Eq. 2.7 with the no-slip boundary condition at the surface of the conductivity core. So the velocity profile of the filter cake in this region is present below:

$$v_{HB}(r) = -\frac{(Ar - B)^{1+\frac{1}{n}}}{A\left(1+\frac{1}{n}\right)} + \frac{(AR - B)^{1+\frac{1}{n}}}{A\left(1+\frac{1}{n}\right)} \tag{2.12}$$

For the region $R_G < r < R_{YS}$, the constant plug velocity can be obtained by the velocity continuity condition. Because the plug-like gel has a constant velocity, the velocity at the interface of two phases is the same as at interface of the yielded and unyielded in gel zone, as shown in Eq. 2.13.

$$\frac{\Delta p}{L}\frac{1}{2\mu}R_G^2 + c = -\frac{(AR_{YS} - B)^{1+\frac{1}{n}}}{A\left(1+\frac{1}{n}\right)} + \frac{(AR - B)^{1+\frac{1}{n}}}{A\left(1+\frac{1}{n}\right)} \tag{2.13}$$

So the velocity profile for the gas is present as below:

$$v_G(r)=\frac{\Delta p}{L}\frac{1}{2\mu}r^2-\frac{\Delta p}{L}\frac{1}{2\mu}R_G^2-\frac{(AR_{YS}-B)^{1+\frac{1}{n}}}{A\left(1+\frac{1}{n}\right)}+\frac{(AR-B)^{1+\frac{1}{n}}}{A\left(1+\frac{1}{n}\right)} \tag{2.14}$$

The velocity profile for the filter cake is shown as below:

$$v_{HB}(r)=\begin{cases}-\dfrac{(AR_{YS}-B)^{1+\frac{1}{n}}}{A\left(1+\frac{1}{n}\right)}+\dfrac{(AR-B)^{1+\frac{1}{n}}}{A\left(1+\frac{1}{n}\right)}, & |\tau|\le\tau_0\\ -\dfrac{(Ar-B)^{1+\frac{1}{n}}}{A\left(1+\frac{1}{n}\right)}+\dfrac{(AR-B)^{1+\frac{1}{n}}}{A\left(1+\frac{1}{n}\right)}, & |\tau|>\tau_0\end{cases} \tag{2.15}$$

By integrating the velocity profile within two flow regions, the average velocity of the filter cake through a slot can be obtained, as in Eq. 2.16. The details are in Appendix A.

$$\bar{u}_{HB}=\frac{(AR-B)^{1+\frac{1}{n}}}{A\left(1+\frac{1}{n}\right)}-\frac{(AR-B)^{2+\frac{1}{n}}}{A^2\left(1+\frac{1}{n}\right)\left(2+\frac{1}{n}\right)(R-R_G)} \tag{2.16}$$

Similarly, mean gas velocity can be obtained by integrating Eq. 2.14 within the domain.

$$\bar{u}_{GAS}=-\frac{1}{3}\frac{\Delta p}{L}\frac{R_G^2}{\mu_{gas}}+\frac{(AR-B)^{1+\frac{1}{n}}}{A\left(1+\frac{1}{n}\right)} \tag{2.17}$$

For the Case 2, in some part of the filter cake, the shear stress is larger than the initial yield stress; in the other part, the shear stress is smaller than the yield stress. So the shear condition for Case 2 is

$$\frac{\tau_0}{R} < -\frac{\Delta p}{L} < \frac{\tau_0}{R_G} \tag{2.18}$$

Finally, in Case 3, the pressure gradient is high enough that the shear stress through the filter cake domain is greater than the initial yield stress. The velocity field of the filter cake is fully developed, as shown in **Fig. 2.5**. There is no any solid-like flow in the filter cake.

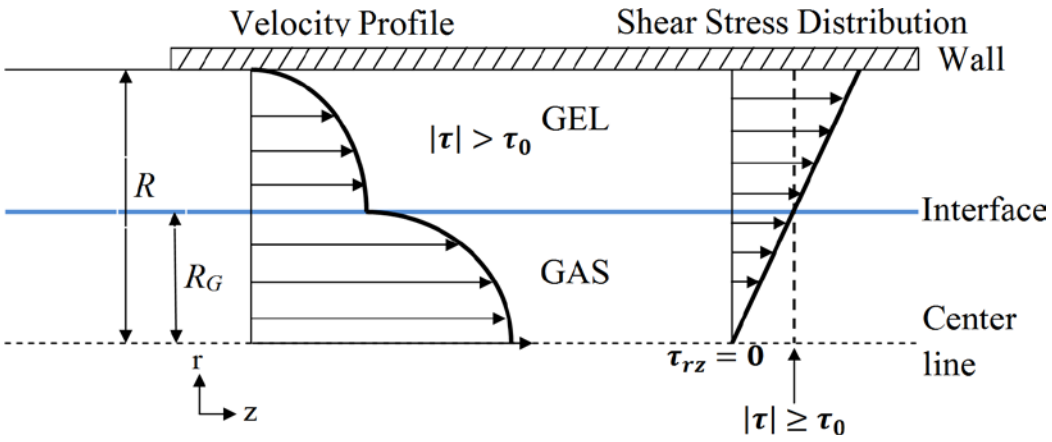

Fig. 2.5—Flow pattern for case 3 (High pressure gradient).

Similarly, we can get the filter cake velocity and the gas velocity profiles by solving the general expression for filter cake and gas velocity with the velocity continuity condition at the gel/gas interface.

So the velocity profile for gas is present as below:

$$V_G(r) = \frac{\Delta p}{L}\frac{1}{2\mu}r^2 - \frac{\Delta p}{L}\frac{1}{2\mu}R_G^2 - \frac{(AR_{YS} - B)^{1+\frac{1}{n}}}{A\left(1+\frac{1}{n}\right)} + \frac{(AR - B)^{1+\frac{1}{n}}}{A\left(1+\frac{1}{n}\right)} \tag{2.19}$$

The velocity profile for filter cake is shown as below:

$$v_{HB}(r) = -\frac{(Ar-B)^{1+\frac{1}{n}}}{A\left(1+\frac{1}{n}\right)} + \frac{(AR-B)^{1+\frac{1}{n}}}{A\left(1+\frac{1}{n}\right)} \tag{2.20}$$

By integrating velocity profile equations, Eqs. 2.19 and 2.20, within their domain, the mean velocities for gas and filter cake are shown in Eq. 21 and Eq. 22 separately.

$$\overline{u}_{GAS} = -\frac{1}{3}\frac{\Delta p}{L}\frac{R_G^2}{\mu_{gas}} + \frac{(AR-B)^{1+\frac{1}{n}}}{A\left(1+\frac{1}{n}\right)} - \frac{(AR_G-B)^{1+\frac{1}{n}}}{A\left(1+\frac{1}{n}\right)} \tag{2.21}$$

and

$$\overline{u}_{HB} = \frac{(AR-B)^{1+\frac{1}{n}}}{A\left(1+\frac{1}{n}\right)} + \frac{(AR_G-B)^{2+\frac{1}{n}}}{A^2\left(1+\frac{1}{n}\right)\left(2+\frac{1}{n}\right)(R-R_G)} - \frac{(AR-B)^{2+\frac{1}{n}}}{A^2\left(1+\frac{1}{n}\right)\left(2+\frac{1}{n}\right)(R-R_G)} \tag{2.22}$$

If the Reynolds number for gas flow is larger than 4000, Eqs. 2.17 and 2.21 are not appropriate for calculating the mean gas velocity. We need to use an empirical turbulent flow expression to calculate the average gas velocity.

For the Case 3, the shear stress in all filter cake domain is greater than the initial yield stress. The shear condition for Case 3 is

$$-\frac{\Delta p}{L} > \frac{\tau_0}{R_G} \tag{2.23}$$

After combining the shear stress distribution equation in a channel with the Herschel-Bulkley fluid's rheological equation, with the appropriate boundary conditions,

we get the expression for the velocity profile and the flow rate. The model developed shows that three flow regimes may exist in a slot, depending on the pressure gradient and the filter cake yield stress.

2.3 Model Validation

The model developed was validated by the experimental work conducted by Yango (Yango, 2011). The experiment set up and flow condition was simulated by the analytical model presented in the previous section. The experiments were conducted on a core sample with a dimension of 7 in. by 1.61 in., as shown in **Fig. 2.6**. The cores were from Kentucky sandstone and its permeability is about 0.1 md. The fracture set in between two cores is 0.25 in. in width.

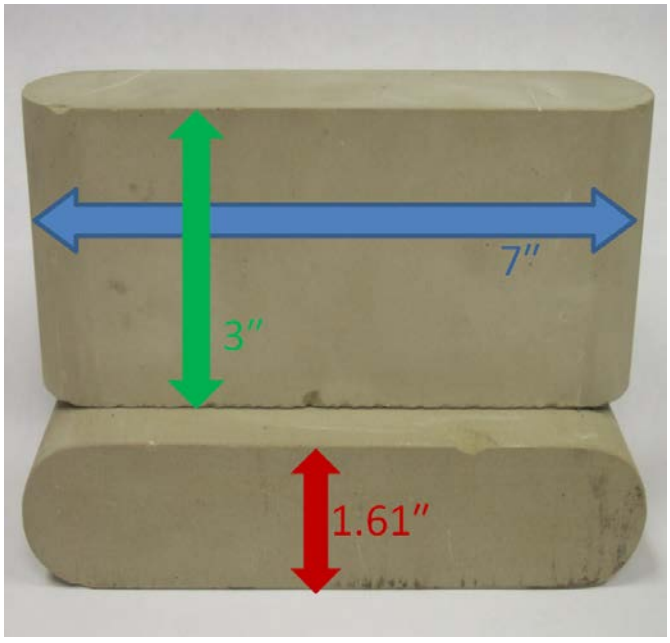

Fig. 2.6—A conductivity cell sample in laboratory (Yango, 2011).

Yango (2011) built up the filter cake on the surface of the conductivity cores at first, and then run the filter cake cleanup experiment. To build up the filter cake, a 40 lb/Mgal guar borate crosslinked gel was mixed and pumped through a modified API RP-61 cell using a hydracell diaphragm pump. The parameters used in the experiments, and also in the model calculation are presented in **Table 2.1**. More detail about the process of the buildup and cleanup experiment can be found in Yango (2011).

TABLE 2.1—CLEANUP TEST DATA	
Fracture Width, in	0.25
Flow Rate during Leak off, ml/s	6.08
Shear Rate, s^{-1}	20.71
Leak off Time, min	94
Leak off Volume, ml	177.49
Filter Cake Thickness, mm	*1.1474*
Filter Cake Concentration, lb/Mgal	*748*
Yield Stress, Pa	*296*
Leak off Coefficient, $ft/min^{0.5}$	0.0032

Fig. 2.7, from Yango's work, displays what happen in the fracture in the cleanup experiment. Fig. 2.7a is the filter cake buildup after leak off. We can see there are full of the original gel between two cores. In fact, there has the filter cake on the core face, but is covered by the original gel. Fig. 2.7b-e show that the process of the filter cake has been removed from the fracture when the water flow rate was increased in steps from 25 ml/s to 62 ml/s. Based on our experiment results, the critical flow rate for the referenced clean up experiments is estimated between 55 ml/s to 62 ml/s.

(a)

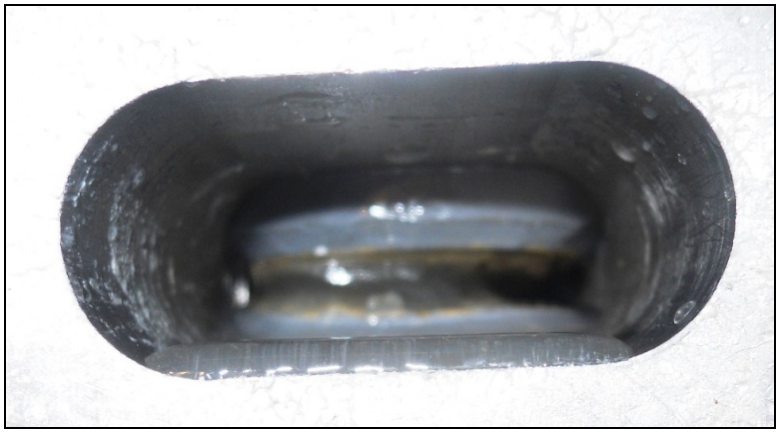

(b)

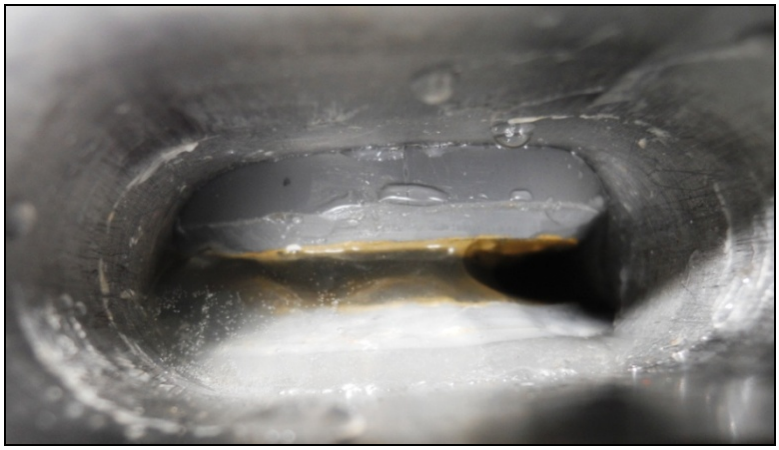

(c)

Fig. 2.7—Filter cake cleanup result for the experiment. (a) Before cleanup. (b) Flow rate 25 ml/s. (c) Flow rate 40 ml/s. (d) Flow rate 50 ml/s. (e) Flow rate 62 ml/s.

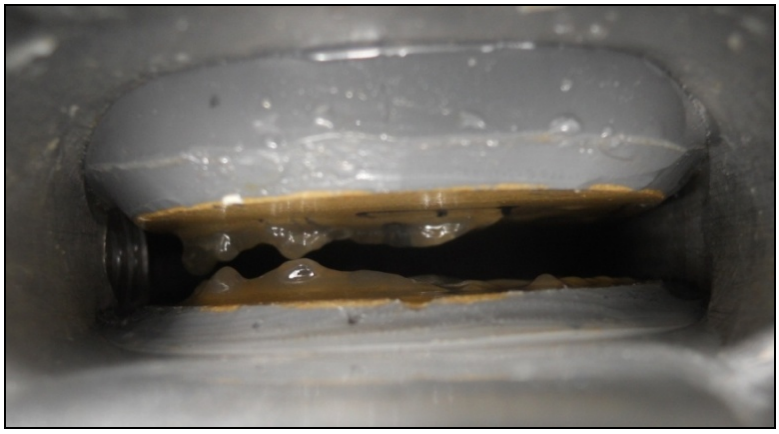

(d)

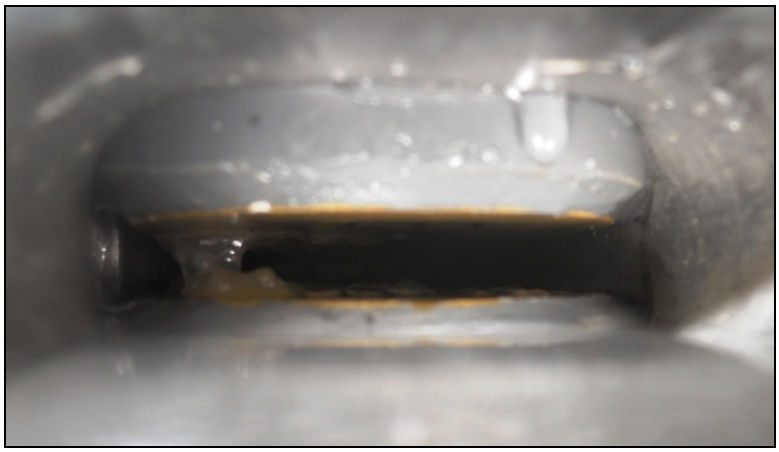

(e)

Fig. 2.7—Continued.

We used our model to calculate the initial yield stress of filter cake based on the critical flow rate obtained from the experiment. Then, we used the yield stress to calculate the filter cake concentration by Xu's correlation (2011), and compared with the concentration result from the experiment.

From the experiment, the critical water flow rate for filter cake cleanup is estimated at 55 ml/s to 62 ml/s. We chose 60 ml/s to use our model to calculate the filter cake concentration. The filter cake thickness is not a constant along the cell length

direction. **Fig. 2.8** shows a picture of actual filter cake in the experiment after cleanup the original gel. The velocity is higher at the locations that have thicker filter cake because the volumetric flow rate is the same through the cell. This means that the pressure gradient at the thicker filter cake locations is higher than at other parts of the fracture. We chose the higher thickness condition in our calculation. For the water flow rate of 60 ml/s, the Reynolds number is 2600 if simply using the mean thickness to calculate the velocity; or higher than 4000 if using the highest thickness. Turbulent flow occurs in this cleanup experiment. Therefore, we used the turbulence flow model to calculate the pressure drop. After algebraic manipulation, the filter cake has an estimated concentration of 458 lb/Mgal based on our model comparing with 748 lb/Mgal from the experiment.

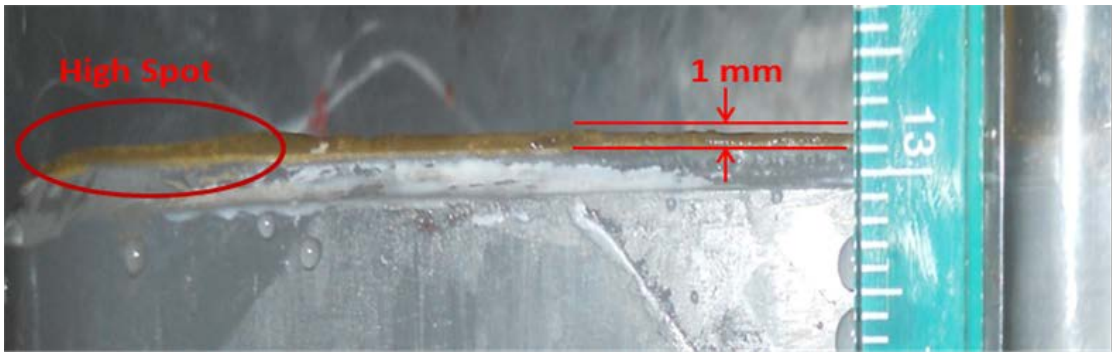

Fig. 2.8-Uneven filter cake thickness along the core sample.

In this chapter, we have developed a model that can be used to calculate the critical flow rate to initiate filter cake flow and found that there might exist three possible flow patterns. The pressure gradient, fracture width, the filter cake thickness,

rheological parameter of the filter cake and other factors depend which flow pattern occurs. We conducted experiments to validate the model by building filter cake under dynamic filtration conditions and flowing back water to clean up the filter cake. In summary, it is concluded from this study that:

1. A model for the filter cake thickness and properties was developed and can be used in a reservoir simulation model to capture the effects of gel damage.

2. The filter cake properties established for different pumping conditions can be used to design filter cake clean up by flowing back formation fluids at a shear stress that exceeds the yield stress of the filter cake. A theoretical model developed was tested using water as the flow back fluids.

CHAPTER III

HERSCHEL-BULKLEY FLUID FLOW IN PROPPED FRACTURE*

3.1 Introduction

In Chapter III, a theoretical model and its numerical solution will be presented to investigate the flow behavior of non-Newtonian fluid in porous media. The method of the Computational fluid dynamics (CFD) will be discussed first to study the porous-media non-Newtonian fluid flow. In the numerical simulations, we developed a micro pore-scale model to mimic the real porous structure in a proppant pack. The relationship between pressure gradient and superficial velocity was investigated under the influence of variable physical properties for non-Newtonian fluid, such as yield stress, power-law index, and consistency index. We also considered the effect of proppant packing arrangement and proppant diameter. The Herschel-Bulkley model was used with an appropriate modification proposed by Papanastasiou (1987) to mitigate numerical difficulties. Non-Newtonian fluid flow in porous media was investigated numerically by solving the Navier-Stokes equation directly.

The Kozeny-Carman equation, a traditional permeability-porosity relationship, has been popularly used in porous media flow models. However, this relationship is not suitable for non-Newtonian fluid flow in porous media. In this chapter, an analytical mathematical model is then developed to describe the flow behavior of non-Newtonian fluids in a proppant pack. One of the parameters, the effective radius, in the model needs

* Reproduced with permission from "Theoretical and Numerical Simulation of Herschel-Bulkley Fluid Flow in Propped Fractures" by Ouyang, L., Zhu, D. and Hill, A.D. 2013. Paper IPTC 17011 presented at the 6th International Petroleum Technology Conference, Beijing, China. Copyright 2013 by Society of Petroleum Engineers.

to be determined by regression analysis of the results from the numerical simulation. This avoids the use of Kozeny- Carman equation and can attain the exactly results for non-Newtonian fluid flow. In the mathematical model, the gel in the propped fractures is modeled as a Herschel-Bulkley fluid.

The result of the new model indicates that yield stress has a significant impact on non-Newtonian fluid flow through porous media, and the pressure gradient strongly depends on pore structure. The analytical expression reveals the physical principles for flow velocity in porous media. The variation trends of the threshold pressure gradient versus different influence factors are presented. By Computational Fluid Dynamics (CFD), I obtained a detailed view of the flow streamlines, the velocity field, and the pressure distribution in porous media. Numerical calculation results show that, in the center of the throats of porous media, the increasing yield stress widens the central plug-like flow region, and the increasing power law index sharpens the velocity profile. The new model can be readily applied to provide a clear guide to selection of fracture fluid, and can be easily incorporated into any existing reservoir simulators.

3.2 Numerical Simulation of Herschel-Bulkley Fluid Flow

Computational Fluid Dynamics (CFD) approaches make it possible to numerically solve flow, mass and energy balances in geometry structures of porous media. We identified the details of the flow process by direct numerical simulation of Herschel-Bulkley fluid transport at the pore scale using the CFD software, FLUENT, which is based on unstructured meshes to allow flexibility for the complicated geometry.

We investigated the flow behavior of Herschel-Bulkley fluid in porous media and studied the impacts of different key factors such as proppant size, rheological parameters, proppant packing arrangement and imposed pressure gradients on flow behavior.

3.2.1 Computational Geometry

To numerically simulate the flow of a Herschel-Bulkley fluid through a proppant pack, we started with a small domain consisting of 40 proppant particles arranged in the simple cubic packing as shown in **Fig. 3.1**. The flow domain for gel is the space between the proppants, shown in **Fig. 3.2**.

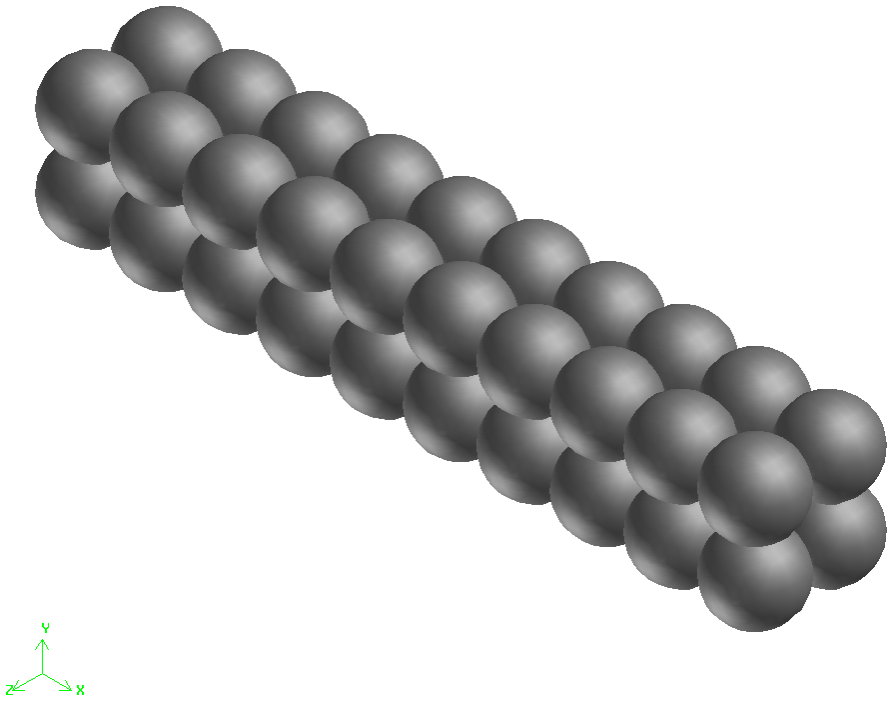

Fig. 3.1— Geometrical pattern for Simple Cubic proppant packing.

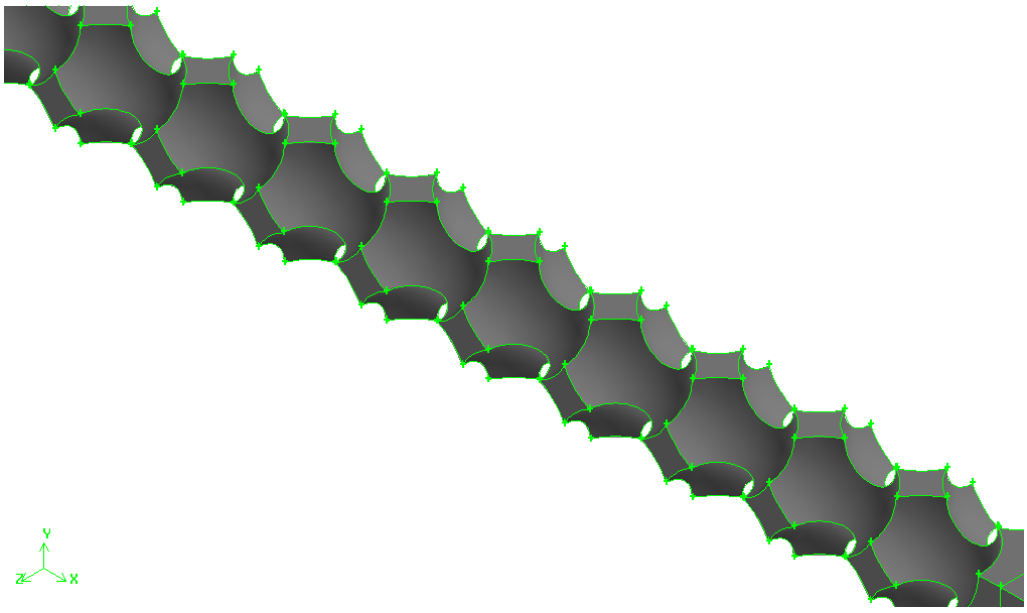

Fig. 3.2— Geometrical pattern for flow channel.

As shown in Fig. 3.2, the flow channel is the interstitial space between the proppants and is the domain where the fluid can flow, which is the main computational domain. The size and structure of the flow domain depend on the size, packing arrangement of the proppants, and the ratio of large proppant's diameter to small proppant's. To investigate the effect of proppant size, proppant diameter of 0.84mm, 0.42mm, 0.21mm and 0.149mm, corresponding to 20 mesh, 40 mesh, 70 mesh and 100 mesh sizes, were modeled. There are finite contact areas between the surfaces of adjacent proppants. The porosity of the packed bed depends on the packing arrangement and contact area. The computational domain also includes an entrance region and an exit region to avoid the effect of inflow and outflow. We use symmetrical boundary

condition at the surround of the entrance and exit region, constant velocity inlet boundary condition at the entrance region, and constant pressure outlet boundary condition at the exit region. The pressure gradient at these regions is negligible, comparing with the pressure gradient along the porous media zone. The geometry of the flow channel is established by GAMBIT, a preprocessing software package for generating flow geometry and mesh.

The actual proppant arrangement in the propped fracture is usually not as simple as shown in Fig. 3.1. The flow behavior of non-Newtonian fluid in porous media is sensitive to the pore structure. We investigated the influence of the proppant packing arrangement on the fluid flow in a micro porous media using three different proppant packing structures: simple cubic (SC, Fig. 3.3a), body centered cubic (BCC, Fig. 3.3b) and face centered cubic (FCC, Fig. 3.3c). The geometry patterns of three proppant packing arrangements are shown in **Fig. 3.3**.

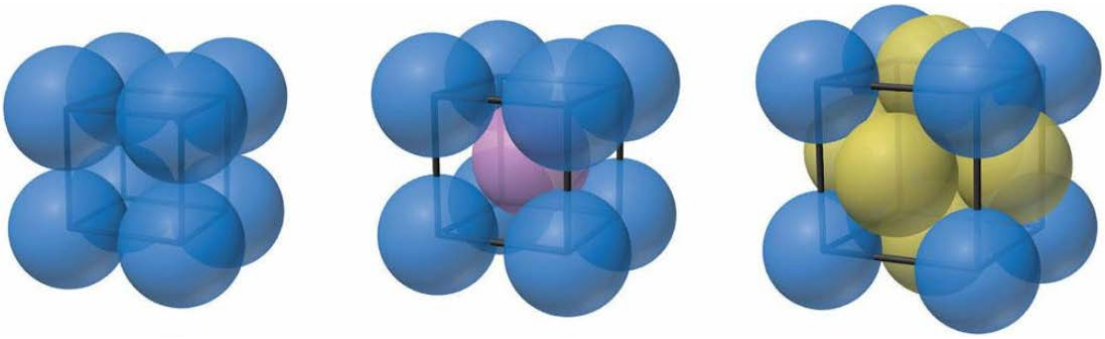

a).SC b).BCC c).FCC

Fig. 3.3—Three different packing ways.

The geometry frameworks of proppant packing arrangement of body center cubic and face center cubic are shown in **Fig. 3.4** and **Fig. 3.5** separately. The domains also consist 40 proppant particles. Comparing with the simplic center packing arrangment, they have the same number of proppant particles and porosity, but have different dimension sizes because of the different packing arrangemnt. This must be paid more attenation when calculating the pressure gradient. In order to clearly distinguish the structures, we provide right side, front side and isometric view of the packing arrangment.

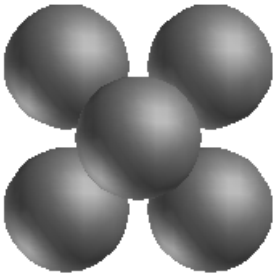

(a)

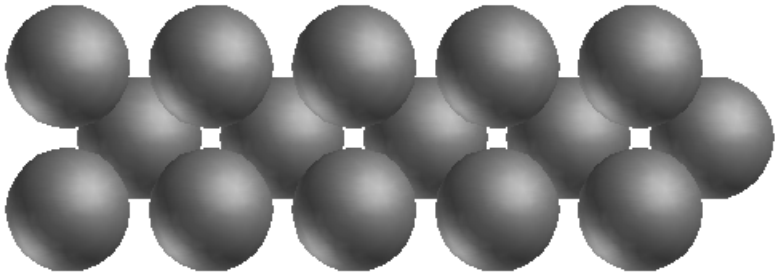

(b)

Fig. 3.4— Geometrical pattern for Body Center Cubic proppant packing. (a) Right side view. (b) Front side view. (c) Isometric view.

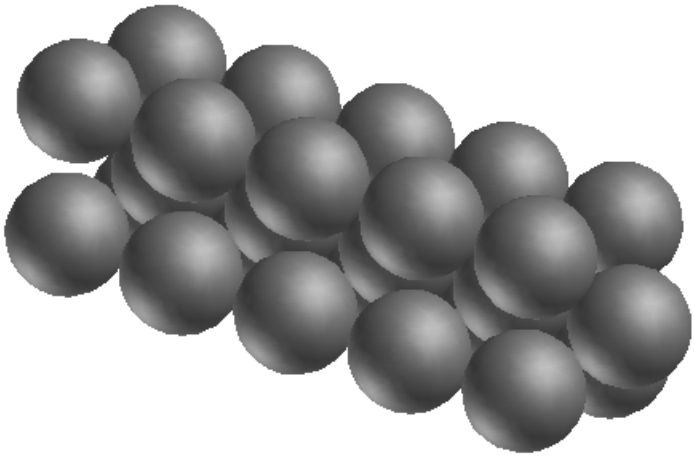

(c)

Fig. 3.4— Continued.

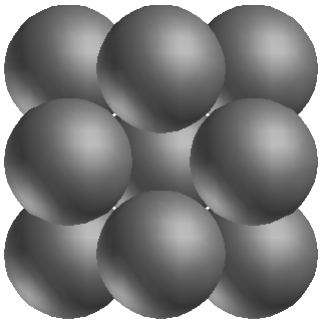

(a)

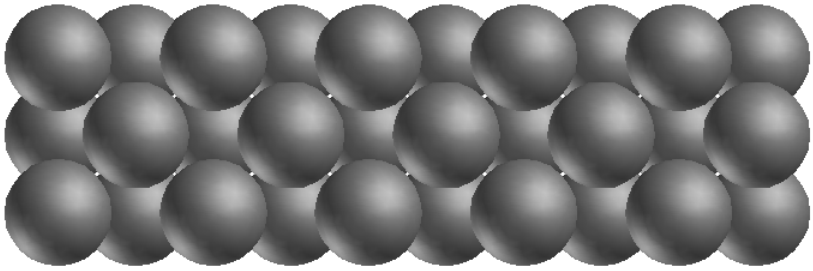

(b)

Fig. 3.5— Geometrical pattern for Face Center Cubic proppant packing. (a) Right side view. (b) Front side view. (c) Isometric view.

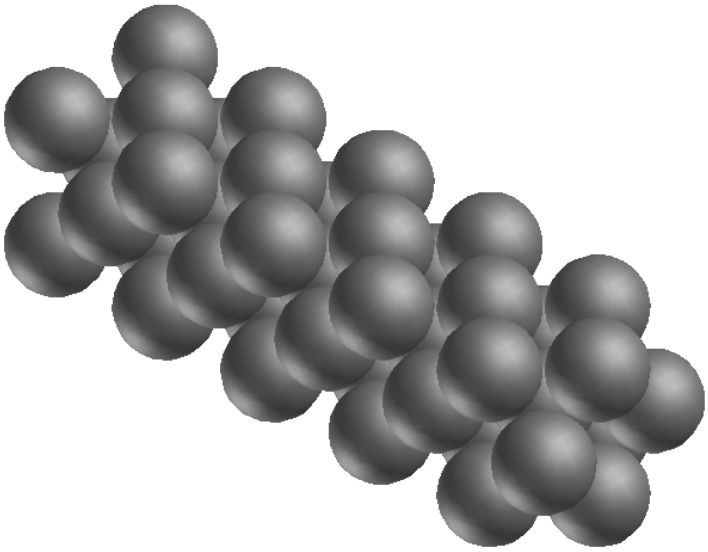

(c)

Fig. 3.5— Continued.

The proppant, used in hydraulic fracture treatments, do not have an unifrom diameter. They have a size distribution, some typical sizes 20/40, 30/50 mesh. The size opening for 20 mesh is about twice than 40 mesh. The same ratio for 30/50 mesh. The ratio of large diameter to small diameter of 2 is used in the study for 20/40 mesh and 30/50 mesh. This is the extreme case for size distribution issue. The small proppant was put in the center and the four large proppants were at the four corners. In this structure, the numer ratio of large proppant to small proppant is 1:1. The geometry frameworks of proppant packing arrangement of body center cubic with two different diameters are shown in **Fig. 3.6**.

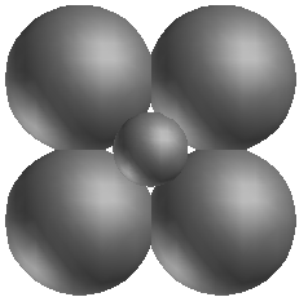

(a)

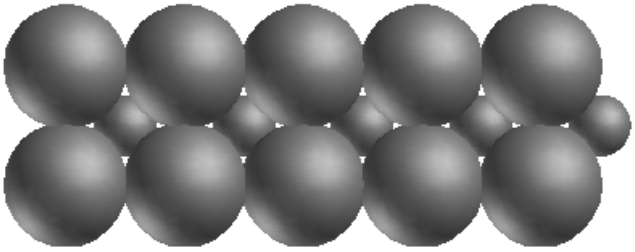

(b)

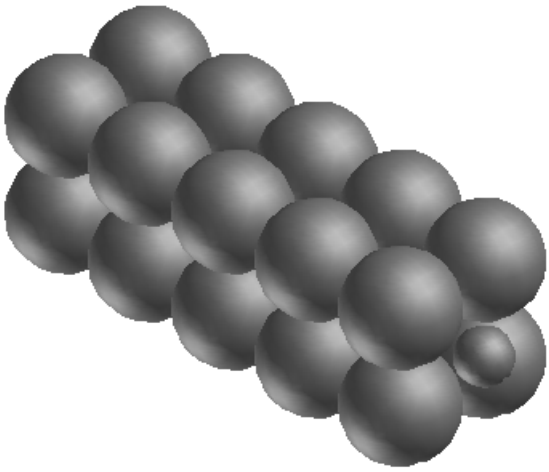

(c)

Fig. 3.6— Geometrical pattern for Body Center Cubic proppant packing with two different diameters. (a) Right side view. (b) Front side view. (c) Isometric view.

3.2.2 Generation and Independence of the Grid

The meshes of the computational domain are generated by GAMBIT software package, which is designed to build and mesh models for CFD. The unstructured grid is adopted. Unstructured grid has irregular shape and is more flexible in its ability to define complex shapes. The physical problem has complex geometrical structure for flow channel. The flow behavior of non-Newtonian fluid is sensitive to the geometric texture of the flow domain. It is very important to actual mimic the flow region for non-Newtonian fluid. The meshes of the calculation region of four pore structures (SC, BCC, FCC, and BCC with two different diameters) are shown in **Fig. 3.7**.

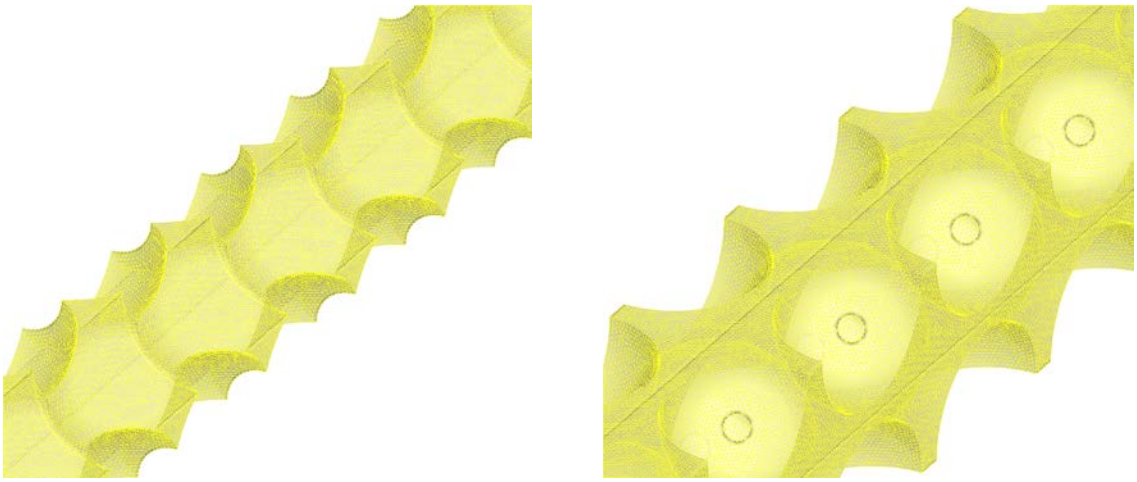

Fig. 3.7— Calculational models and meshes for the different proppant packing. (a) Simple cubic. (b) Body center cubic. (c) Face center cubic. (d) BCC with two diameters.

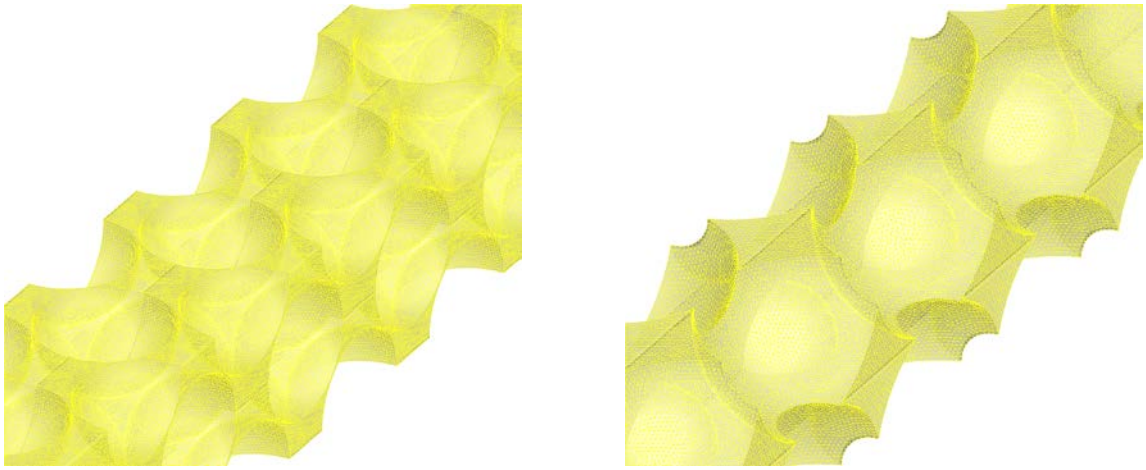

(c) (d)

Fig. 3.7— Continued.

The sensitivity of the results to mesh resolution was examined to assure the accuracy of the numerical simulations. Usually, using the smaller grid size in computational domain leads to more accurate results, but might cause numerical instability while require more computation time. A mesh refinement study was used to compare the effect of the mesh density on the solution to have sufficient accuracy and efficient computation time. For the simple cubic packing arrangement, the grid size in the x, y, and z-directions was decreases from 0.03 to 0.015 mm, and the total grid number increased from approximately 350,000 to 1.5 million grids, as shown in **Table 3.1**. A diagram of the different grid elements on the proppant surface is shown in **Fig. 3.8**. For pressure gradient, the numerical results using the grid size of 0.015 mm is approximately 1% higher than for the grid size of 0.02 mm, 2% higher than for the grid size of 0.025 mm and 5% higher than for grid size of 0.03 mm. The results showed that there is minimal loss of accuracy resulting from using larger grid sizes. The grid size of

0.02 mm was chosen for all numerical simulations to keep a balance between numerical accuracy and computational cost. Furthermore, the simulation exercises show that the cases using a grid size of 0.02 mm did not have any instability problems.

TABLE 3.1—MAXIMUM GRID EDGE SIZE AND TOTAL NUMBER OF GRIDS

Maximum Grid Edge Size (mm)	Total Number of Grid
0.015	1529144
0.020	800284
0.025	517116
0.030	349712

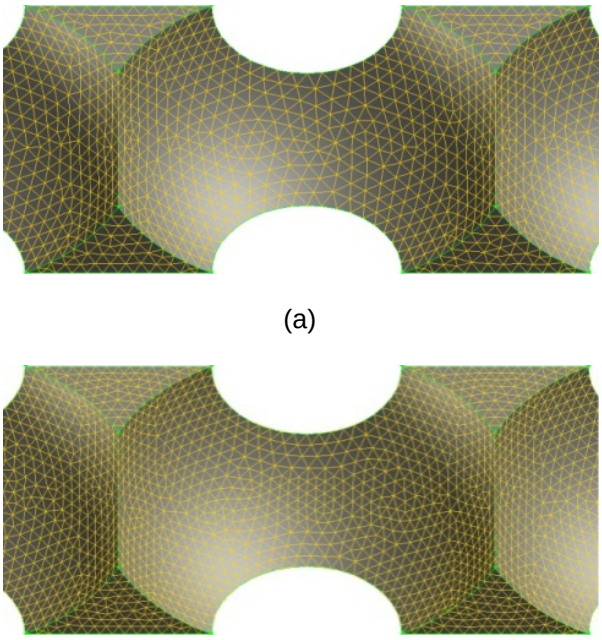

(a)

(b)

Fig. 3.8—Grids on proppant surfaces using different grid sizes. (a) 0.03mm. (b) 0.025mm. (c) 0.02mm. (d) 0.015mm.

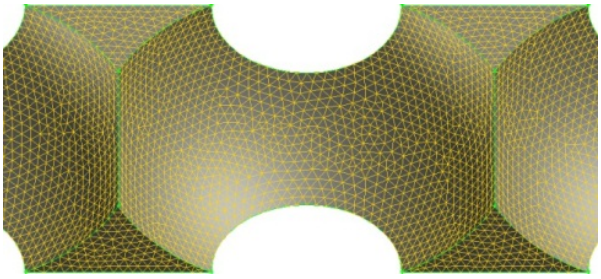

(c)

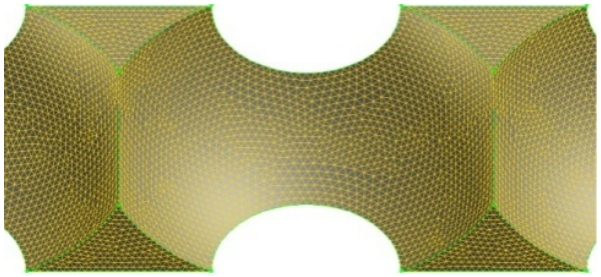

(d)

Fig. 3.8—Continued.

3.2.3 Herschel-Bulkley- Papanastasiou Model

To model the stress-deformation behavior of the viscoplastic gels used in the hydraulic fracturing, the Herschel-Bulkley constitutive equation was adequate. The Herschel-Bulkley model includes the shear-thinning or shear-thickening behavior of power law fluid and the yield stress effect of the Bingham fluid. The rheology equation of the Herschel-Bulkley model is presented in the previous chapter, Eq. 2.6. When the shear stress is less than the yield stress, there will be a solid plug-like core flowing. The unyielded zone leads to the discontinuity of the first order velocity derivative and causes an instability problem in numerical simulation. To avoid this issue in any viscoplastic model, Papanastasiou (1987) proposed a modification by introducing a material

parameter, which controls the exponential growth of stress. In Herschel-Bulkley-Papanastasiou model, the rheology equation, as shown below, is valid for the yielded and unyielded zones.

$$\tau = \tau_0\left[1-\exp\left(-m\gamma\right)\right]+C\gamma^n \tag{3.1}$$

where m is the stress growth exponent. The apparent viscosity is given as:

$$\eta = C\left|\gamma\right|^{n-1}+\frac{\tau_0}{\left|\gamma\right|}\left[1-\exp\left(-m\left|\gamma\right|\right)\right] \tag{3.2}$$

For low shear rate, this equation leads to a very high viscosity. This stands for the solid-plug flow zone. Papanastasiou recommends that the stress growth exponent should be larger than 1000 to closely mimic an ideal flow behavior of the viscoplastic fluid. Belblidia et al. (2010) showed that the new model can perfectly match the original Herschel-Bulkley model through exploring the viscoplastic regime. To use the Herschel-Bulkley-Papanastasiou model, a user-defined function (UDF), written in C program language, was compiled and linked to FLUENT. The UDF function defines the apparent viscosity following **Eq. 3.2**. The code of the UDF function for Herschel-Bulkley-Papanastasiou model is shown in Appendix E. In this study, each case has millions of grids and extremely high CPU, so the cases were run on an IBM iDataplex Cluster with nodes based on Intel's 64-bit Nehalem & Westmere processor. The code of the UDF function was modified to parallel version, which can be used on either a parallel computer system or a serial computer system.

3.2.4 Computational Parameter, Boundary Condition and Algorithm

To cover the most possible conditions in field circumstance, we considered a large range of various rheological parameters. The yield stress varies from 0 to 200 Pa, the consistency index varies from 10 to 100 $Pa \cdot s^n$ and the power law index ranges between 0.6 and 1. The data set is summarized in **Table 3.2**. Table 3.2 also provides the proppant diameter and porosity of pack bed. The density of the studied fluids has been set equal to 1000 kg/m^3 and the viscosity is calculated by the Herschel-Bulkley model during numerical simulation. To assure and accelerate the convergence of numerical stimulation, the steady flow solution of a Newtonian fluid is taken as the initial condition of the flow field for numerical iteration of the Herschel-Bulkley fluids.

TABLE 3.2—HERSCHEL-BULKLEY FLUID AND PROPPANT PARAMETERS FOR PARAMETRIC SIMULATION STUDY

Parameter	Value
Superficial Velocity, m/s	0.5, 0.1, 0.05, 0.01, 0.005, 0.001, 1E-4, 1E-5, 1E-6
Consistency Factor, $Pa \cdot s^n$	10, 100
Flow Behavior Index	0.6, 0.7, 0.8, 0.9, 1
Yield Stress, Pa	0, 0.1, 1, 10, 50, 100, 200
Porosity	0.3
Diameter of Proppant, mm	0.84, 0.42, 0.21, 0.149

FLUENT uses the finite-volume method to solve the Navier-Stokes equations for fluids. In the simulation, constant physical properties at 290 °K and 50 psi are assumed for the fluids in the grid. For the flow boundary condition, a constant velocity boundary condition is used at the inlet and a constant pressure condition is used at outlet. This ensures high accuracy of the results and avoids possible instability problem. The

boundary condition at the outlet was then zero static pressure. The pressure was relative to the reference pressure, which was set as 50 psi. For wall boundary conditions, no-slip condition was adopted on the surface of proppant. This allows the fluid layer adjacent to the wall to have a velocity equal to that of the wall, which is zero in this case. To maintain periodicity in the width direction, symmetry boundary conditions were used in the span-wise and the transverse directions.

We used the method of Green-Gauss Cell Based to calculate the gradients, which is used to discretize the convection and diffusion terms in the flow equation. For the spatial discretization of flow moment governing equations, the second-order upwind scheme is adopted to assure the accuracy of results. In the cases involving a yield stress term, where convergence to target could be very difficult to attain under the high resolution advection scheme, the first-order upwind differencing scheme was used and convergence was then achieved. To avoid pressure-velocity decoupling, we used Semi-Implicit Method for Pressure Linked Equations (SIMPLE) algorithm. SIMPLE algorithm has been widely used in numerical procedure to solve the Navier-Stokes equations in computational fluid dynamics. To clarify the procedure, the flow chart of SIMPLE algorithm is shown in **Fig. 3.9**.

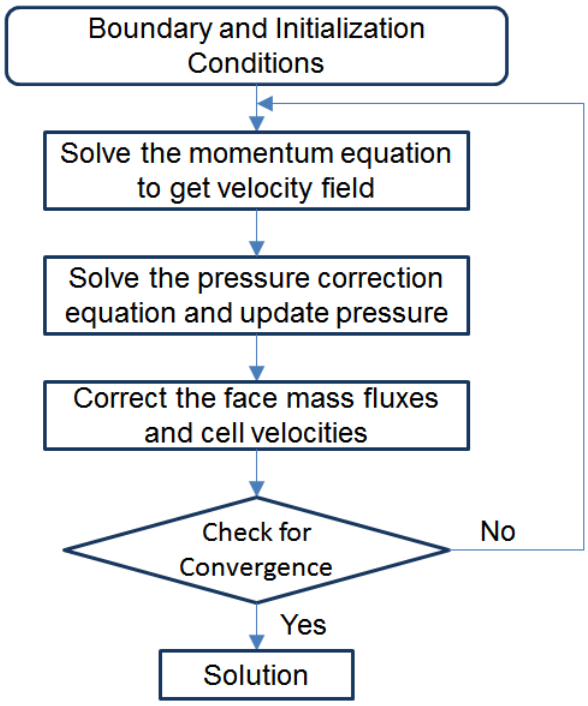

Fig. 3.9—Flow chart of SIMPLE algorithm.

To suppress oscillations or divergence in the flow solution, Under Relaxation Factors for pressure, density, body forces and momentum were reduced to a small value at the beginning several hundred steps of numerical iterations. Under relaxation factors limit the amount which a variable change from previous iteration to the current one. The small values for under relaxation factors may prevent oscillations in residuum developing. At the same time the solution may need more time to converge. After attaining the stability in the calculation, Under Relaxation Factors can become to be a normal value to speed up convergence for all variables. The solution was assumed to have converged when the root mean square (RMS) of the normalized residual error

reached 10^{-7} for all of the equations. The calculations assumed that the flows are three-dimensional, steady, laminar and incompressible.

3.2.5 Flow Field Visualizations

Visualizations of the velocity and pressure fields from the numerical simulations of a Herschel-Bulkley fluid flow in a proppant pack are helpful in understanding the pressure drop – flow rate relationship. **Fig. 3.10** shows porous-media flow behavior of a Herschel-Bulkley fluid in simple cubic packing arrangement. Fig. 3.10a shows the contour of velocity along the middle plane of the flow domain, while Fig. 3.10b shows the vector field of velocity in three dimensions in a throat of the porous media. Red color stands for high value and blue color stands for small value. Both of them show that the maximum velocity occurs at the center of the narrowest throat of the proppant pack. In the numerical results, it was also noticed that velocity can be up to 20 times the average inlet velocity in some areas of the flow field, but the shear-thinning and the yield stress reduce the value of maximum velocity. Fig. 3.10c shows the streamlines in the micro pore-scale structure. Fig. 3.10d shows the pressure distribution along the flow channel.

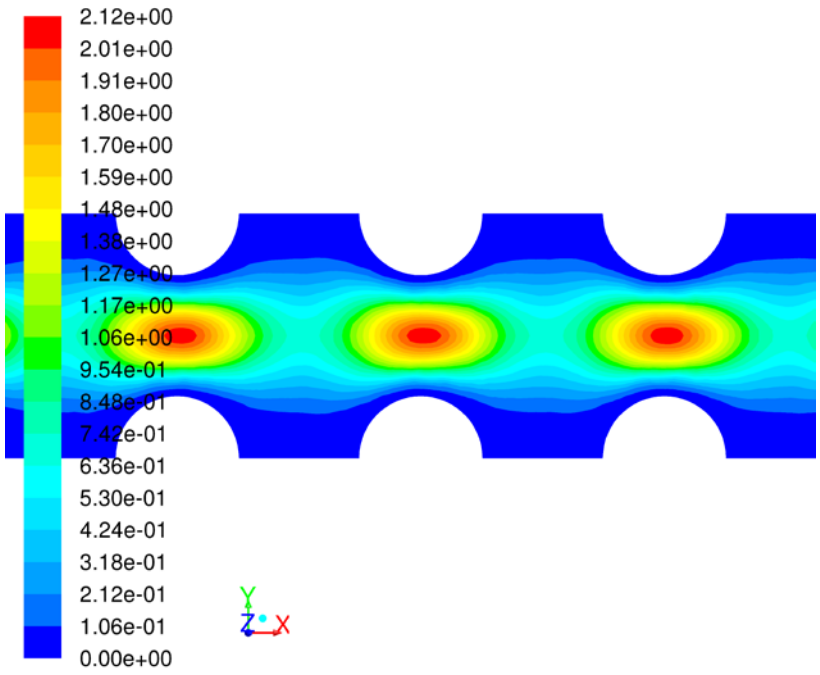

(a)

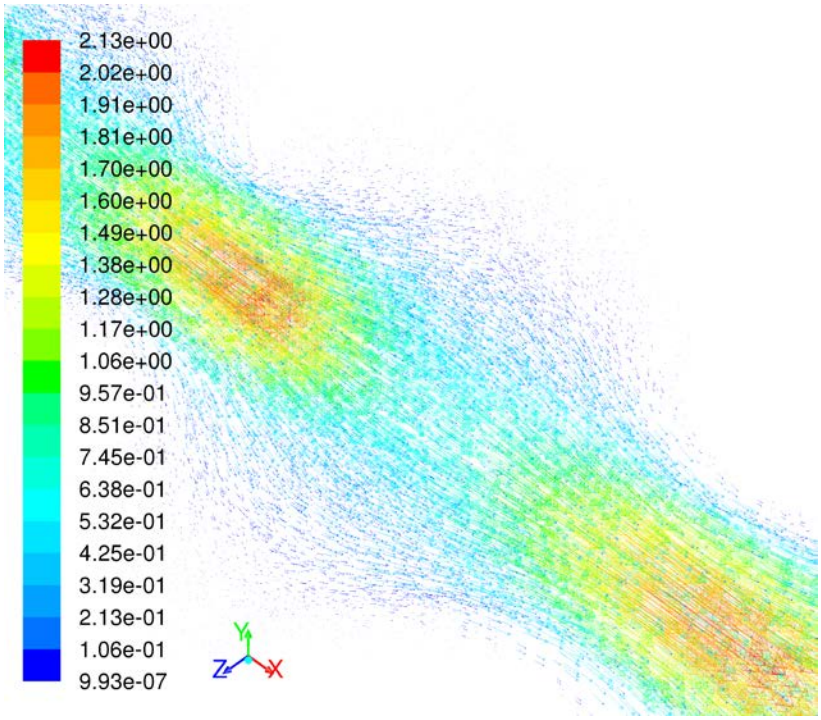

(b)

Fig. 3.10—Visualizations of non-Newtonian fluid in media proppant pack of SC. (a) Velocity contour at the middle plane of proppant pack bed. (b) Vector field of velocity in 3D. (c) Streamline. (d) Pressure distribution.

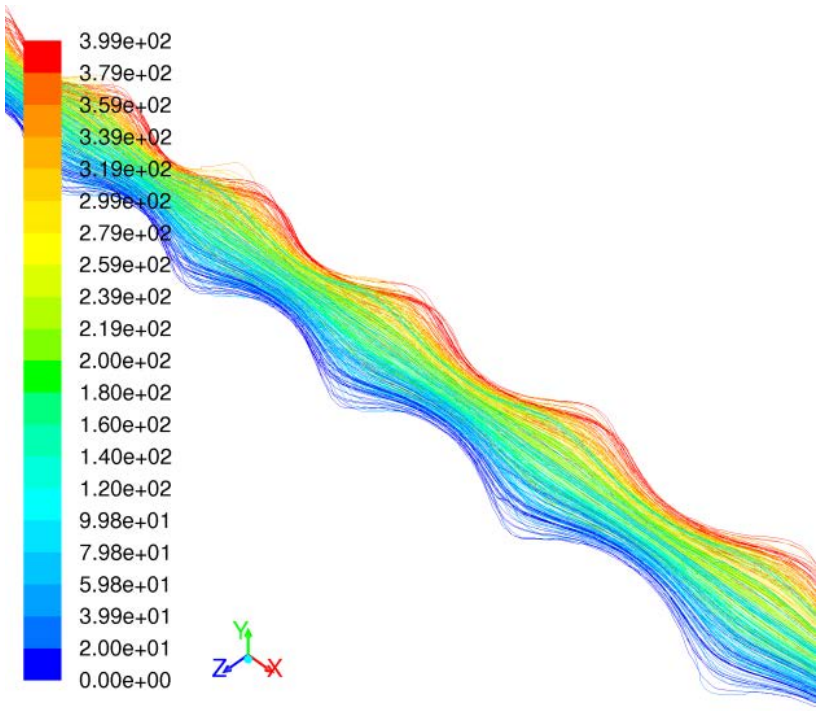

(c)

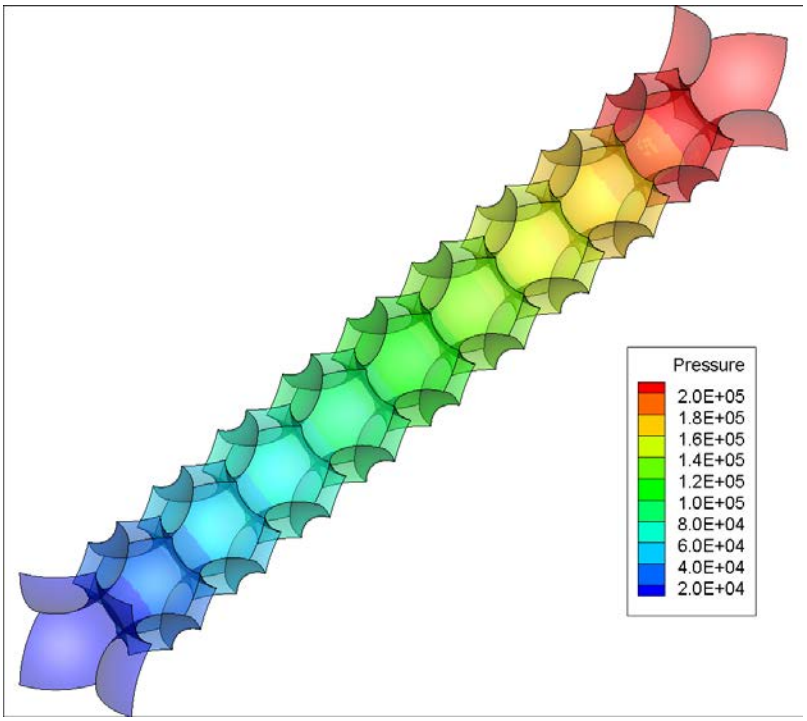

(d)

Fig. 3.10—Continued.

Fig. 3.11, 3.12 and 3.13 show contour of velocity, the vector field, streamline and pressure distribution in proppant packing of BCC, FCC, and BCC with two diameters, respectively. As shown in four group pictures, fluid has large different flowing behavior between four pore structures. This leads to the difference of flow initiation gradient for fluids with yield stress and the correlation between pressure gradient and velocity between four proppant packing arrangements.

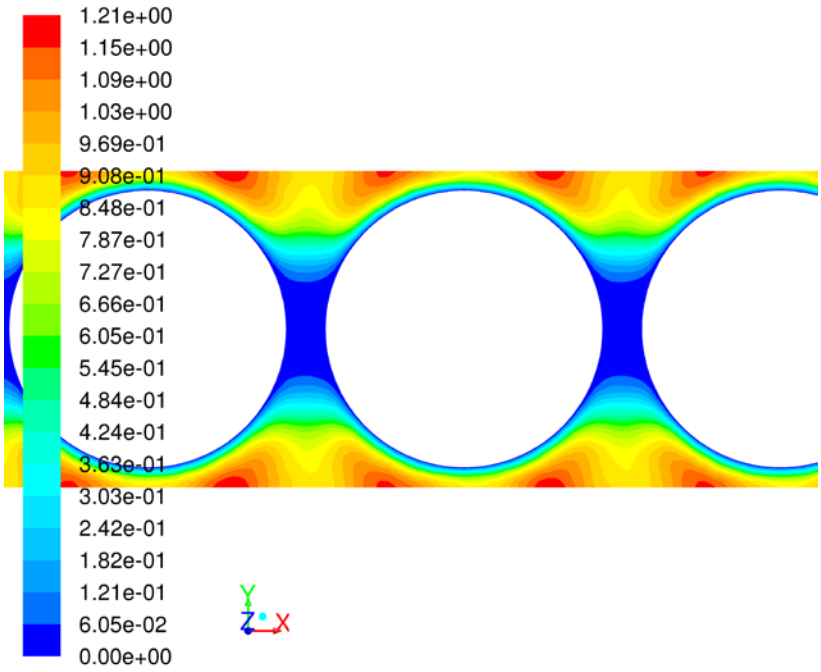

(a)

Fig. 3.11—Visualizations of non-Newtonian Fluid in media proppant pack of BCC. (a) Velocity contour at the middle plane of proppant pack bed. (b) Vector field of velocity in 3D. (c) Streamline. (d) Pressure distribution.

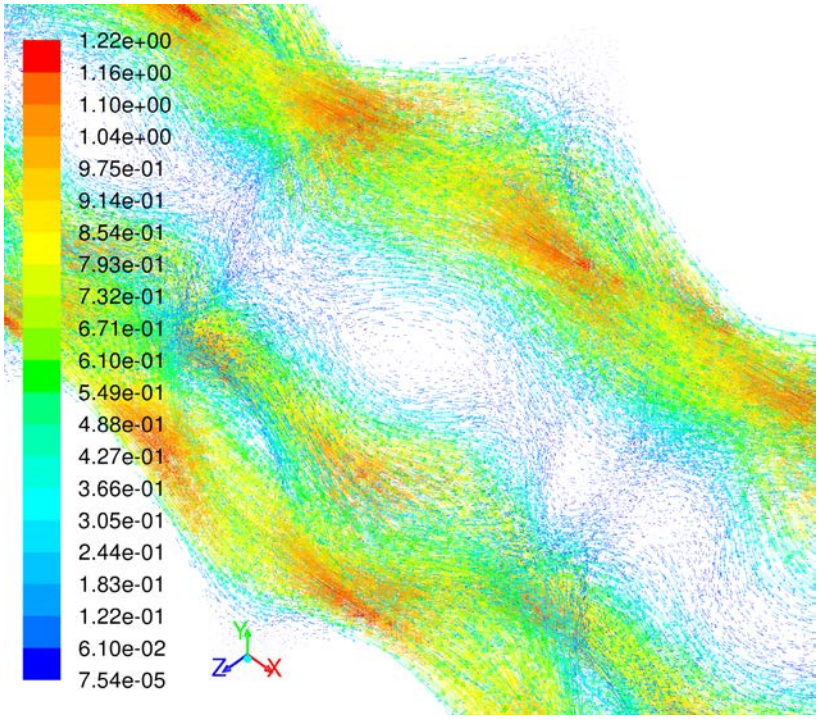

(b)

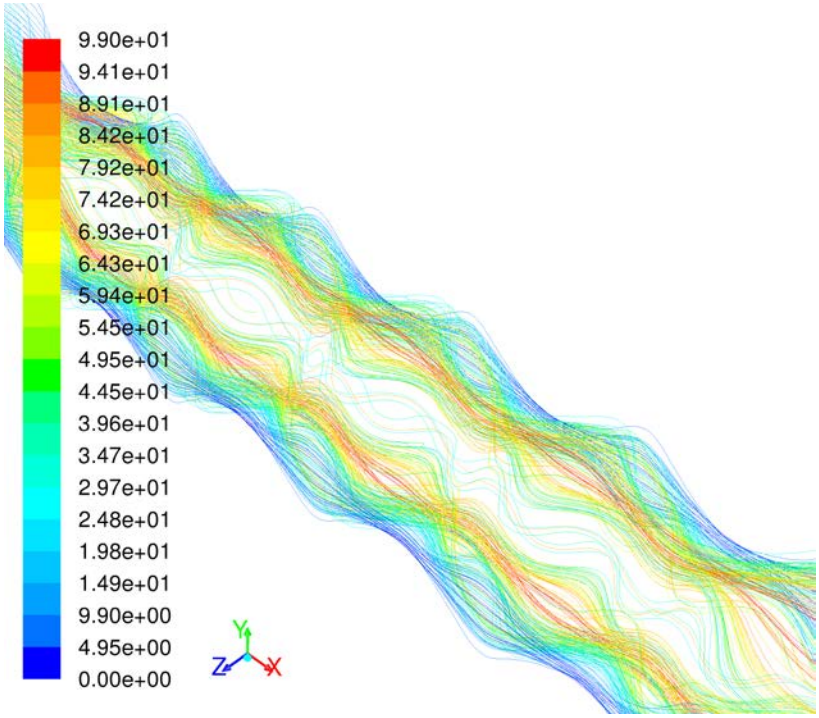

(c)

Fig. 3.11—Continued.

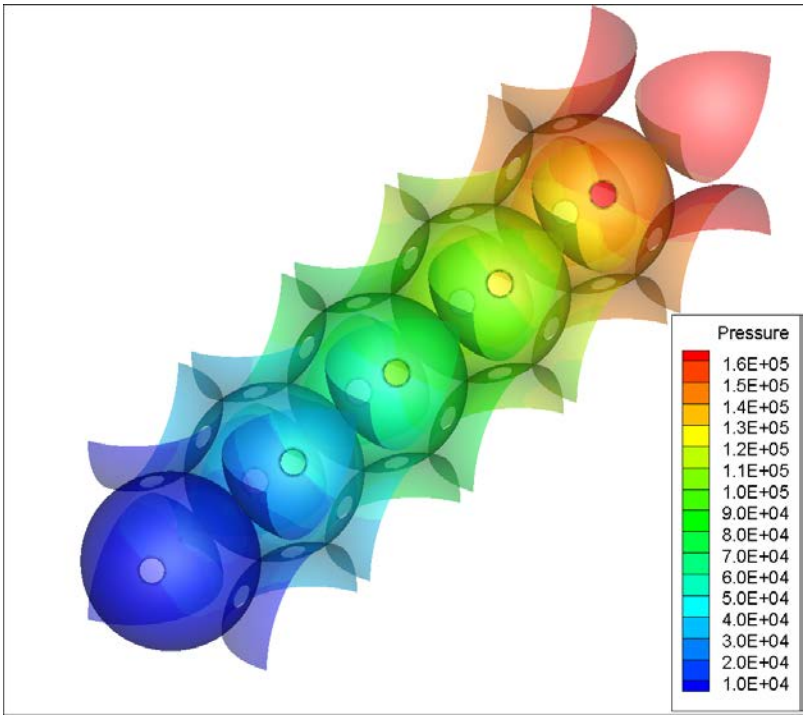

(d)

Fig. 3.11—Continued.

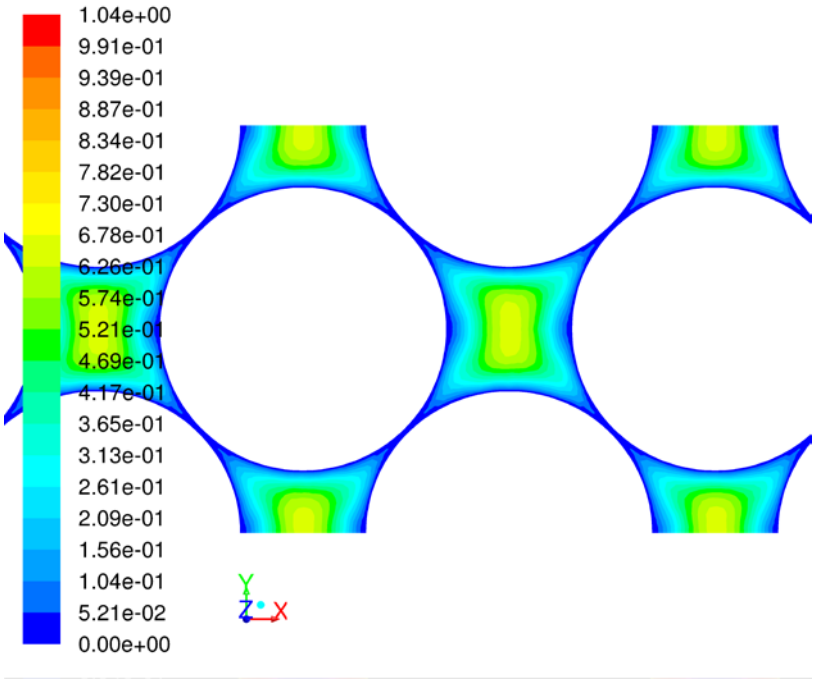

(a)

Fig. 3.12—Visualizations of non-Newtonian Fluid in media proppant pack of FCC. (a) Velocity contour at the middle plane of proppant pack bed. (b) Vector field of velocity in 3D. (c) Streamline. (d) Pressure distribution.

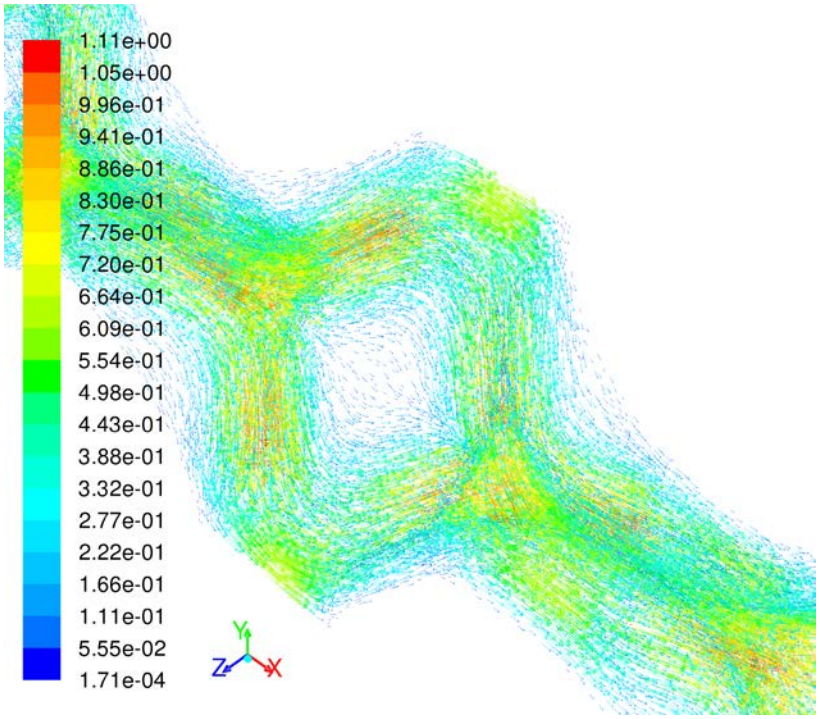

(b)

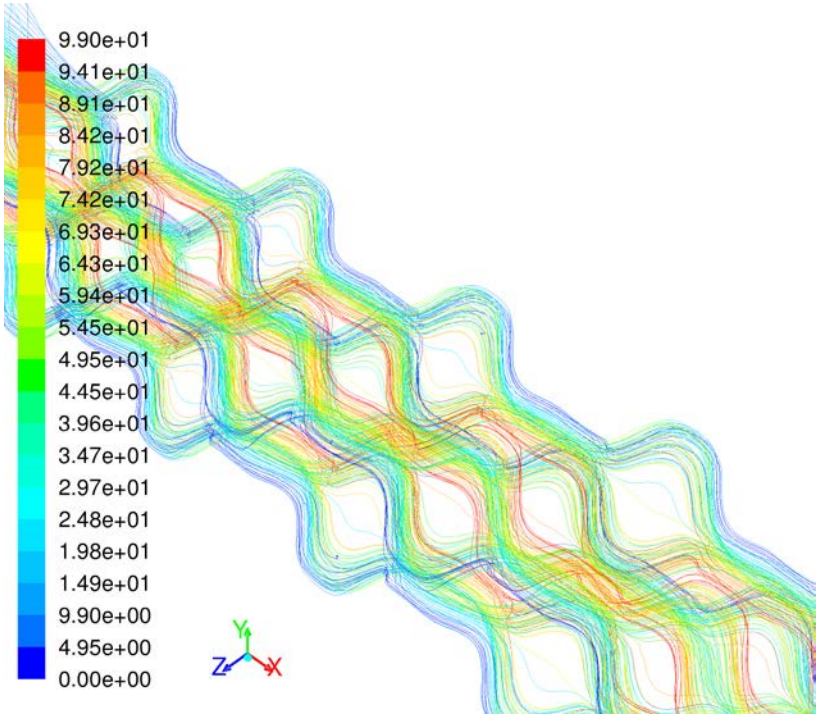

(c)

Fig. 3.12—Continued.

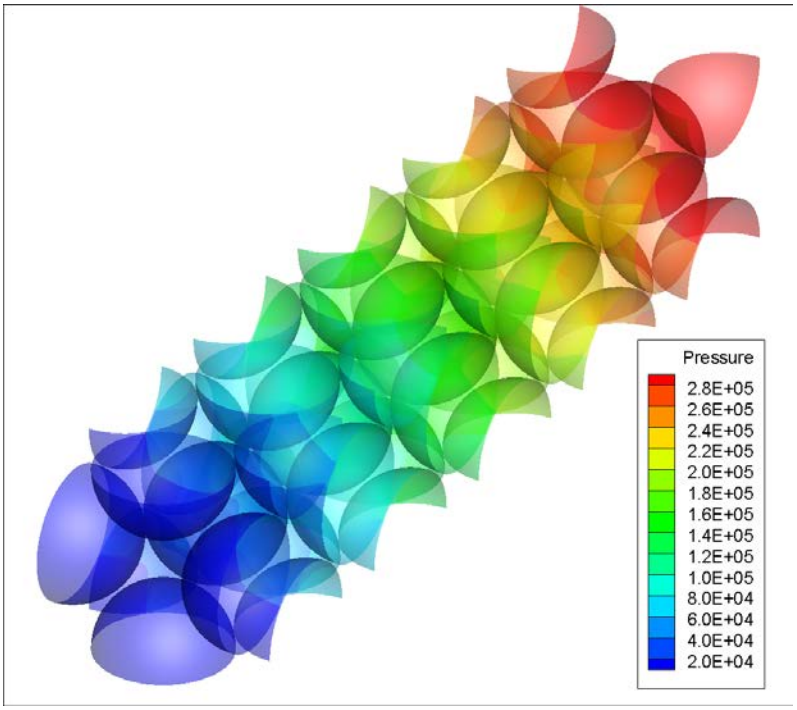

(d)

Fig. 3.12—Continued.

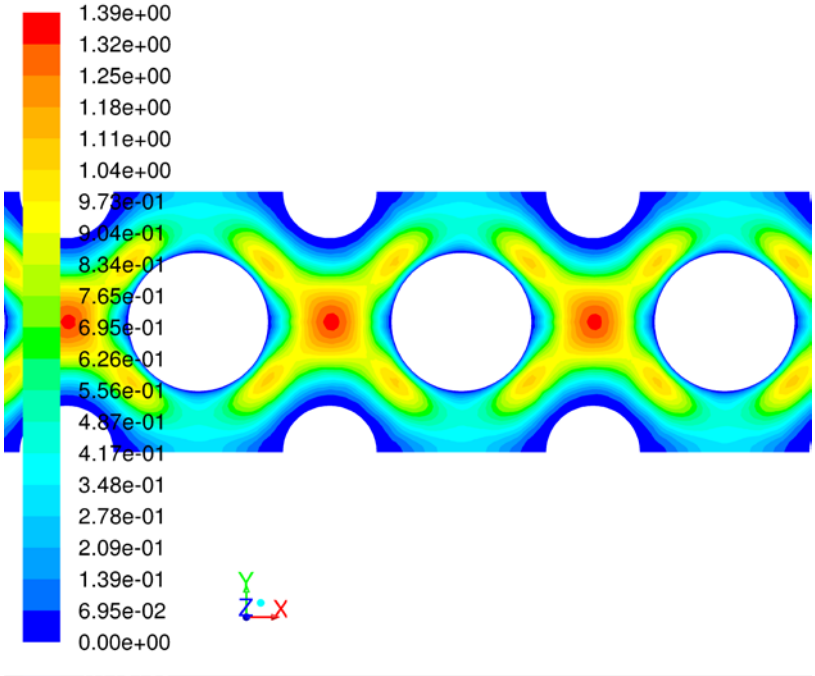

(a)

Fig. 3.13—Visualizations of non-Newtonian Fluid in media proppant pack of BCC with two diameters. (a) Velocity contour at the middle plane of proppant pack bed. (b) Vector field of velocity in 3D. (c) Streamline. (d) Pressure distribution.

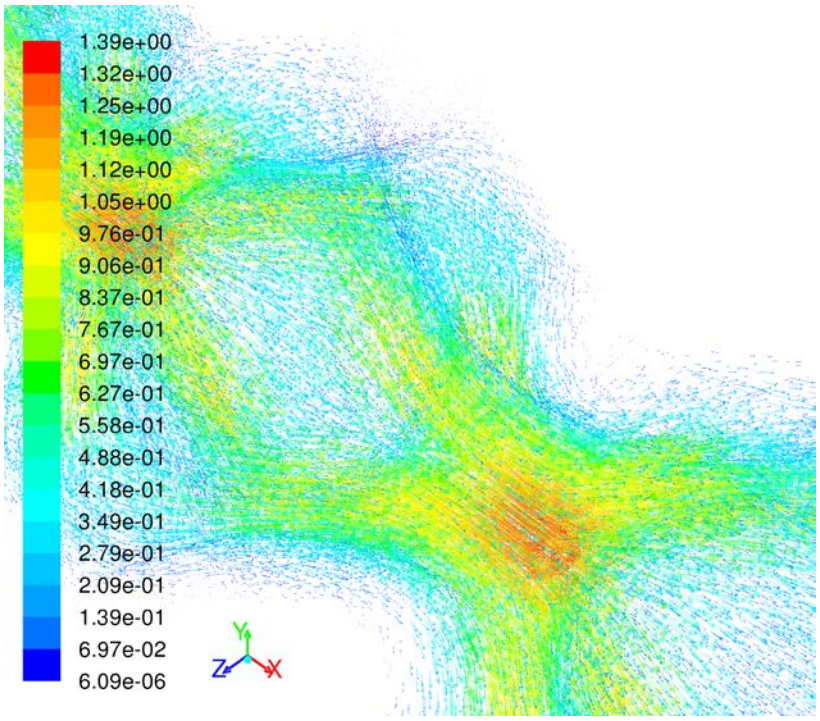

(b)

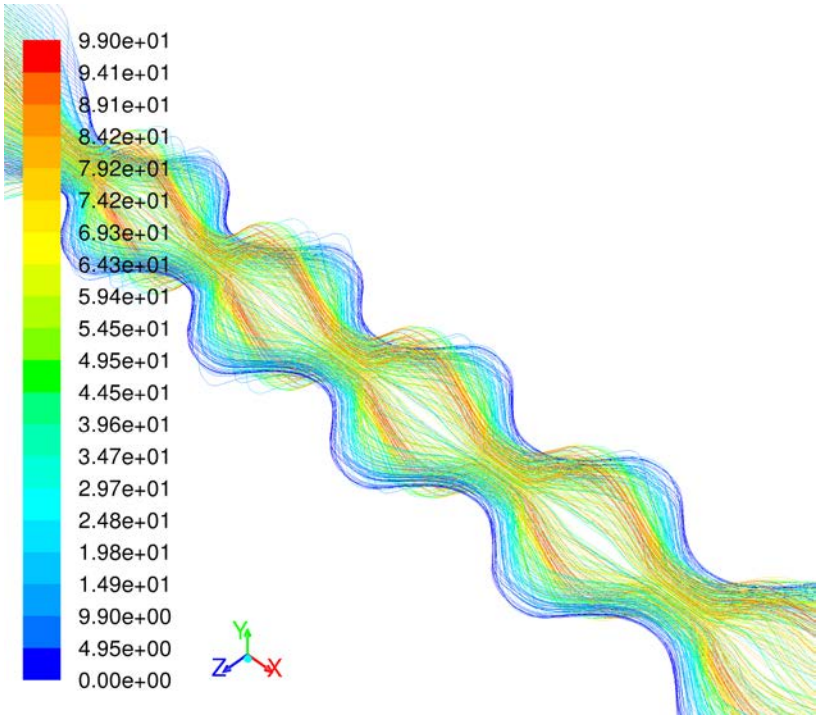

(c)

Fig. 3.13—Continued.

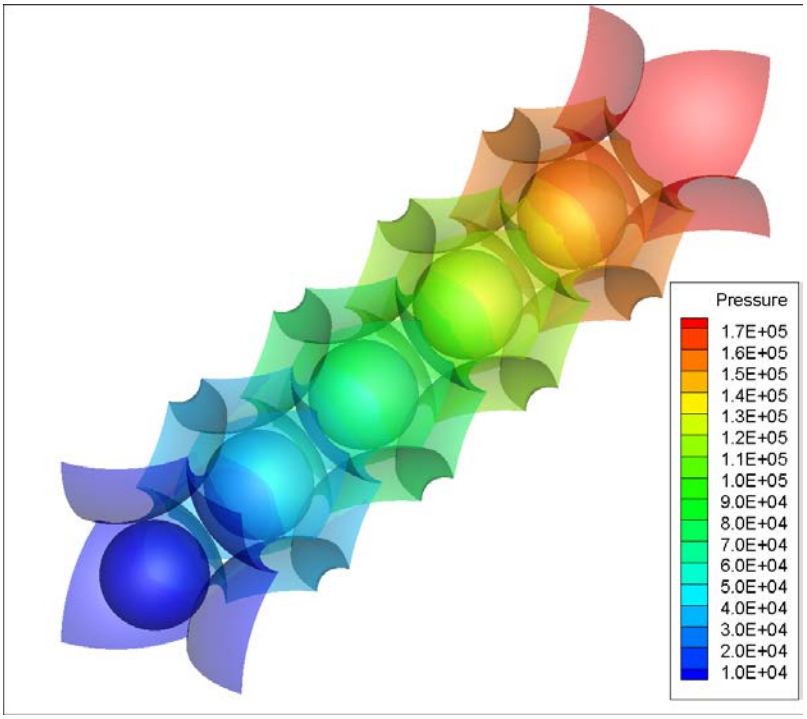

(d)

Fig. 3.13—Continued.

3.2.6 Effect of Power Law Index

A Power-Law fluid is a common type of non-Newtonian fluid. The power-law fluid can be mathematically defined by the following equation:

$$\tau = C\gamma^{n} \tag{3.3}$$

where γ is the shear rate, τ is the shear stress, C is the consistency factor and n is the flow behavior index. From the **Eq. 3.3**, the effective viscosity for a Power-Law fluid is given by the **Eq. 3.4**:

$$\mu_{eff} = C\gamma^{n-1} \tag{3.4}$$

The effective viscosity of Power-Law fluid is a function of shear rate, and it is not a constant. If Power-Law index *n* is less than one, the effective viscosity decreases with the increasing shear rate.

Fig. 3.14 shows pressure gradient vs. Darcy velocity for different values of the power law index. As shown in the figure, the power law index has a significant impact on the pressure gradient, especially at high superficial velocities. At high velocity, the shear-thickening fluids (n>1) cause an acute increase in pressure gradient. The interesting discovery is that the pressure gradient is inversely proportional to the power law index at very low velocity, as shown in Fig. 3.14b. This can be explained from velocity equation relationship for Power-Law fluid flow in porous media, shown below, **Eq. 3.5**:

$$U_{Darcy} = \frac{1}{3+1/n}\left(\frac{\Delta pR}{2CL}\right)^{1/n} R\phi \qquad (3.5)$$

where U_{Darcy} is the Darcy velocity in meters/second; n is the Power-law index; Δp is the pressure drop in Pa; R is the effective pore throat radius in meters; C is the consistency index in Pa·s^{n-2}; L is the pore throat length in meters and Φ is porosity. At low superficial velocity, if the term $\frac{-\Delta p}{2CL}$ is smaller than 1, smaller n ($0.6 < n < 1.4$) leads to smaller value of the term $\left(\frac{-\Delta p}{2CL}\right)^{1/n}$. In low superficial velocity zone, for the same velocity, the fluid with smaller power law index creates a higher pressure gradient. On

the contrary, If the term $\frac{-\Delta p}{2CL}$ is larger than 1, smaller n leads to larger value of the term $\left(\frac{-\Delta p}{2CL}\right)^{1/n}$.

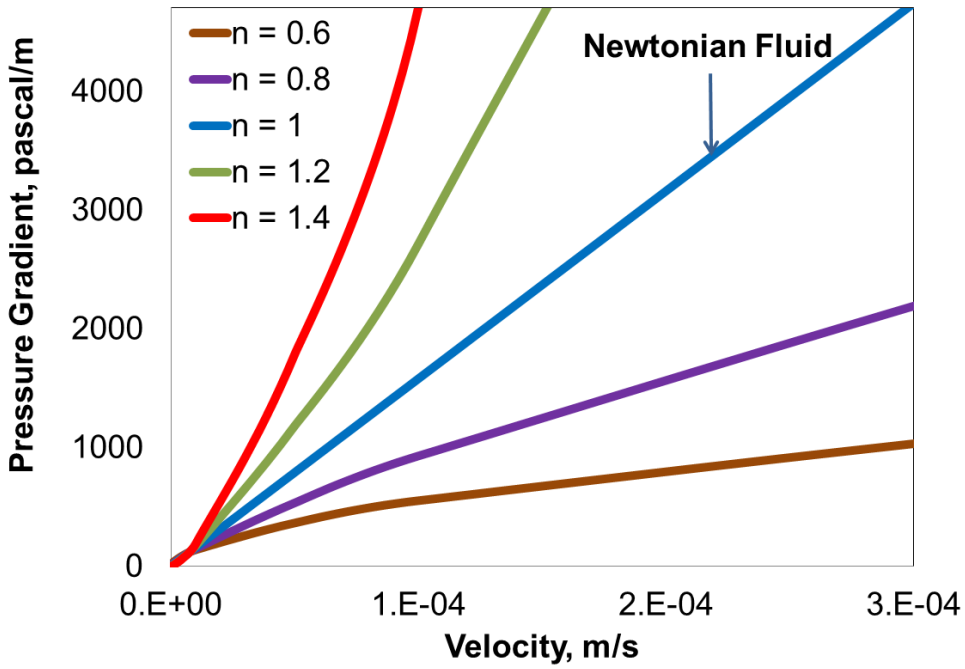

(a)

Fig. 3.14—Pressure gradient vs. superficial velocity for power law fluids with different power law index. (a) Large scale. (b) Small scale.

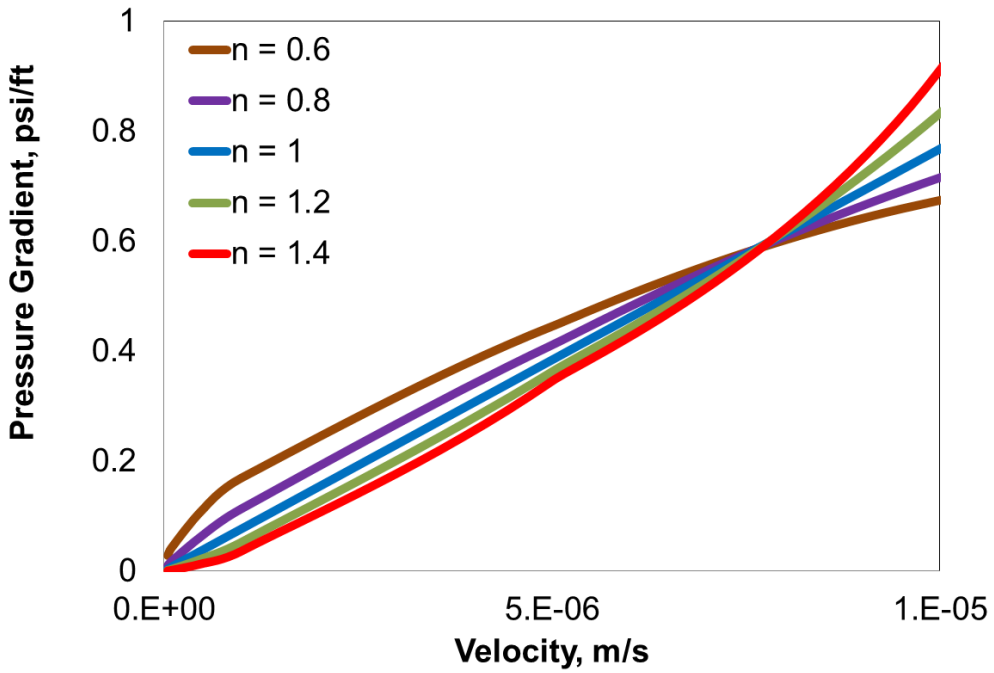

(b)

Fig. 3.14—Continued.

Fig. 3.15 shows, in the pore throat, the flow behavior of non-Newtonian fluids with different power law indexes. For Fig. 3.15a, 3.15b, and 3.15c, the contours were taken on a cross section at the narrowest part of the pore throat of simple cubic packing. The three cases have the same flow rate. As shown in Fig. 3.15d, decreasing the power law index flattens the velocity profile and reduces the maximum velocity; and increasing the power law index has an opposite effect. This characteristic behavior of the power law index is the same as what happen in pipe flow, which is shown in Appendix C.3, simulation validation.

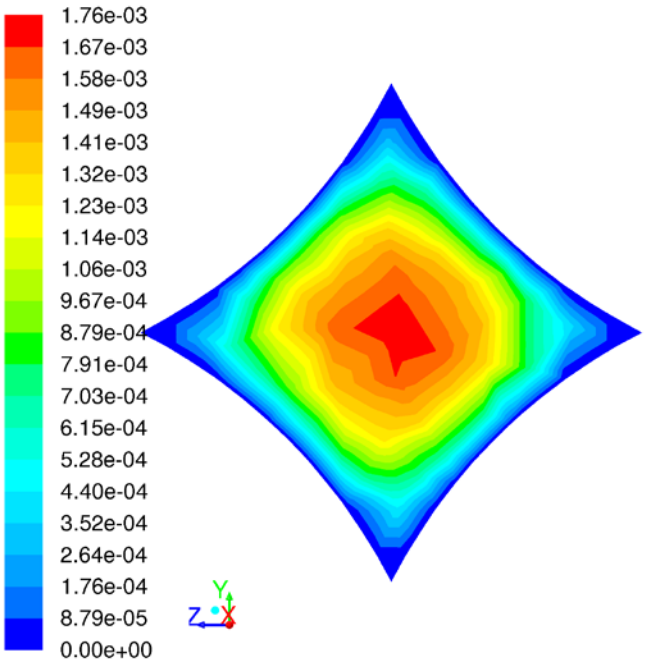

(a)

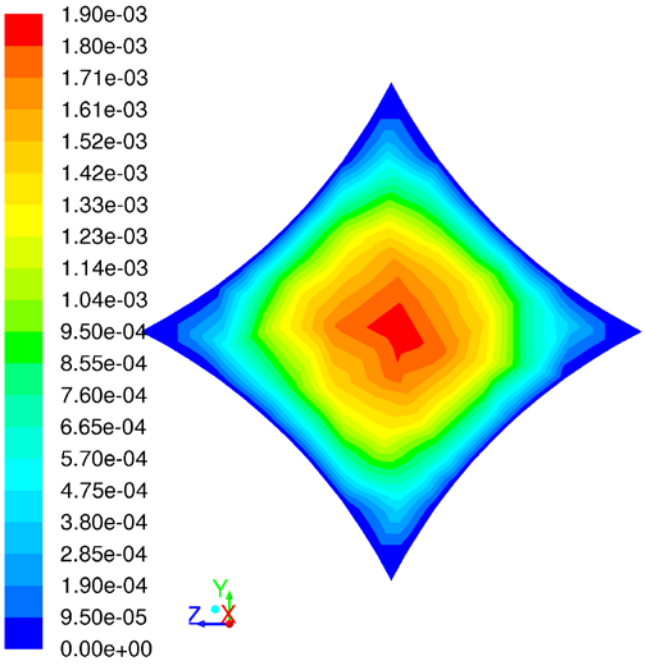

(b)

Fig. 3.15—Flow characteristic of power law fluid at the cross section of the throat. (a) Velocity contour (n = 0.6). (b) Velocity contour (n = 0.8). (c) Velocity contour (n = 1). (d) Comparison of velocity profile.

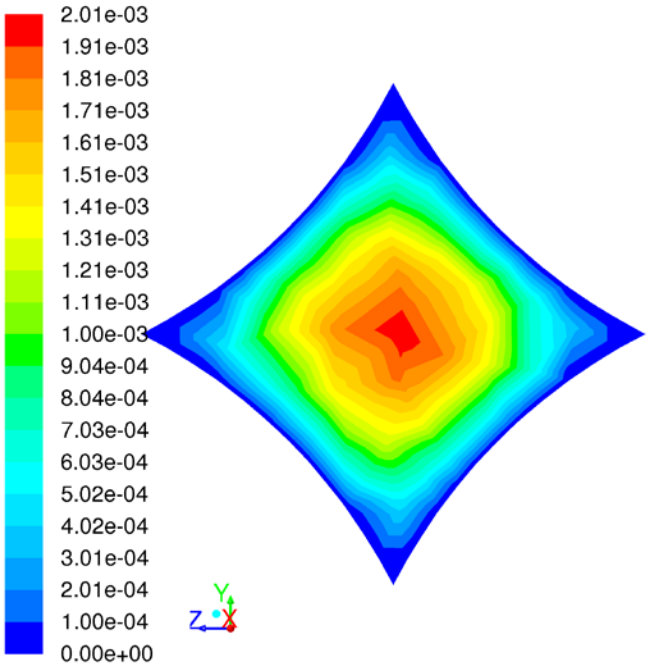

(c)

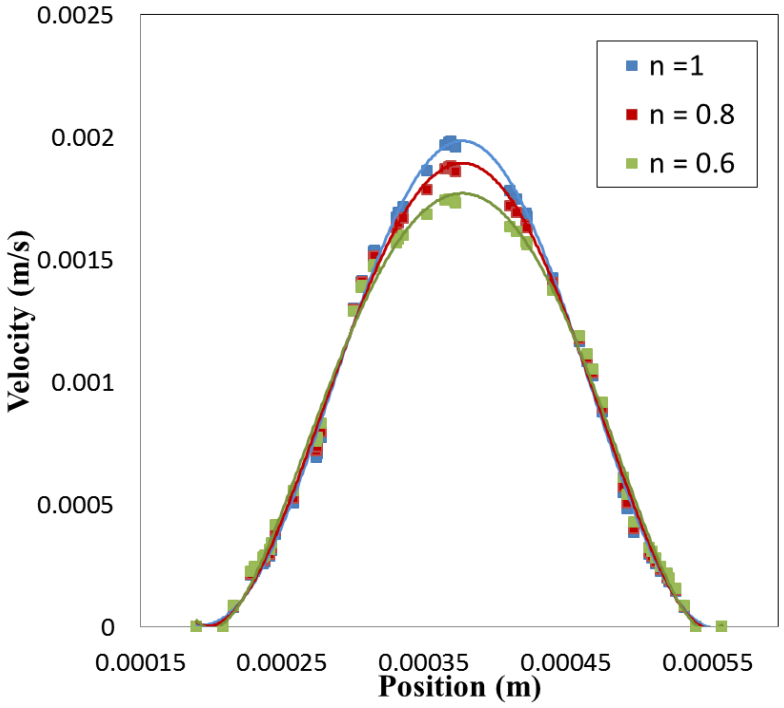

(d)

Fig. 3.15—Continued.

3.2.7 Effect of Yield Stress

For a fluid that has yield behavior, the value of apparent viscosity is infinite if the pressure gradient is less than a critical value. Bingham fluid can be mathematically defined by the following equation:

$$\begin{cases} \gamma = 0 & |\tau| < \tau_0 \\ \tau = \tau_0 + C\gamma & |\tau| \geq \tau_0 \end{cases} \tag{3.6}$$

From **Eq. 3.6**, the viscosity for a Power-Law fluid is given by

$$\mu_{eff} = \begin{cases} \infty & |\tau| < \tau_0 \\ \dfrac{\tau_0}{\gamma} + C & |\tau| \geq \tau_0 \end{cases} \tag{3.7}$$

The effective viscosity of Bingham fluid is a function of shear rate, shear stress and initial yield stress.

Fig. 3.16 plots the pressure gradient vs. velocity for different yield stresses. The Bingham fluid can flow only after the pressure gradient exceeds a critical value. **Fig. 3.17** reveals that the flow initiation pressure gradient increases linearly with the yield stress. The yield stress influences the flow behavior of non-Newtonian fluids through two effects. First, a certain critical pressure drop value needs to be exceeded for the flow to be initiated. This is represented by the term (*AR-B*) in Eq. 3.16. Second, for fluids with yield stress, there is a plug flow region of constant velocity in the center of the flow channel. The term $f(\alpha)$ in Eq. 3.16 reflects this impact of the yield stress. Both of these effects lower the flow rate and reduce efficiency of filter cake clean up.

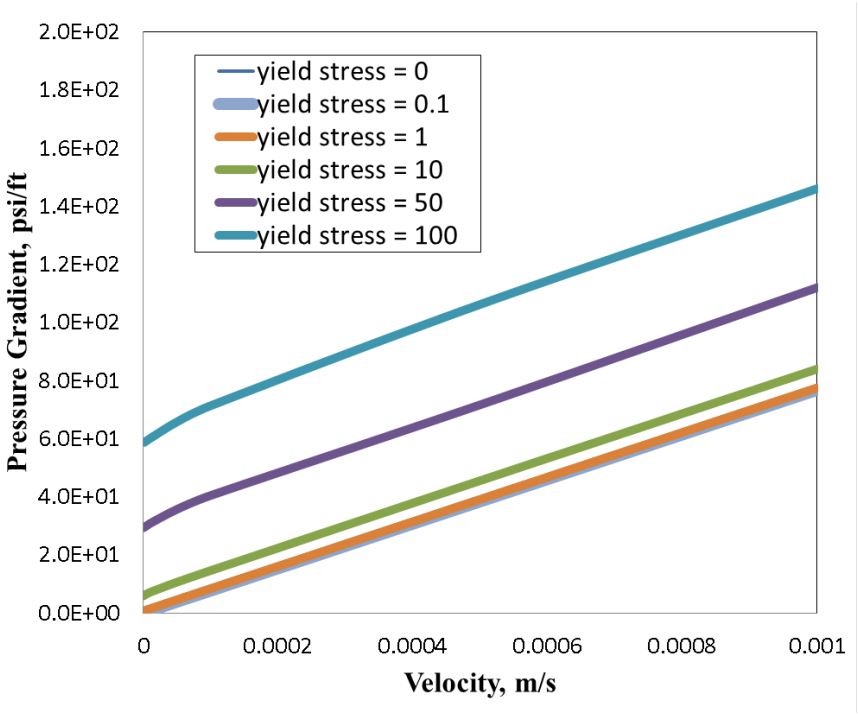

Fig. 3.16—Pressure gradient vs. superficial velocity for Bingham fluids.

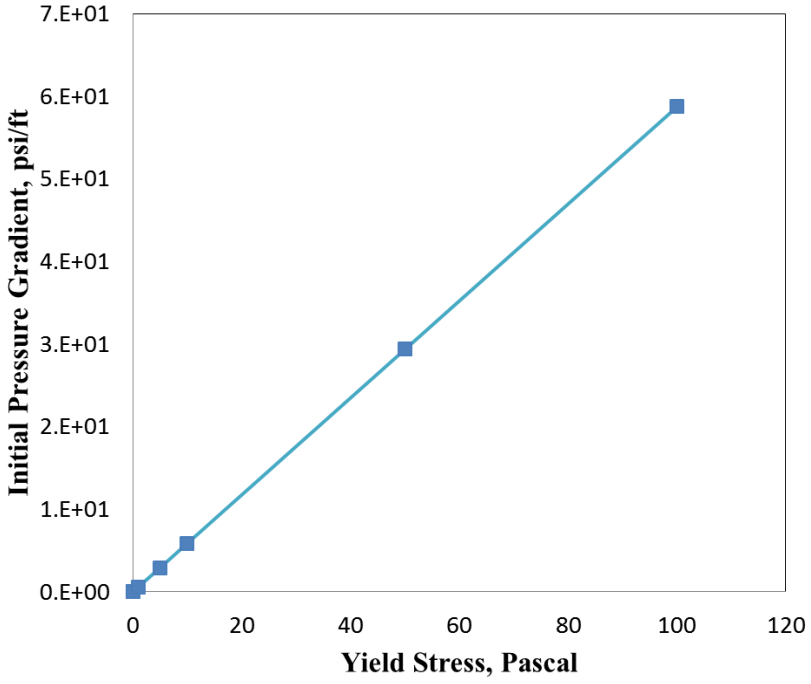

Fig. 3.17—Flow initiation gradient vs. yield stress for Bingham fluids.

Fig. 3.18 shows the velocity contour and profile for Bingham fluids with different yield stress at the narrowest part of a pore throat of the porous pack of simple cubic arrangement. Fig. 3.18d summarizes the velocity profiles for these fluids along the maximum straight line at the narrowest pore throat. As seen in the figure, the yield stress has significant influence on the velocity profile. The maximum velocity is reduced sharply when the yield stress increases from 1 to 10Pa. The yield stress leads to a discontinuity of the velocity derivative and a completely constant velocity zone at the center of the pore. From both the velocity contour map and the velocity profile, we can find that increasing initial yield stress enlarges the solid-plug flow zone and reduces the maximum velocity.

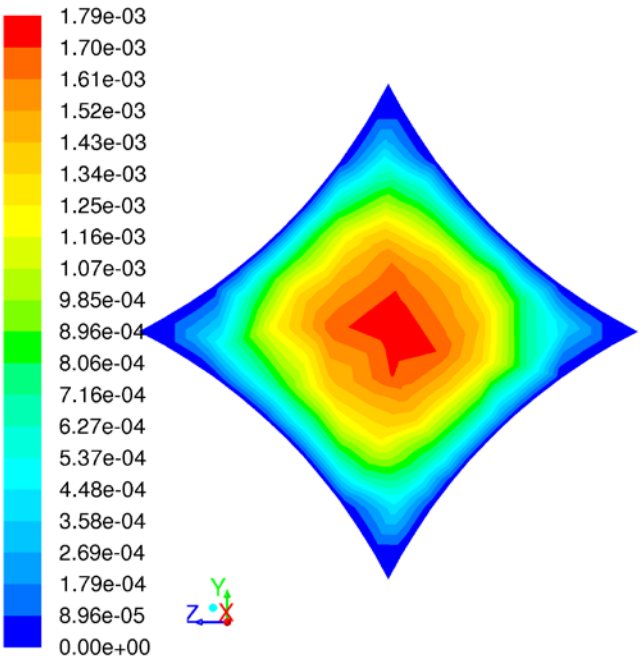

(a)

Fig. 3.18—Flow characteristic of a Bingham fluid at the cross section of the throat. (a) Velocity contour (yield stress = 1). (b) Velocity contour (yield stress = 10). (c) Velocity contour (yield stress = 100). (d) Comparison of velocity profile.

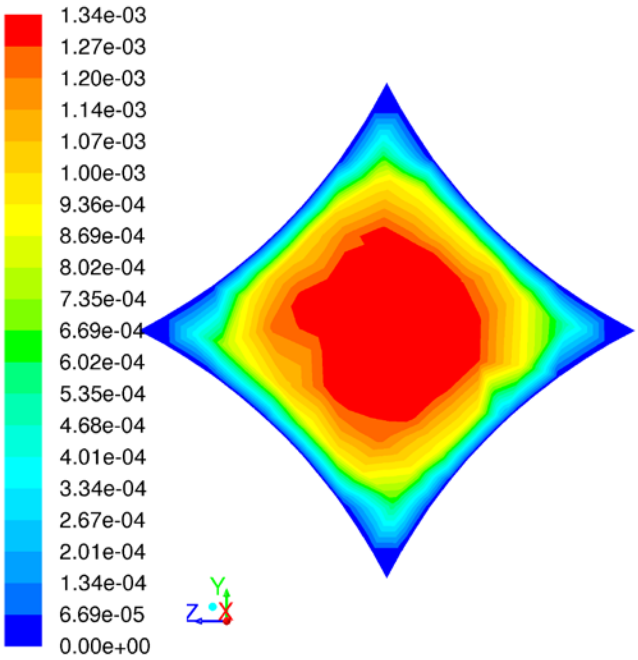

(b)

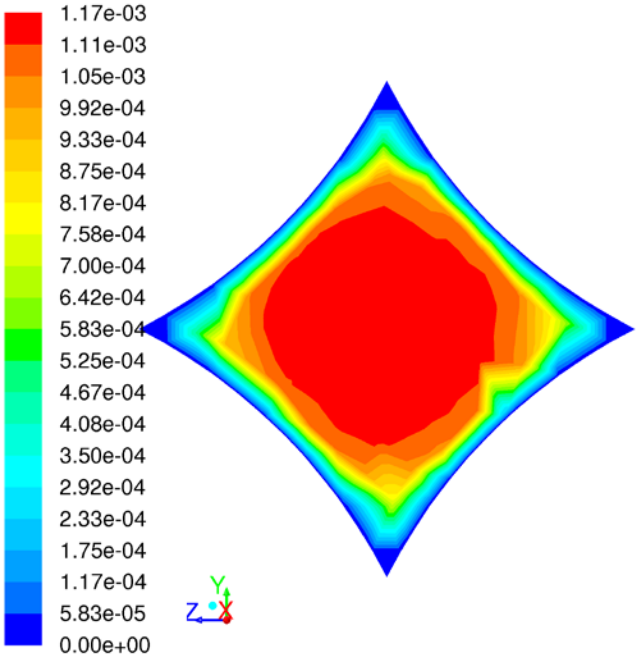

(c)

Fig. 3.18—Continued.

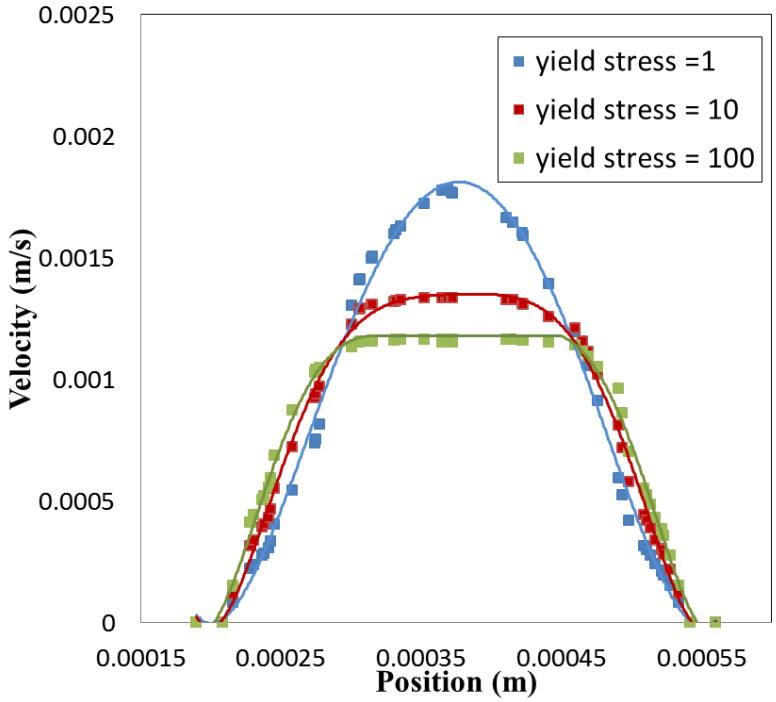

(d)

Fig. 3.18—Continued.

3.2.8 Effect of Proppant Diameter

We considered four typical mesh sizes, namely 20, 40, 70 and 100 meshes, and the corresponding proppant diameters are 0.84 mm, 0.42 mm, 0.21 mm, and 0.149 mm. **Fig. 3.19** shows the influence of the yield stress on the flow initiation pressure gradient with varying proppant diameter. Initial yield stress increases from 0 to 100 Pa. The result shows that the flow initiation pressure gradient has an inverse linear relationship with proppant diameter. The effective radius has a linear relationship with proppant diameter.

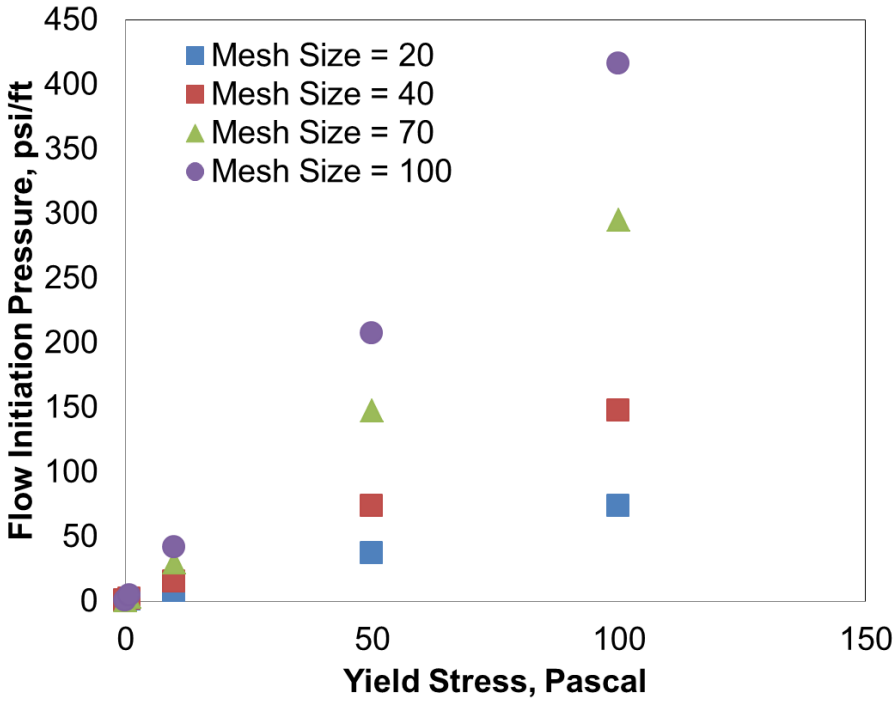

Fig. 3.19— Flow initiation pressure gradient vs. yield stress for varying proppant mesh sizes.

3.2.9 Effect of Proppant Arrangment

We studied three different proppant arrangements: simple cubic (SC), body center cubic (BCC), and face center cubic (FCC). We also studied the flow behavior of non-Newtonian fluid in porous media of BCC comprising two different proppant diameters (BCC2). For BBC2, the ratio of diameter of large proppant to small proppant is 2. **Fig. 3.20** compares the numerical results of the pressure gradient of power-law, Bingham, Herschel-Bulkley fluid flows in porous media of the packing arrangements of SC, BCC, FCC and BCC2. The results show that the proppant packing pattern has a large effect on the pressure gradient. The proppant packing pattern not only can change

the flow initiation pressure gradient, but also influence the increasing rate of the pressure gradient. For the fixed Darcy velocity, if all other factors keep the same, the Simple Cubic packing arrangement always require the lowest pressure gradient. This is due to the largest flow channel between the proppants. Face Center Cubic packing arrangement has the largest pressure gradient, because FCC structure divides the space into many small parts. For the same packing arrangement BCC, the uniform proppant requires smaller pressure gradient, comparing with two different diameters. The proppant arrangements in the porous media influence the non-Newtonian fluid flow due to the different pore structure. The pore structure determines the shear stress distribution, and the viscosity of non-Newtonian fluid strongly depends on the stress distribution. It is observed that the proppant packing arrangement has great influence on the flow behavior of non-Newtonian.

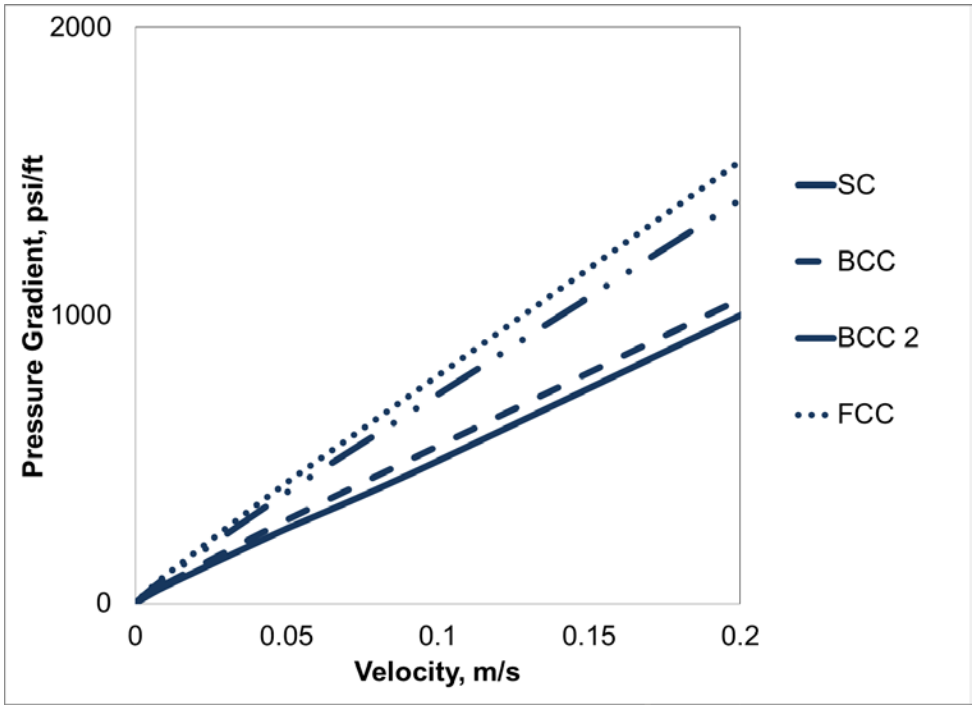

(a)

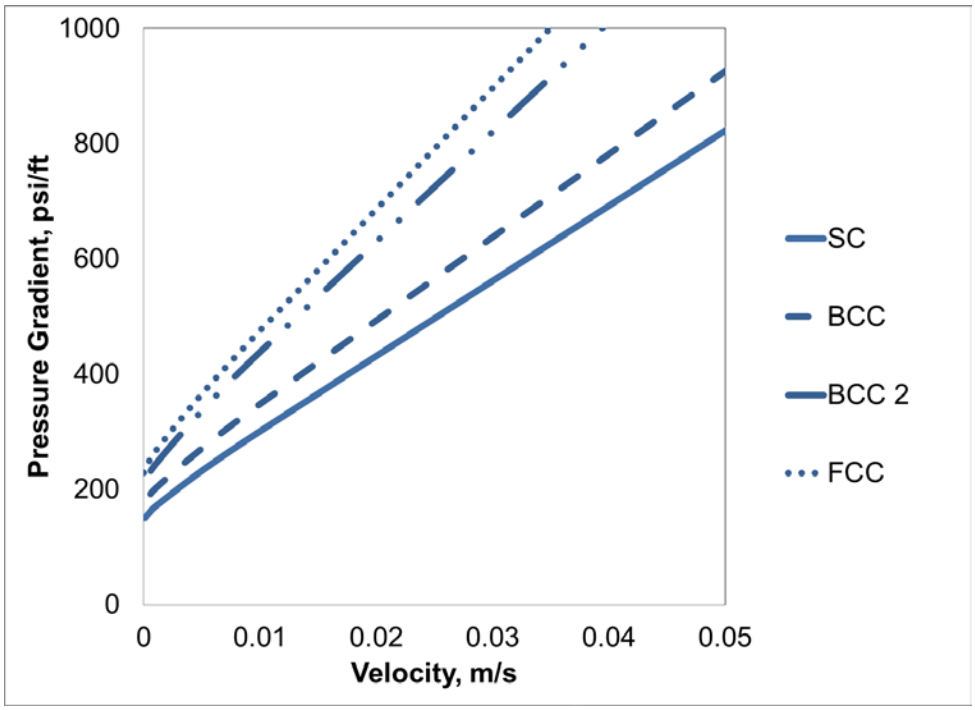

(b)

Fig. 3.20—Comparison of pressure gradient for non-Newtonian fluids flows in different proppant arrangements. (a) Power law fluid (Power-Law index = 0.9). (b) Bingham fluid (Initial yield stress = 200 Pascal). (c) Herschel-Bulkley fluid (Power-Law index = 0.8 & Initial yield stress = 100 Pascal).

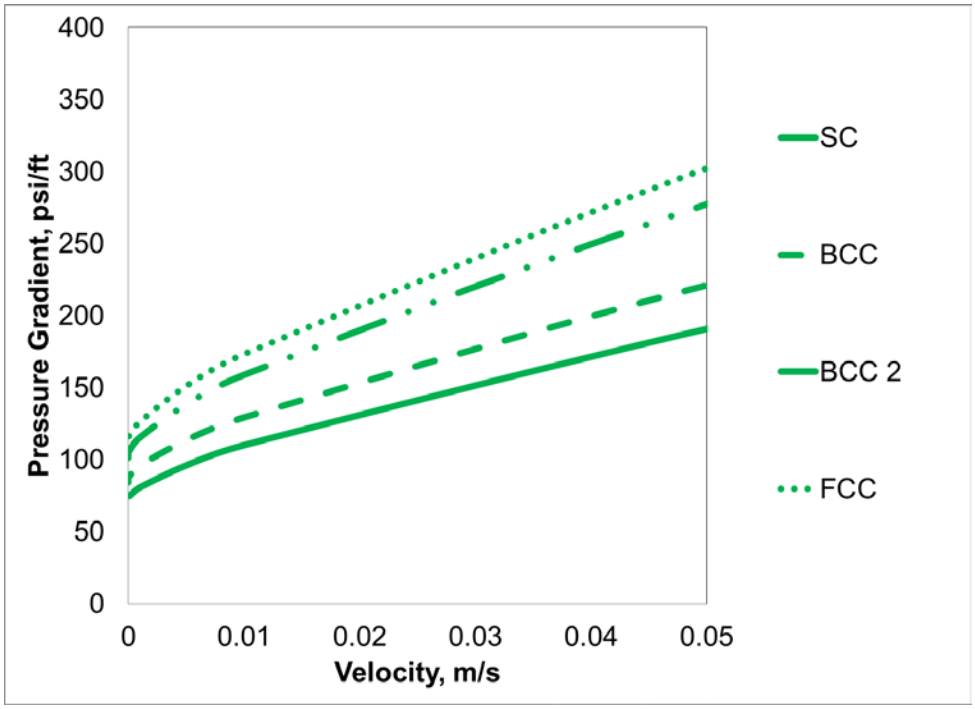

(c)

Fig. 3.20—Continued.

3.3 Mathematical Model for Herschel-Bulkley Fluid Flow in Porous Media

Modeling of non-Newtonian fluid flow in porous media is difficult because of the complexity of rheology of non-Newtonian fluid and the complication of the microscopic pore structure in porous media. We used the approach of bundle of capillary tubes to derive the Herschel-Bulkley fluid flow equation in porous media. In the capillary bundle model, the flow channels in a porous media are assumed as a bundle of capillary tube, as shown in **Fig. 3.21**. Fig. 3.21a shows the actual flow channel in porous media. The flow channels are desultory and difficulty to be described. They usually have different flow directions, diameters, path lengths and shapes of cross section. Fig. 3.21b shows the imaginary flow channel in capillary bundle model. We assumed that the

capillary tubes are straight, cylindrical and parallel. To successfully represent the real flow channel in Fig. 3.21a, the critical step is to find the accurate radius of the tube in capillary bundle model. Actually, the accurate radius cannot be analytical solved because of the coupling effect of pore structure in porous media and rheology of fluid. Hence, we use the numerical simulation results to find out the equation for the effective radius.

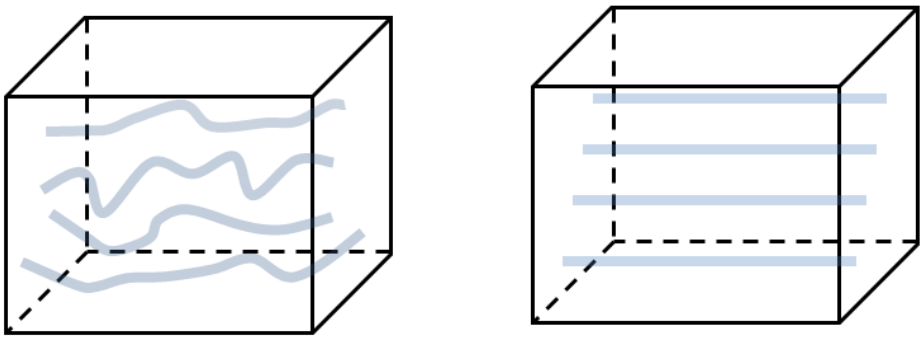

Fig. 3.21— (a) Actual flow channel in porous media (b) Suppositional flow channel in capillary bundle model.

3.3.1 Shear Stress Distribution in Capillary Tube

The schematic of the force balance on a small fluid element in a capillary tube is shown in **Fig. 3.22**. The assumptions for the physical model for Herschel-Bulkley fluid flow in tube include laminar, incompressible, steady-state, isothermal, and fully-developed flow.

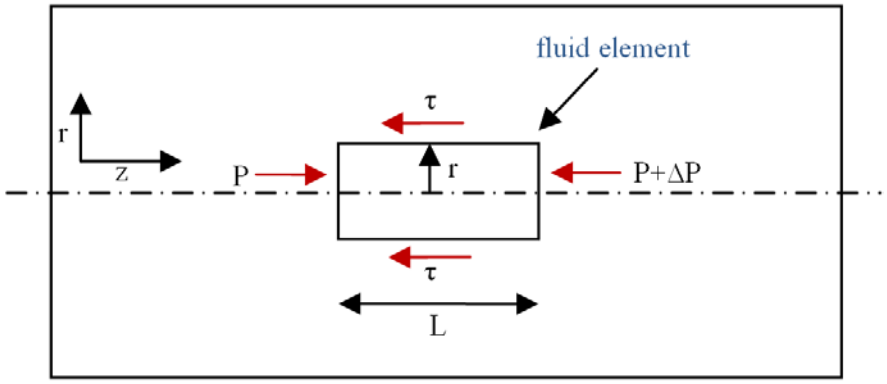

Fig. 3.22—The force balance on the fluid element in capillary tube flow.

The equation for force balance in the z-direction on a small fluid element located at the distance, *r*, from the center can be written as:

$$p \cdot \pi r^2 = (p + \Delta p)\pi r^2 + \tau 2\pi r L \tag{3.8}$$

So based on the force balance law, the shear stress distribution in tube can be written as:

$$\tau = \frac{-\Delta p}{L}\frac{r}{2} \tag{3.9}$$

This equation shows that the shear stress has a linear distribution across the capillary tube cross-section, as shown in **Fig. 3.23a**. The shear stress is zero at the center of the tube and reaches a maximum value at the wall of the tube.

3.3.2 Herschel-Bulkley Fluid Flow Equations in Capillary Tube

Combining the Herschel-Bulkley fluid rheological equation, Eq. 3.1, with the shear stress distribution equation (Eq. 3.9), and the appropriate boundary conditions, we can attain the generally expression for the velocity profile in the capillary tube as

$$v_{HB}(r)=\begin{cases}\dfrac{(AR-B)^{1+\frac{1}{n}}}{A\left(1+\dfrac{1}{n}\right)} & |\tau|<\tau_0 \\ -\dfrac{(Ar-B)^{1+\frac{1}{n}}}{A\left(1+\dfrac{1}{n}\right)}+\dfrac{(AR-B)^{1+\frac{1}{n}}}{A\left(1+\dfrac{1}{n}\right)} & |\tau|\geq\tau_0\end{cases} \tag{3.10}$$

with

$$A=\frac{-\Delta p}{2CL},\qquad B=\frac{\tau_0}{C} \tag{3.11}$$

where $-\Delta p$ is the pressure drop, L is the length of the porous media, C is the consistency factor of the filter cake, τ_0 is the initial yield stress, τ is the shear stress and R is the radius of the capillary tube.

Fig. 3.23a shows the shear stress distribution in a capillary tube. The velocity profile for Herschel-Bulkely fluid is shown in **Fig. 3.23b**. The characteristic feature for the Herschel-Bulkley fluid flow is that there is a solid plug-like core flowing in the middle of the tube where the shear stress is less than the yield stress. For the region $R_{YS}<r<R$, the velocity increases from zero at the tube wall to the plug velocity at R_{YS}. R_{YS} is the position of the interface of yielded and unyielded of Herschel-Bulkley fluid. At this location, the shear stress in fluids is equated to the yield stress. So the expression for R_{YS} can be attained as below:

$$R_{YS}=\frac{2\tau_0 L}{-\Delta p} \tag{3.12}$$

To initiate a Herschel-Bulkley fluid to flow, the maximum shear stress in capillary tube must be larger than the yield stress. So we can get the flowing condition of pressure gradient for a Herschel-Bulkley fluid, as shown in **Eq. 3.13**.

$$-\frac{\Delta p}{L} > \frac{2\tau_0}{R} \tag{3.13}$$

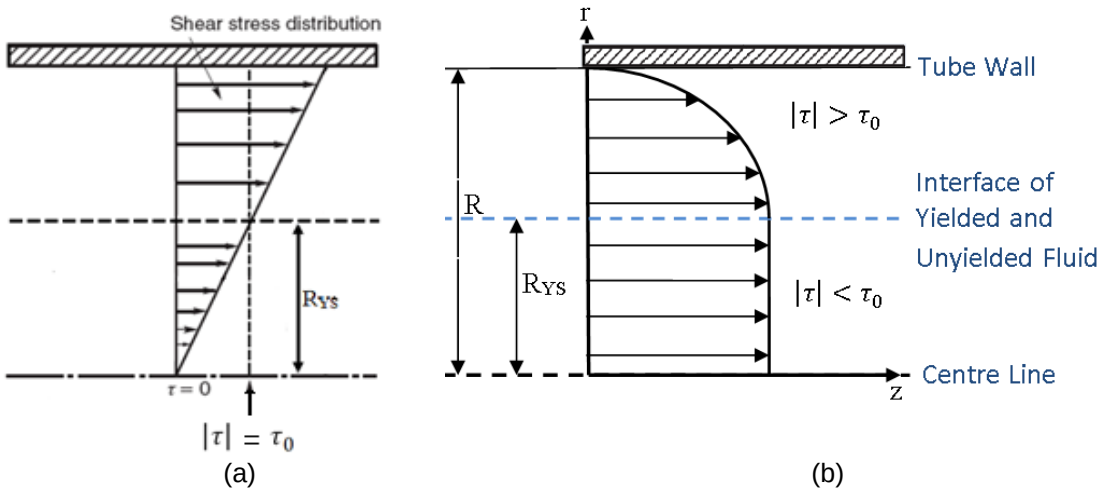

Fig. 3.23— Tube Flow Patterns for Herschel-Bulkley Fluid. (a) Shear stress distribution in tube. (b) Velocity profile of Herschel-Bulkley fluid.

By integrating the velocity profile over the entire of tube size, the mean velocity through a single capillary for a Herschel-Bulkley fluid is obtained, **Eq. 3.14**. The detail derivation for the mean velocity is in Appendix B.

$$\bar{u}_{HB} = \frac{(AR-B)^{1+\frac{1}{n}}}{A\left(1+\frac{1}{n}\right)} - \frac{2(AR-B)^{2+\frac{1}{n}}}{A^2R\left(1+\frac{1}{n}\right)\left(2+\frac{1}{n}\right)} + \frac{2(AR-B)^{3+\frac{1}{n}}}{A^3R^2\left(1+\frac{1}{n}\right)\left(2+\frac{1}{n}\right)\left(3+\frac{1}{n}\right)} \tag{3.14}$$

To make the equation simpler, we introduce a dimensionless yield stress variable

$$\alpha = \frac{2\tau_0 L}{-R\Delta p} \tag{3.15}$$

to Eq. 3.14. The equation becomes

$$\begin{aligned}\bar{u}_{HB} &= (AR-B)^{\frac{1}{n}} R\left[\frac{1-\alpha}{\left(1+\frac{1}{n}\right)} - \frac{2(1-\alpha)^2}{\left(1+\frac{1}{n}\right)\left(2+\frac{1}{n}\right)} + \frac{2(1-\alpha)^3}{\left(1+\frac{1}{n}\right)\left(2+\frac{1}{n}\right)\left(3+\frac{1}{n}\right)}\right] \\ &= (AR-B)^{\frac{1}{n}} R f(\alpha)\end{aligned} \tag{3.16}$$

3.3.3 Correlation between Tube Flow and Porous Media Flow

From the interstitial fluid velocity $\bar{u}$, we can get the Darcy velocity through the porous media by the following equation:

$$\bar{u}_{Darcy} = \bar{u}\phi \tag{3.17}$$

For the capillary bundle model approach, the average radius of the flow tube is related with the permeability and porosity of the porous media. The step of transferring tube flow to porous-media flow is the important step for a capillary bundle model. In previous papers, most of the correlations are based on the Kozeny equation or its derivatives. The Kozeny equation, **Eq. 3.20**, is developed by combining Poiseuille's equation, **Eq. 3.18**, and Darcy's law, **Eq. 3.19**.

$$q = \left(\frac{n\pi R^4}{8\mu}\right)\frac{-\Delta p}{L} \tag{3.18}$$

$$q = \left(\frac{k}{\mu} \frac{n\pi R^2}{\varphi} \right) \frac{-\Delta p}{L} \tag{3.19}$$

$$R = \left(\frac{8k}{\phi} \right)^{\frac{1}{2}} \tag{3.20}$$

The Kozeny equation essentially creates an equivalent bundle of tubes that has the same permeability as the porous media, and the concept and process of derivation are based on Newtonian fluid. First, the Poiseuille's equation, Eq. 3.18, assumes that the fluids behave as Newtonian fluids and have a constant viscosity independent of the flow rate. Second, in Darcy's law, Eq. 3.19, the apparent viscosity is equated to the viscosity in the rheology equation of fluids, which is true only for Newtonian fluids. So the family of Kozeny equations is only suitable for Newtonian fluid flow. Many previous works did not identify these two concepts in their correlation developments. Christopher and Middleman (1965) derived the equation of the capillary diameter and the particle diameter based on Newtonian fluids flow. They applied it to power law fluids in the bundle of tube approximation. Teeuw et al (1980) directly introduced the Kozeny equation to express the equivalent capillary radius of a porous media for a power law fluid. Al-Fariss and Pinder (1987) developed a modified Blake-Kozeny equation for Herschel-Bulkley fluid flow in porous medium by intruding a definition of the permeability of the porous medium. The authors attained the definition of the permeability by combining Darcy's Law and Blake-Kozeny equation, both of which describe laminar flow of Newtonian fluids. In the derivation of the viscosity equation for Herschel-Bulkley fluid flow in porous media, May et al (1997) related the hydraulic

radius in capillary tubes and hydraulic radius in porous media, which was also based on Newtonian fluid flow. Wang et al (2006) developed a theoretical expression for the pressure gradient for heavy oil flow in porous media using the Kozeny equation. To get the equation for Herschel-Bulkley fluid flow in porous media, Friedel (2006) combined the Carmen-Kozeny equation and the correlation of hydraulic radius and the mean diameter for the porous medium. There are a large number of papers using capillary bundle approach to modeling non-Newtonian fluids flow in porous media, including the Power law model (Bird et at 1960), the Bingham model (Vradis and Protopapas, 1993; Chase and Dachavijit, 2003) and Herschel-Bulkley model (Park, 1972).

The average velocity for a laminar porous-media flow of fluids is given by Darcy's law:

$$\bar{u}_{Darcy} = \frac{k}{\mu}\frac{-\Delta p}{L} \tag{3.21}$$

If we combine equations 3.14, 3.17 and 3.21, we have two unknowns, the effective radius of the capillary tube and the apparent viscosity for a non-Newtonian fluid. There is not enough information to analytically solve the equations. We need to use another way to determine the effective radius or other empirical parameter. In fact, the rheological behavior of non-Newtonian fluid depends on the pressure drop and the pore structure. The flow rate of non-Newtonian fluids depends on the coupling effect of the pressure drop, the rheological behavior of the fluid and the geometry of the porous media. So, the effective radius of a capillary tube should depend on these parameters. It may be possible that the best way to achieve the exactly empirical solution is to use

these variables and data in numerical simulation. First, we find the correlation between pressure gradient and velocity for a large range of parameters from the extended numerical experiments. Then, we used the numerical results in the mean velocity equation of capillary tube to determine the equivalent radius. After having the effective equation, we can attain the flow rate equation. To incorporate the model in reservoir simulator in the future, we use the concept of apparent viscosity for non-Newtonian fluids in Darcy's Law and keep the same definition of permeability as used for Newtonian fluids.

3.3.4 Correlation of Effective Radius

Numerical simulation in the study covers a large range of parameters, including pressure gradient, velocity, proppant diameter and rheological properties of a Herschel-Bulkley fluid. Using the empirical correlation for the effective radius derived from the numerical simulations, the flow equations for a non-Newtonian fluid in porous media can closely match the results from numerical simulation. Some correlations of effective radius are shown and discussed below.

Power Law Fluid. The analytical expression for the mean velocity of laminar flow of a power law fluid in capillary tube can be attained by choosing the appropriate parameter for Eq. 3.14. The result is,

$$\bar{u}_{PL} = \left(3 + \frac{1}{n}\right)^{-1} \left(\frac{-\Delta p}{2CL}\right)^{1/n} R^{1+1/n} \tag{3.22}$$

Based on the CFD simulation results, we get the effective radius correlation equation for a power law fluid as

$$R_{eff,PL} = d\left(a_1 n + a_2\right) \tag{3.23}$$

where n is the power law index and d is the proppant diameter. a_0, a_1 and a_2 are constant depending on the way of proppant packing arrangement.

TABLE 3.3—CORRELATION CONSTANTS FOR POWER LAW FLUID

Proppant Arrangement	a_1	a_2
SC	-0.0504	0.1122
BCC	-0.03841	0.09743
BCC2	-0.03266	0.08346
FCC	-0.02844	0.07727

Table 3.3 presents the correlation constants of the effective radius for the power law fluid flowing in porous media of different proppant arrangements. These constants are determined by fitting Power-law fluid flow equation, Eq. 3.22, with numerical simulation results.

Fig. 3.24a shows the fitting curve for the correlation of the power law index and the ratio of the effective radius to the proppant diameter. **Fig. 3.24b** shows the comparison of the pressure gradient from numerical simulation and our theoretical equation under various conditions for Power-law fluid. From Fig. 3.24b, the analytical prediction model shows good agreement with CFD simulation results. For this curve fitting in Fig. 3.24a, the sum squared error (SSE) is 6.7797e-5 and the coefficient of determination R^2 is 0.9922.

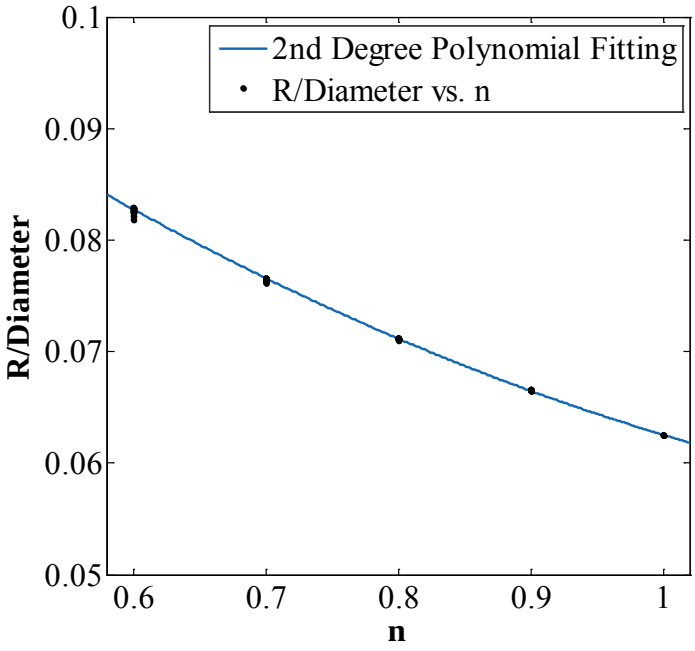

(a)

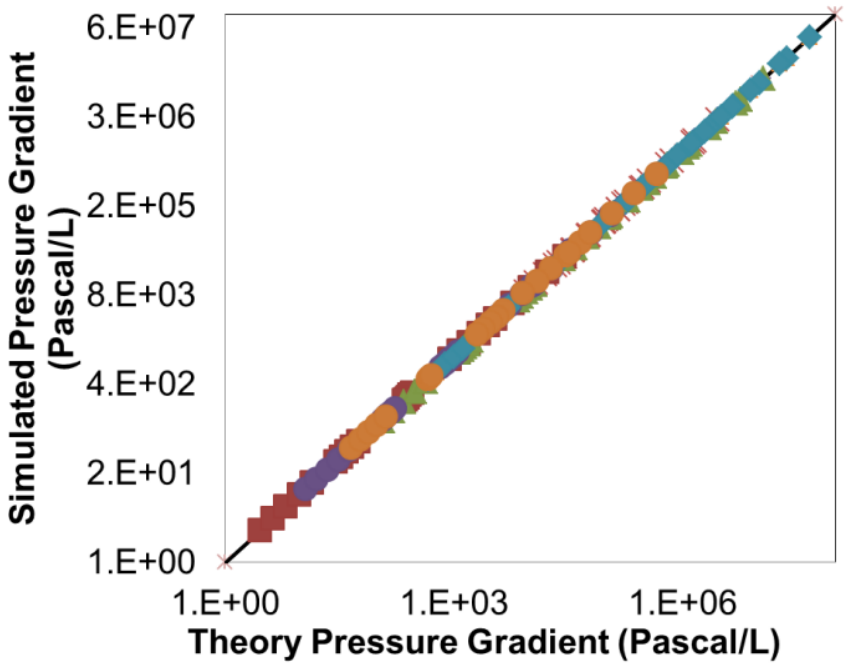

(b)

Fig. 3.24— Comparison with CFD simulation data for Power Law Fluid. (a) Curve fitting of effective radius. (b) Comparison of pressure gradient.

Bingham Fluid. Similarly, we can attain an analytical expression for the mean velocity for laminar flow of a Bingham fluid in a capillary tube, as shown in **Eq. 3.24**.

$$\overline{u}_B = \frac{-\Delta p}{8CL} R^2 \left[1 - \frac{4}{3}\left(\frac{2L\tau_0}{-\Delta pR} \right) + \frac{1}{3}\left(\frac{2L\tau_0}{-\Delta pR} \right)^4 \right] \tag{3.24}$$

This is a quadratic equation. We calculated the effective radius using the value of velocity and pressure gradient from CFD simulation results, and then used cubic polynomial to fit the effective radius. For a Bingham fluid, the ratio of the yield stress to pressure drop is an index for the effect of the yield stress on the flow behavior. So the equivalent radius must be a function of this dimensionless parameter.

$$R_{eff,B} = d\left[b_1 \left(\frac{\tau_0}{-\Delta p} \right)^2 + b_2 \frac{\tau_0}{-\Delta p} + b_3 \right] \tag{3.25}$$

TABLE 3.4—CORRELATION CONSTANTS FOR BINGHAM FLUID

Proppant Arrangement	b_1	b_2	b_3
SC	-6.779	10.68	0.06141
BCC	17.83	6.412	0.05877
BCC2	-39.36	5.092	0.05306
FCC	-8.323	7.464	0.04861

Table 3.4 presents the correlation constants of the effective radius for Bingham fluids flowing in porous media of different proppant arrangements.

Fig. 3.25a shows the ratio of the numerical effective radius to proppant diameter versus dimensionless parameter $\tau_0/(-\Delta p)$. As seen in the graph, our effective radius equation closely matches the results from CFD. **Fig. 3.25b** shows the comparison

between the numerical effective radius and theoretical effective radius from Eq. 3.25. The sum squared error is 3.7569E-4 and the coefficient of determination R^2 is 0.9986.

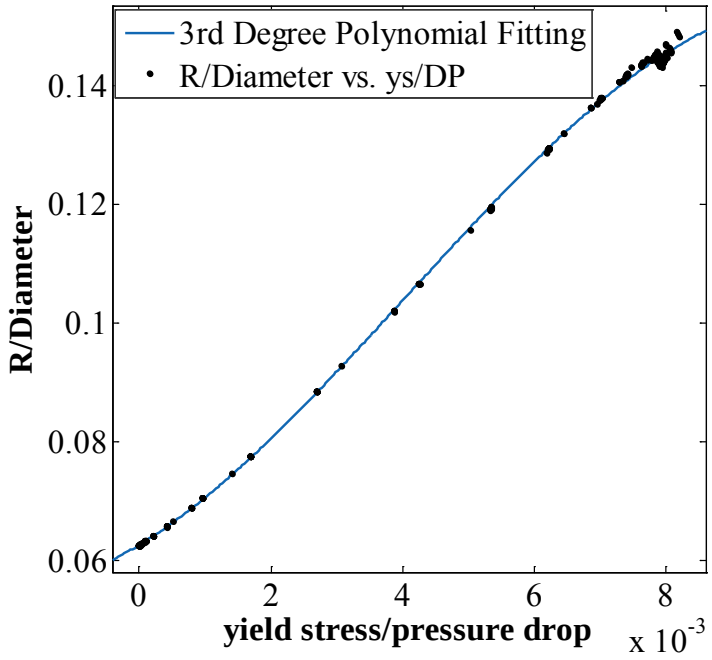

(a)

Fig. 3.25— Comparison with CFD simulation data for Bingham Fluid. (a) Curve fitting of effective radius. (b) Comparison of effective radius.

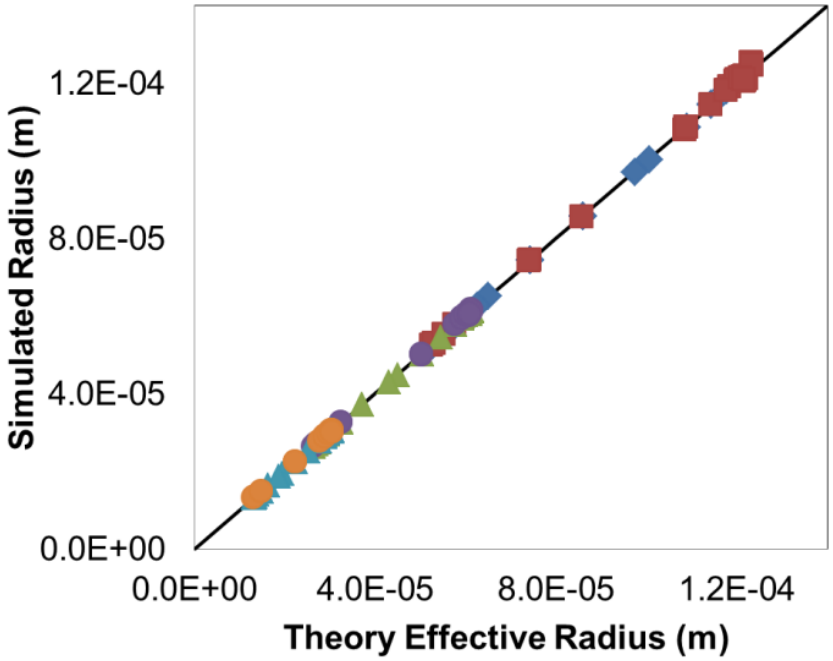

(b)

Fig. 3.25— Continued.

Herschel-Bulkley Fluid. The analytical expression for the mean velocity of laminar capillary-tube flow of a Herschel-Bulkley fluid has been shown in Eq. 3.14. To derive in a simplified way, we neglected the higher order terms in the term of $f(\alpha)$ and attained **Eq. 3.26**.

$$\bar{u}_{HB} = \left(3 + \frac{1}{n}\right)^{-1} \left(\frac{-\Delta p}{2CL} R - \frac{\tau_0}{C}\right)^{1/n} R \qquad (3.26)$$

If $\tau_0 = 0$, this equation simplifies to the power law fluid flow equation, Eq. 3.22. If $n = 1$, the equation simplifies to the following equation:

$$\bar{u}_{HB} = \frac{-\Delta p}{8CL} R^2 \left(1 - \frac{2\tau_0 L}{-\Delta p R}\right) \qquad (3.27)$$

Comparing with Bingham fluid flow equation, Eq. 3.24, there is a small difference in the coefficient of dimensionless yield stress parameter α (Eq. 3.15) and Eq. 3.27 misses the four order of α. If the dimensionless yield stress parameter is close to 1, the two equations are almost the same. If the dimensionless yield stress is much smaller than 1, the term including the dimensionless yield stress parameter is reasonable to be omitted. For this case, Eq. 3.27 simplifies to the Bingham fluid flow equation with a slight error. In our method, we calculated effective radius based on this flow equation using the numerical results. After that, we combined this equation with the fitting correlation for the effective radius. Therefore, our model can exactly predict the flow behavior.

We used the power law index *n* and the ratio of the yield stress to pressure drop $\tau_0/(-\Delta p)$ as two variable quantities in the effective radius equation for a Herschel-Bulkley fluid. As before, based on the CFD simulation results, we achieve the effective radius correlation equation:

$$R_{eff,HB} = d\left[c_{00} + c_{10}n + c_{01}\frac{\tau_0}{-\Delta p} + c_{02}\left(\frac{\tau_0}{-\Delta p}\right)^2\right] \tag{3.28}$$

TABLE 3.5—CORRELATION CONSTANTS FOR HERSCHEL-BULKLEY FLUID

Proppant Arrangement	c_{00}	c_{10}	c_{01}	c_{02}
SC	0.0907	-0.02327	3.525	658.9
BCC	0.0811	-0.01693	1.479	389.5
BCC2	0.0693	-0.01439	1.135	298.9
FCC	0.0658	-0.01329	1.448	712.3

Table 3.5 presents the correlation constants of the effective radius for Herschel-Bulkley fluid flow in porous media of different proppant arrangements.

The fitting surface for the effective radius for Herschel-Bulkley fluids is a cubic equation in two variables. The sum squared error is 5E-4 and the coefficient of determination R^2 is 0.9932. The highest degree for power law index n is 2 and for $\tau_0/(-\Delta p)$ is 3. This refers to previous effective radius equations for power law and Bingham fluids. In three dimensional graph, **Fig. 3.26a** shows the numerical effective radius versus power law index n and the dimensionless parameter $\tau_0/(-\Delta p)$. The results show that our effective radius equation, Eq. 3.28, can represent the surface that goes through almost all the data from numerical simulation. We also compare the theoretical effective radius with numerical simulated radius, as shown in **Fig. 3.26b**. The overall comparison with CFD simulation results shows good agreement with our model.

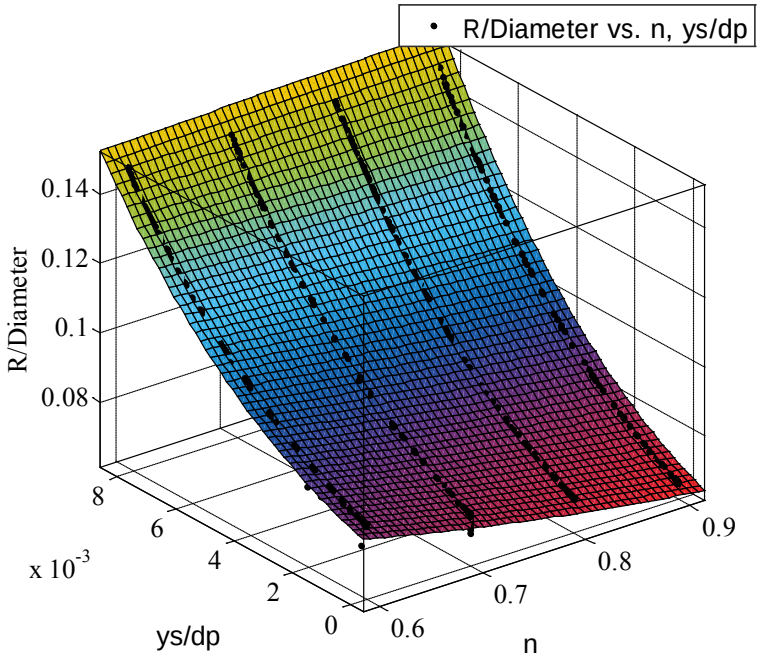

(a)

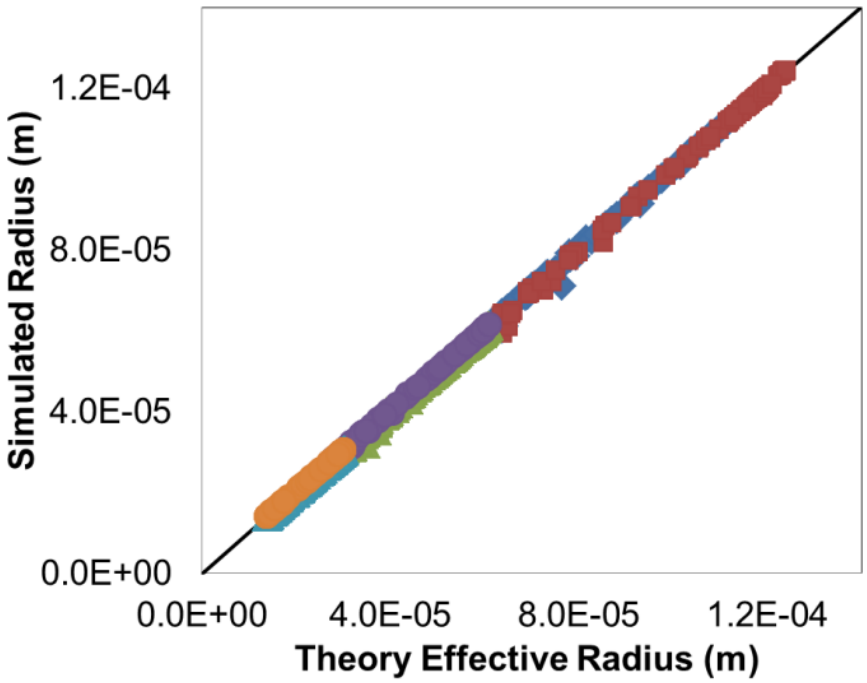

(b)

Fig. 3.26— Comparison with CFD simulation data for Herschel-Bulkley Fluid. (a) Surface fitting of effective radius. (b) Comparison of effective radius.

3.3.5 Apparent Viscosity

By substituting the effective radius equations into flow velocity equations, we can attain the flow equation for a laminar porous-media flow of non-Newtonian fluids. Thereafter, combining with Darcy's equation, and rearranging it, we obtain an equation for the apparent viscosity of a non-Newtonian fluid in porous media.

$$\mu_{app} = \left(3 + \frac{1}{n}\right) \frac{k}{\phi R} \frac{-\Delta p}{L} \left(\frac{-\Delta p}{2CL} R - \frac{\tau_0}{C} \right)^{-1/n} \tag{3.29}$$

This equation can be easily incorporated into reservoir simulator to describing non-Newtonian fluid flow, such as gel clean up in hydraulic fracturing or heavy oil recovery.

3.4 Discussion

At this section, I developed a mathematical model, and then corrected the model based on numerical simulation results. In the work we investigate non-Newtonian fluid behavior in porous media theoretically and numerically. We developed a mathematical model to describe the flow behavior of non-Newtonian fluids in a proppant pack. One of the parameters, the effective radius, in the model needs to be determined by regression analysis of the results from numerical simulation. In the mathematical model, the gel in the propped fractures is modeled as a Herschel-Bulkley fluid; in numerical simulation, the Herschel-Bulkley model is modified following Papanastasiou's recommendation to avoid numerical instability. In simulation cases, we studied a large range of important parameters to cover the common conditions in hydraulic fracturing.

The numerically predicted flow initiation pressure gradient rises rapidly with the increasing of the yield stress. The yield stress affects the Darcy velocity through two physical mechanisms. Compared with the shear-thinning fluid, the shear-thickening fluid requires much higher pressure gradient to attain the same Darcy velocity. Permeability has a quadratic relationship with proppant diameter, and the flow initiation pressure gradient is inversely proportional to proppant diameter. The pore scale study provides detailed observation of flow phenomenon and fundamental understanding of the mechanism of non-Newtonian fluid flow in porous media. We obtained a detailed view of the flow streamlines, the velocity field, and the pressure distribution in porous media. Numerical calculation results show that, in the center of the throats of porous media, the increasing yield stress widens the central plug-like flow region, and the increasing power law index sharpens the velocity profile.

The Kozeny-Carman equation, a traditional permeability-porosity relationship, has been popularly used in porous media flow models. However, this relationship is not suitable for non-Newtonian fluid flow in porous media. The result of the new model indicates that yield stress has a significant impact on non-Newtonian fluid flow through porous media, and the pressure gradient strongly depends on pore structure. The analytical expression reveals the physical principles for flow velocity in porous media. The variation trends of the threshold pressure gradient versus different influence factors are presented. The new model can be readily applied to provide a clear guide to selection of fracture fluid, and can be easily incorporated into any existing reservoir simulators.

CHAPTER IV

TWO PHASE FLOW IN PROPPED FRACTURE

4.1 Introduction

In Chapter III, we simplify the physical problem to focus on single-phase non-Newtonian porous-media flow to investigate the effect of rheological parameters, proppants sizes and packing arrangements. In practical environment, the problems usually involve multi-phase flow, leading to much more complex. In the chapter IV, we investigated the flow behavior of multi-phase non-Newtonian fluid in porous media through the methods of mathematical modeling and numerical simulation.

As described in previous chapters, in propped fractures, there has the residual gel between the proppants and the filter cake deposited on the fracture walls. This will lead to seriously gel damage problem and reduce gas production rate and reserves. The filter cake has a higher polymer concentration, so it has a different flow behavior than the original gel under the same pressure gradient.

In this chapter, we first investigate the transient multi-phase flow behavior of the original gel and the filter cake in propped fracture at the pore scale. Numerous simulations have been performed based on the methods introduced in the previous chapters. In this chapter, we used the method of the Volume of Fluid (VOF) to deal with the multi-phase flow problem. In CFD, VOF method is used to track the fluid-fluid interface and it belongs to the class of Eulerian methods. From the numerical simulation study of three-phase porous-media flow, the flow of the original gel and the filter cake have small influence on each other, if the filter cake has a much higher concentration.

After the verification of the cleanup mechanism for non-Newtonian fluid in Porous Media, we developed a micro pore-scale model to mimic the porous structure and ran a serial of simulation cases of non-Newtonian fluid displaced by Newtonian fluid. The relationship between the relative permeability and the water saturation was investigated under the influence of variable physical properties for non-Newtonian fluid, proppant packing arrangement and proppant diameter. The pore scale study provides detailed observation of flow phenomenon and fundamental understanding of the mechanism of multi-phase displaced flow in porous media.

To make the model more applicable, an analytical model was developed to describe the flow behavior of residual polymer gel being displaced by gas in porous media. Non-Newtonian fluid, the residual gel or the filter cake, is displaced by Newtonian gas in porous media under different conditions. By introducing the capillary pressure, the mathematical model was developed based on the correlation of single-phase non-Newtonian flow in porous media, which was present in Chapter III. And then, the model was compared with the numerical simulation results developed in this chapter. Some parameters in the model need to be determined by regression analysis of the results from numerical simulation. Similar to single-phase problem, the residual gel in the propped fractures is modeled as a Herschel-Bulkley fluid in the analytical model; while in the numerical simulation, the residual gel is modeled as Herschel-Bulkley-Papanastasiou fluid. The result of the new model indicates that yield stress has a significant impact on non-Newtonian fluid flow through porous media, and the pressure gradient strongly depends on pore structure. The analytical expression reveals the

physical principles for flow velocity in porous media. The variation trends of the threshold pressure gradient versus different influence factors are presented. The new model can be readily applied to provide a clear guide to selection of fracture fluid, and can be easily incorporated into any existing reservoir simulators.

4.2 Volume of Fluid Method

We use the Volume of Fluid model in FLUENT for simulating immiscible multi-phase fluids flow. The Volume of Fluid method is one of the most important interfaces capturing technique that can deal with topology changes. This can eliminate the algorithmic complexity. VOF method can naturally conserves the mass balance of each phase.

In the VOF method, an indicator function is used to define the volume fraction of one phase on each grid through the domain, and the location of an interface is reconstructed by the volume fraction function. The integral of volume fraction of one fluid in the control volume can be calculated by the following equation.

$$0 \le \alpha_{ijk}^{n} = \frac{1}{\Delta x \Delta y \Delta z} \iiint_{(i,j,k)} \chi(x,y) dx dy dz \le 1 \tag{4.1}$$

The characteristic volume fraction function is shown below:

$$\begin{cases} \alpha_q = 0 & \text{The cell does not contain the } q \text{ fluid} \\ \alpha_q = 1 & \text{The cell is full of the } q \text{ fluid} \\ 0 < \alpha_q < 1 & \text{Otherwise} \end{cases} \tag{4.2}$$

In each computational cell, the sum of the volume fractions of all phases is unity.

$$\sum_{q=1}^{n} \alpha_q = 1 \tag{4.3}$$

The VOF method easily allows interfaces to merge or breakup. In VOF method, the interface between two phases is evolved on a fixed mesh by the solving a continuity equation for the volume fraction of each phase. For the phase q, the volume fraction equation is shown below:

$$\frac{1}{\rho_q}\left[\frac{\partial}{\partial t}\left(\alpha_q \rho_q\right) + \nabla \cdot \left(\alpha_q \rho_q \vec{v}_q\right) = S_{\alpha_q} + \sum_{p=1}^{n}\left(\dot{m}_{pq} - \dot{m}_{qp}\right)\right] \tag{4.4}$$

Here, ρ_q is the density of q phase; t is the time for unsteady problem; m_{pq} is the mass transfer from phase p to phase q; $S_{\alpha q}$ is the mass source for q phase.

When the explicit scheme is used for the time discretization, the finite difference interpolation scheme for Eq. 4.4 in FLUENT is shown as below:

$$\frac{\alpha_q^{n+1}\rho_q^{n+1} - \alpha_q^{n}\rho_q^{n}}{\Delta t} V + \sum_f \left(\rho_q U_f^{n} \alpha_{q,f}^{n}\right) = \left[\sum_{p=1}^{n}\left(\dot{m}_{pq} - \dot{m}_{qp}\right) + S_{\alpha_q}\right] V \tag{4.5}$$

Here, $n+1$ is for new time step, n is for previous time step, $\alpha_{q,f}$ is for the face value of the q volume fraction, V is for volume of the cell, U_f is the volume flux through the face, based on the normal velocity.

As shown in **Fig. 4.1**, in two dimensions case, the interface between two fluids consists of a serial of continuous, stepwise, smooth lines in each grid cell. It needs to use the volume fraction of each phase in a certain cell and neighbor cells to reconstruct the exactly location of the moving interface.

The critical point in the interface reconstruction is to determine the direction of each segment. That is equated to find the normal vector of the segment, n. The

characterization of the normal vector can be attained from the volume fraction in computational cell. By the finite different method, the normal vector can be attained by the **Eq. 4.5**.

$$n^h = \nabla^h \alpha \tag{4.6}$$

Calculating accurate the normal vector is a challenging problem, because the volume fraction of each numerical cell is discontinuous.

ANSYS FLUENT provides many options for the interface reconstruction near two phases. The geometric reconstruction scheme uses a Piecewise Linear Interface Calculation (PLIC) approach, which is the most accurate and applicable for general unstructured meshes. The PLIC algorithm is second order algorithm and allows the segments to be oriented indifferently. As shown in the figure, the reconstructed interface is a group of many unconnected piecewise linear segments with small discontinuities.

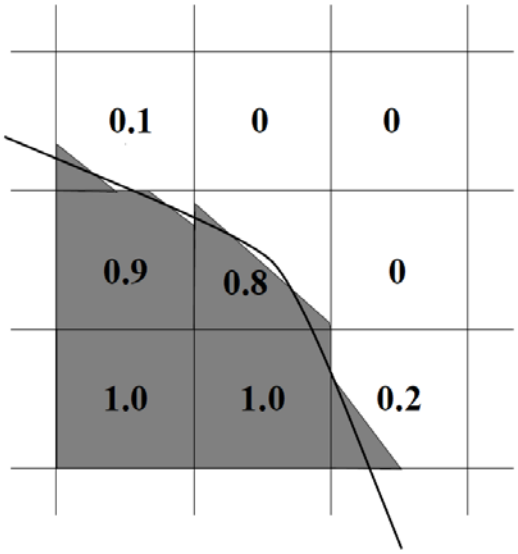

Fig. 4.1— The reconstruction of the interface with PLIC algorithms in VOF method with volume fraction.

In the geometric reconstruction at the interface of two fluids, we calculate the location of the linear interface relative to the center of each computational cell, based on the volume fraction and its derivatives. And then, using the linear interface representation and the normal and tangential velocity distribution on the face of the grids, the advection amount of one fluid through each face can be attained. Finally, the volume fraction in each cell can be achieved by using the balance of fluxes at the previous step.

The fluids share a single set of momentum equations throughout the domain in the VOF model. The velocity field is shared among all the phases. The momentum equation has the following form:

$$\frac{\partial}{\partial t}(\rho\vec{v}) + \nabla\cdot(\rho\vec{v}\vec{v}) = -\nabla p + \nabla\cdot\left[\mu\left(\nabla\vec{v} + \nabla\vec{v}^{T}\right)\right] + \rho\vec{g} + \vec{F} \qquad (4.7)$$

The VOF model also includes the effects of surface tension along the interface of two phases. The surface tension model in FLUENT is the Continuum Surface Force (CSF) model proposed by Brackbill (1992). The addition of the surface tension becomes a source term in the momentum equation. The pressure drop across the surface is shown below:

$$p_2 - p_1 = \sigma\left(\frac{1}{R_1} + \frac{1}{R_2}\right) \tag{4.8}$$

Here, p is the pressure in the fluid, σ is the surface tension coefficient. R is the surface curvature.

For more detail information about the model, please refer to FLUENT help document.

4.3 Cleanup Mechanism for Multi-Phase Flow in Porous Media

As mentioned in the previous chapters, in a hydraulic fracture, filter cake exists because the leak off of liquid phase of fracture fluid into the porous media. The filter cake exists full of the pore of the proppant pack near the surface of fracture wall after leak off. The filter cake is much more difficulty to be cleaned up than the original gel which exists in the center of the proppant pack. The physical flow process of the filter cake and the original gel cleanup in porous media is very complex and cannot be easily studied in laboratory experiments. We identify the details of the flow phenomenon by numerical simulation of three-phase transport at the pore scale in two dimensions using the computational fluid dynamics software package ANSYS FLUENT.

To numerically investigate the three-phase porous-media flow process, we modeled a small domain consisting of 180 proppant particles arranged in the body center cubic packing shown in **Fig. 4.2**.

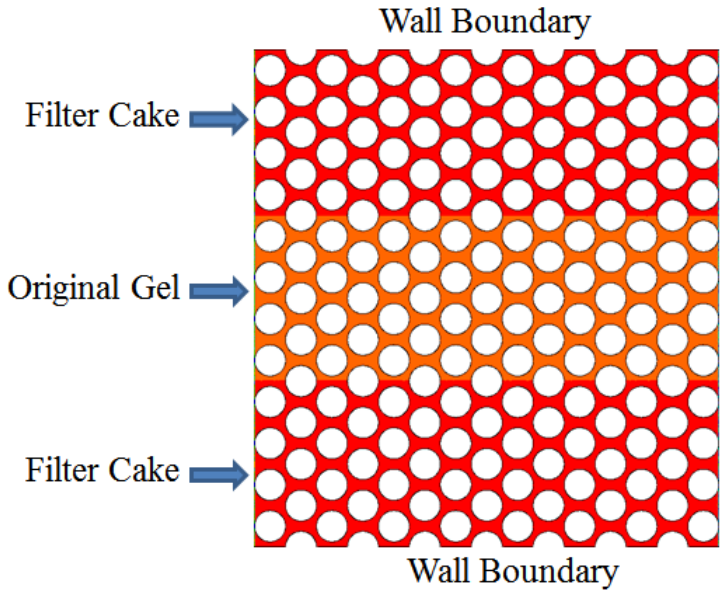

Fig. 4.2— The diagram for propped fracture fully of original gel and filter cake.

White circle stand for proppant particles which are fixed. The red color stands for the filter cake deposited on the fracture wall and the orange color stands for the original gel existed in the middle. The nominal particle sizes of the sintered porous channel are 20 mm. Gas flows from inlet at left side of flow domain to outlet at right side. Constant velocity boundary condition is used at the inlet and constant pressure condition at the outlet. No-slip condition was adopted on the fracture wall and the surface of proppant.

In the simulation, constant physical properties at 290 K and 50 psi are assumed for the gas in the grids.

The corresponding computational grid is shown in **Fig. 4.3**. The grid size is so small that there have many grids between the proppants. This will be helpful for capturing the flow characteristic of non-Newtonian fluids.

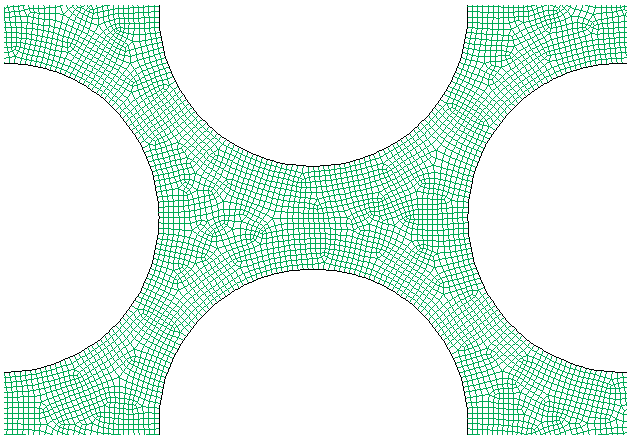

Fig. 4.3— Computational grids between the proppants.

The filter cake usually has a much higher initial yield stress and larger viscosity than the original gel. Under different pressure gradient circumstances, there may exist two flow patterns in porous media. At low pressure gradient, the value of the shear stress through the filter-cake region in porous media is smaller than the initial yield stress. The filter cake is completely immobile and only the original gel has been displaced by gas, as shown in **Fig. 4.4**. As seen from Fig. 4.4f, there still left some original gel between the proppants near the center. This really represents what happen in the experiment, which

can be observed from Fig. 1.6. The phenomenon of immobile filter cake also can be seen in experimental result, like Fig. 1.7. The remaining original gel usually happens at the narrowest part of the pore throat. The gas always tries to find the “easily” way to clean up the original gel. The easiest way is the channel which has the least resistance.

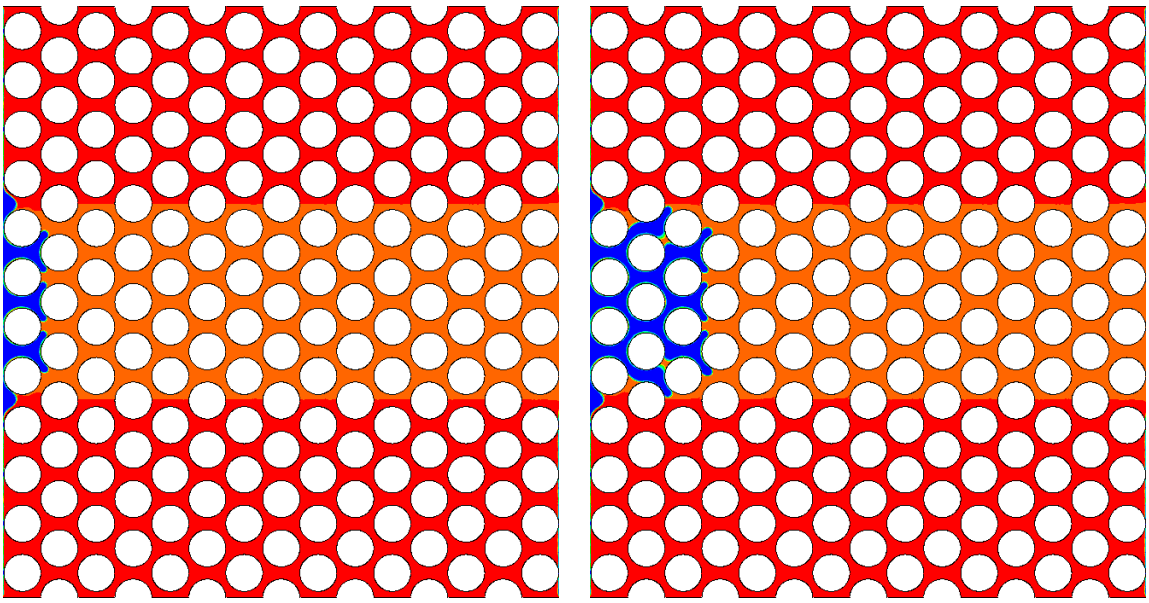

(a) (b)

Fig. 4.4— Displacement of the original gel and the filter cake in porous media (small pressure gradient).

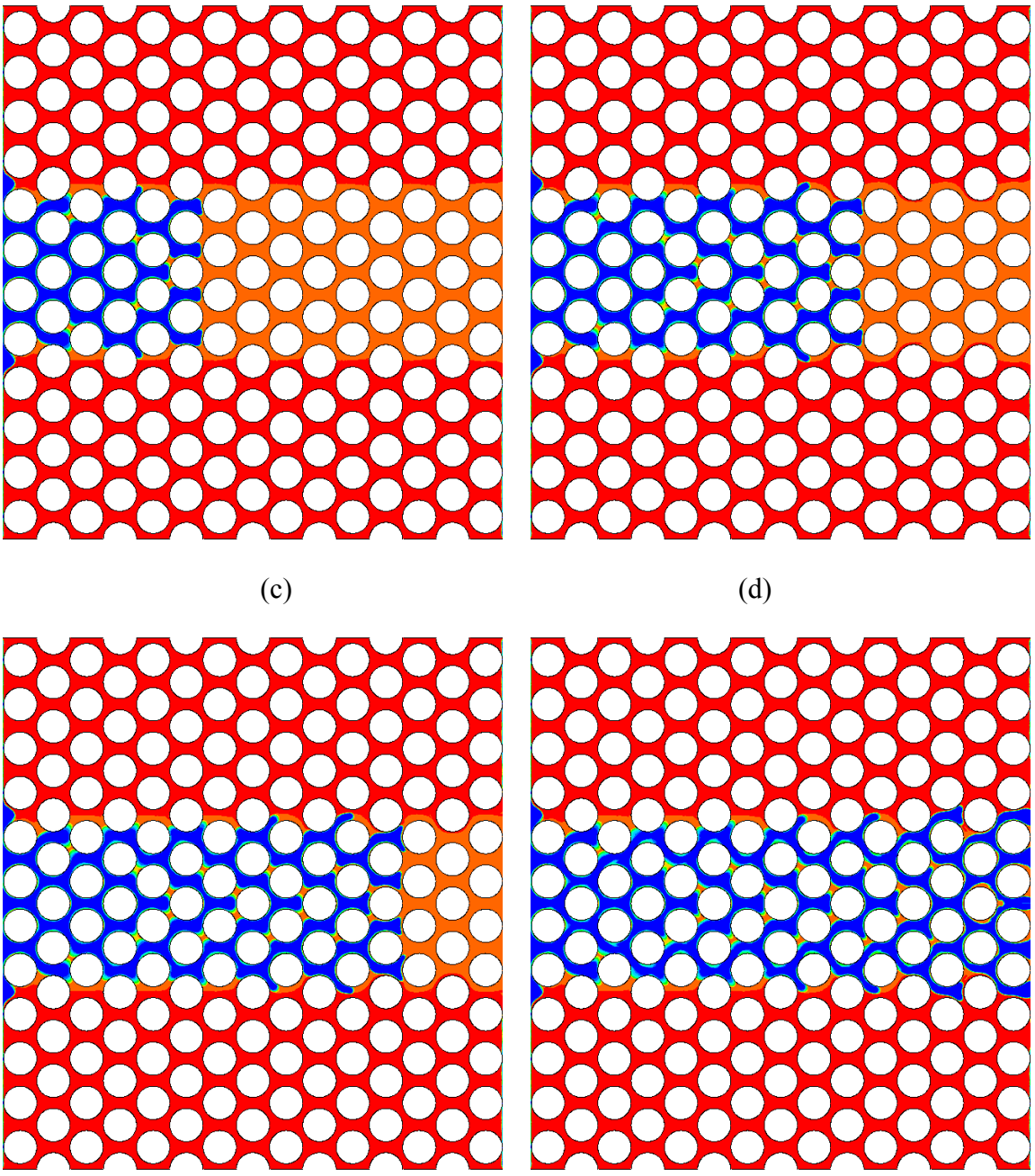

(c) (d)

(e) (f)

Fig. 4.4— Continued.

If the pressure gradient is high enough, the shear stress in the filter cake domain is greater than the initial yield stress. Therefore, both of the original gel and the filter cake are flowing and displaced by the gas, as shown in **Fig. 4.5**. From Fig. 4.5, the filter cake moves slower than the original gel. This is because the filter cake has a larger initial yield stress, and more pressure gradient need to be used to overcome this critical value. In addition, the filter cake has a higher consistency factor. This also leads to a lower velocity for the filter cake. Because of high pressure gradient, the remaining original gel does not block the narrowest part of the pore throat, which happens in the previous case. The remaining original gel exists at the side of the proppants that is far from the inlet. The flow direction is from left to right.

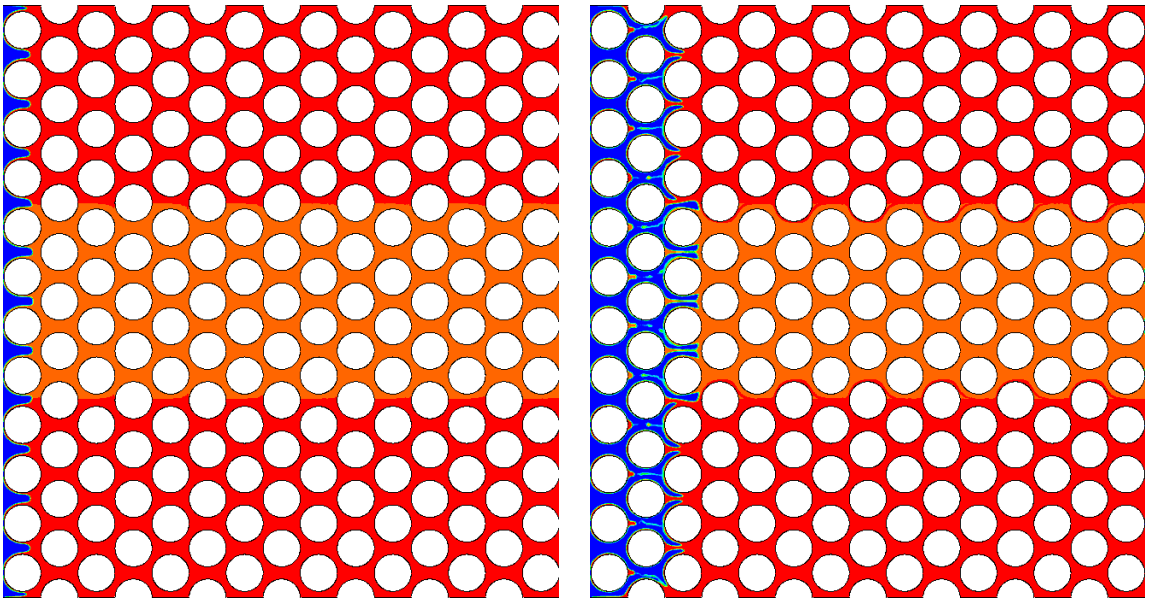

(a) (b)

Fig. 4.5— Displacement of the original gel and the filter cake in porous media (large pressure gradient).

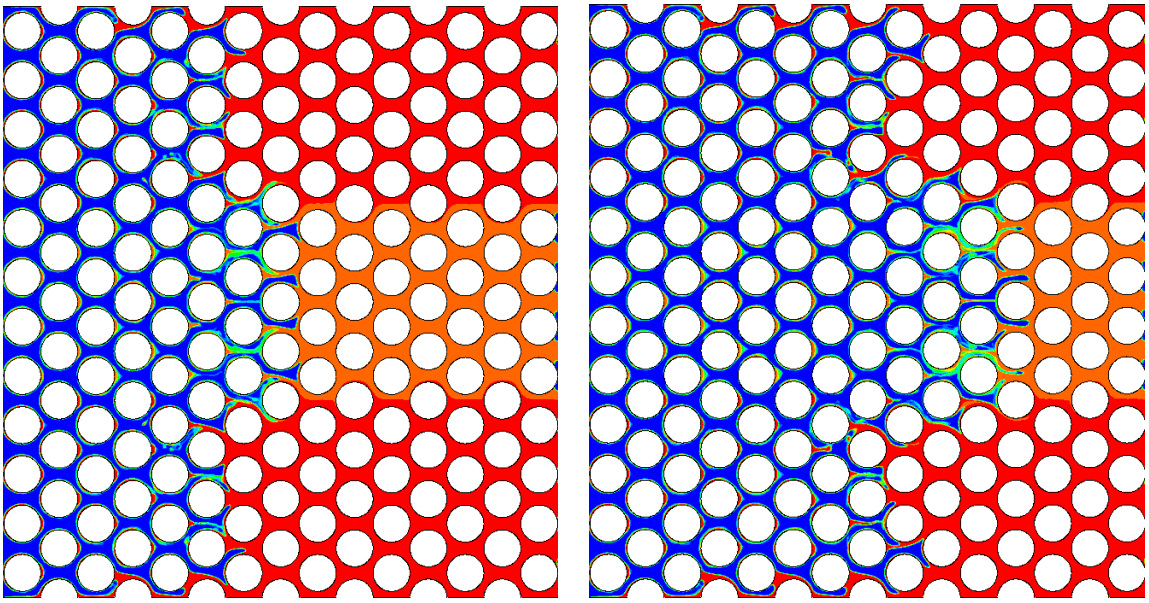

(c) (d)

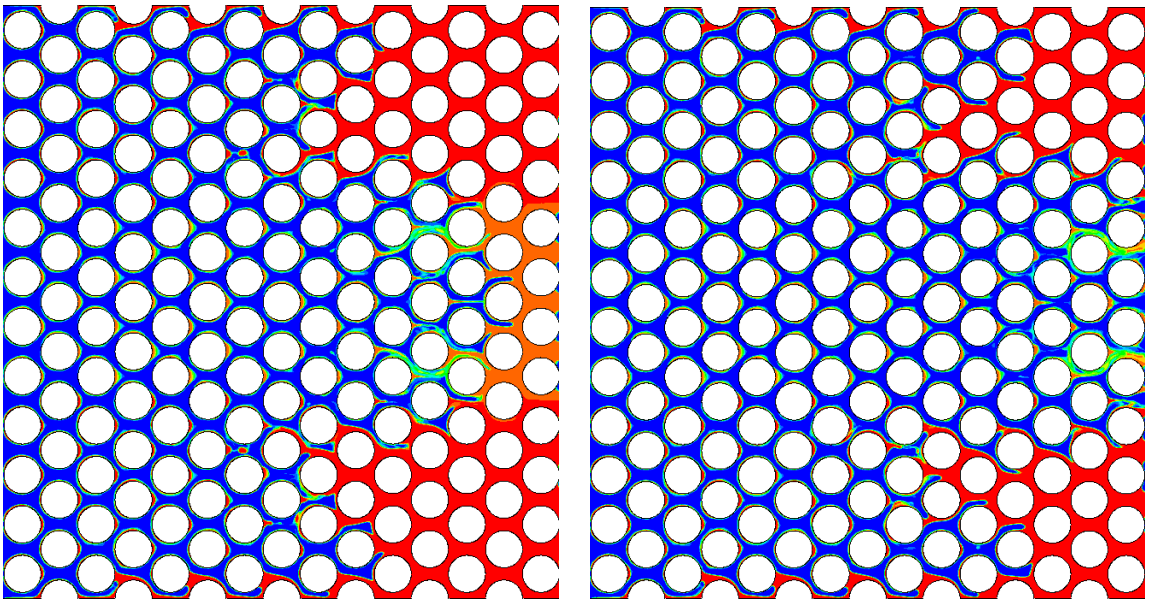

(e) (f)

Fig. 4.5— Continued.

From previous two numerical simulation results, the original gel and the filter cake have independent flow behavior, not matter under high pressure gradient or low pressure gradient. It looks like the gas displace the original gel and the filter cake at different flow zone and two fluids have little impact to each other. There might be two explanations. One reason might be that two fluids have large different on rheological parameter. The other possible reason is that the proppants separate two phases. Because of this analysis, to make the problem simpler, we will only investigate two phase flow in porous media. Non-Newtonian fluid (filter cake or original gel) is displaced by Newtonian fluid (gas) in porous media under different conditions.

4.4 Numerical Simulation of Two Phase Displacement Flow

In this section, we numerically investigated the flow behavior of non-Newtonian fluid displaced by Newtonian fluid in porous media. The micro pore-scale models developed in the Chapter III was used to mimic the porous structure. The Herschel-Bulkley-Papanastasiou model (1987) was also used in the simulation cases to mitigate numerical difficulties.

4.4.1 Boundary Condition & Algorithm

In the numerical simulation, a constant temperature of 290 °K and a constant pressure of 50 psi are assumed for all fluids. The inlet boundary is assumed to have a constant velocity; the outlet boundary is at a constant pressure of zero psi. In FLUENT, all pressure was relative to the reference pressure. Wall boundary condition was adopted

on the surface of the proppants. Symmetry boundary conditions were used at the span-wise and transverse directions to maintain periodicity in the width direction.

We used the method of Least Squares Cell Based to calculate the gradients in discretizing the convection and diffusion terms in Navier-Stokes equations. For pressure-velocity decoupling term, we used Fractional Step scheme. We used second order implicit for transient formulation. The non-iterative time advancement method has been took.

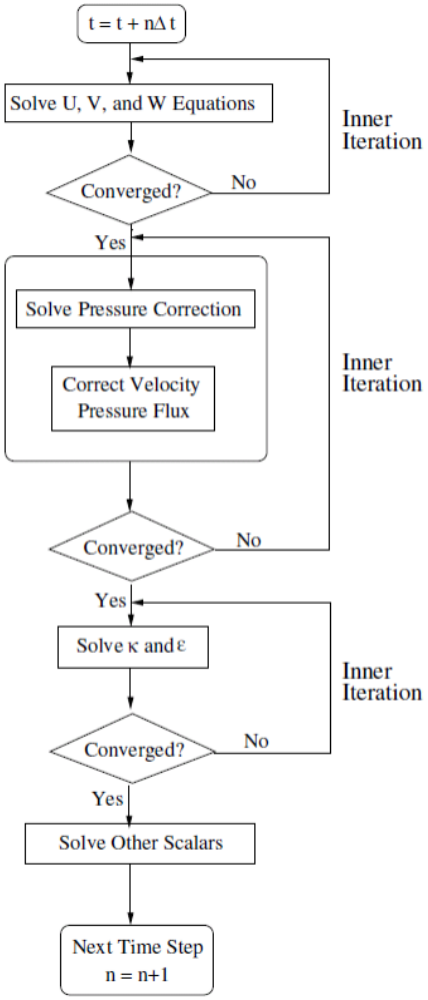

Fig. 4.6—Flow chart of the non-iterative fractional step method (From FLUENT help document "Theory Guide").

We adopted the second-order upwind scheme for the spatial discretization of flow moment governing equations and Modified High Resolution Interface Capturing (HRIC) for volume fraction. More detail about HRIC can refer FLUENT help document "Theory Guide". The maximum Global Courant Number is 0.5 during the entire calculation process. At every time step, the root mean squares of the normalized residual error for all of the equations are smaller than 10^{-5}. The calculations assumed that the flows are three-dimensional, transient, laminar and incompressible.

4.4.2 Flow Field Visualizations

Fig. 4.7 shows the displacement process of Herschel-Bulkley fluid in simple cubic packing arrangement. The figures provide the evolution of the contour of phase and pressure distribution through the entire flow domain. In Fig. 4.7, red color stands for non-Newtonian fluid and blue color stands for Newtonian fluid. The other colors, like green and yellow, mean that there have both of two fluids in the cell. Different colors indicate the different percentages for each phase. We find that most of remaining non-Newtonian fluid leaves far from the main flowing channel and near the obstructed part.

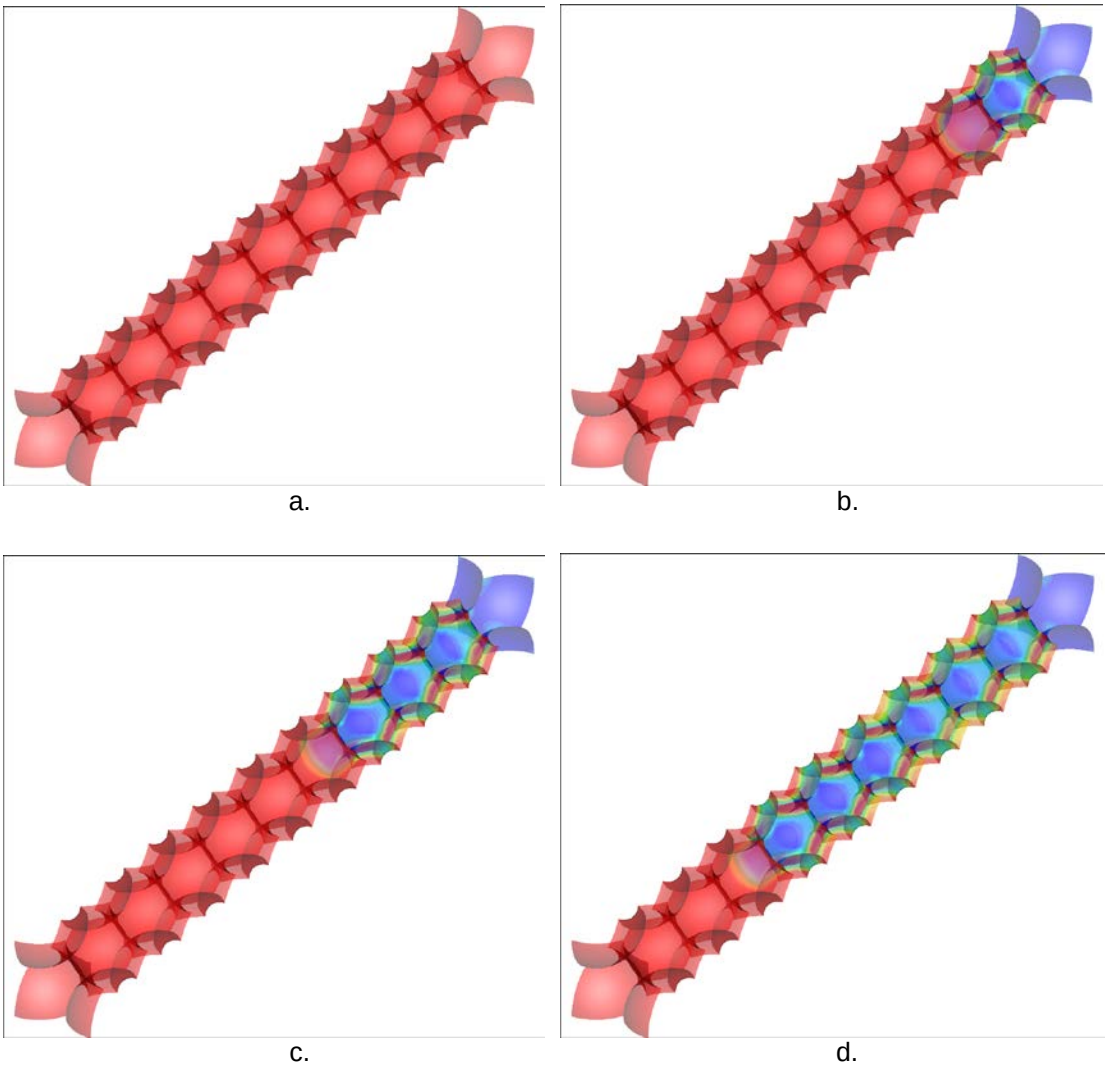

Fig. 4.7—Visualizations of the evolution of the phase distribution on non-Newtonian fluid displacement in media proppant pack of SC.

From the figures of the pressure distribution, **Fig. 4.8**, we can see that the pressure gradient in Newtonian fluid is smaller than in non-Newtonian fluid. In Newtonian fluid zone, the contour of the pressure has uniform color. This is because the non-Newtonian fluid has a much larger viscosity, comparing with Newtonian fluid. When the more non-Newtonian fluid is displaced, the smaller pressure gradient is

required to keep the same flow rate. This also can be proved by the figure of the pressure drop variation with time in the following.

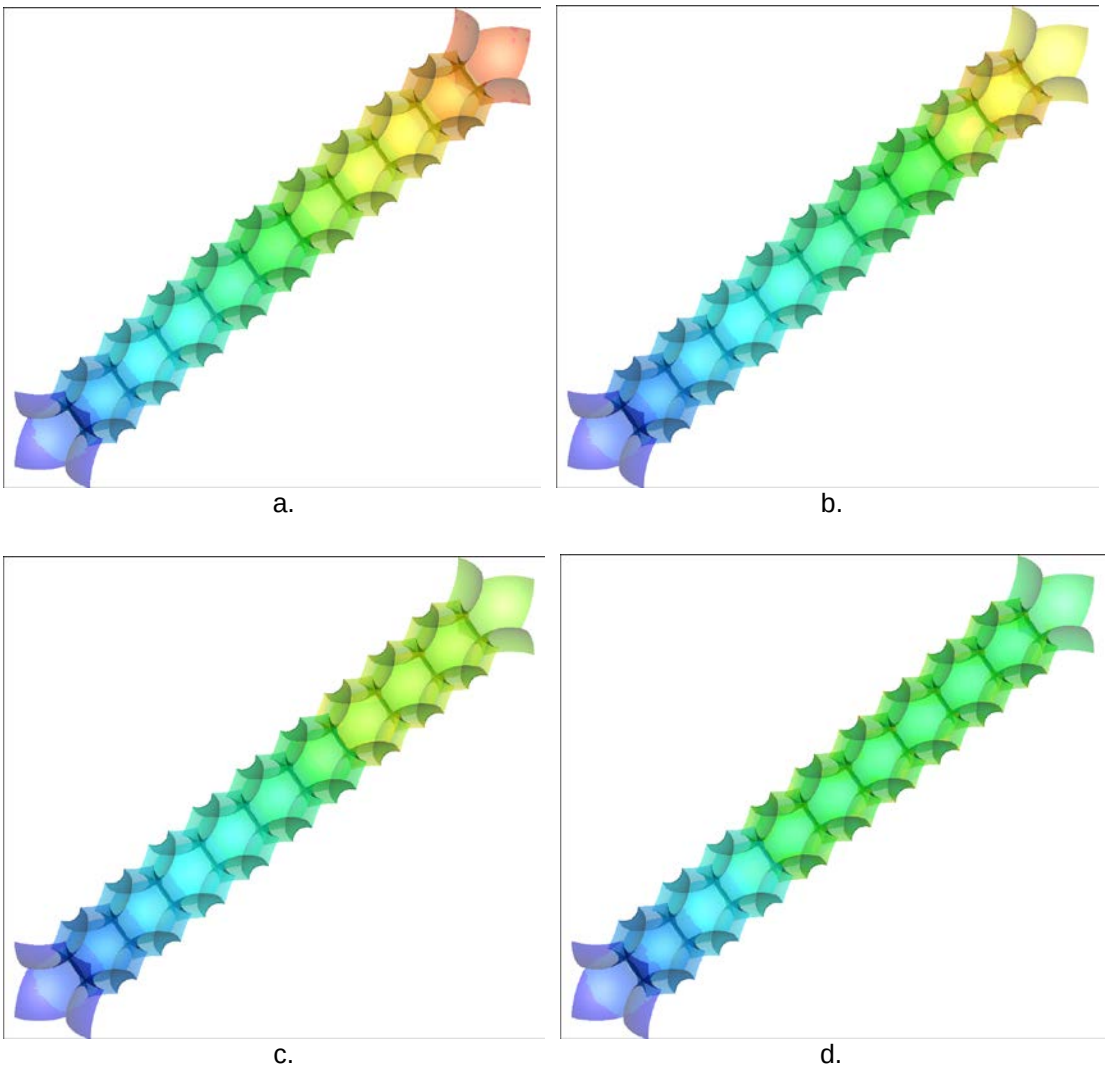

Fig. 4.8—Visualizations of the evolution of the pressure distribution on non-Newtonian fluid displacement in media proppant pack of SC.

To clear observe where the residual non-Newtonian leaves, we provides the phase distribution on cross-section at different position along the proppant packing, as shown in **Fig. 4.9**. Red color stands for non-Newtonian fluid and blue color stands for Newtonian fluid. At the large cross section, like Fig. 4.9a, lots of non-Newtonian fluid remains around the main flowing channel. The residual space is in the narrowest part that between the proppants. Most of Newtonian fluid can flow through the center of the pore throat. At the small cross section, as Fig. 4.9d, most of the pore throat is flowing zone for the Newtonian fluid. Because the small cross section has a little available space for flow, most part of the cross section has been cleaned up and only a little non-Newtonian fluid remains.

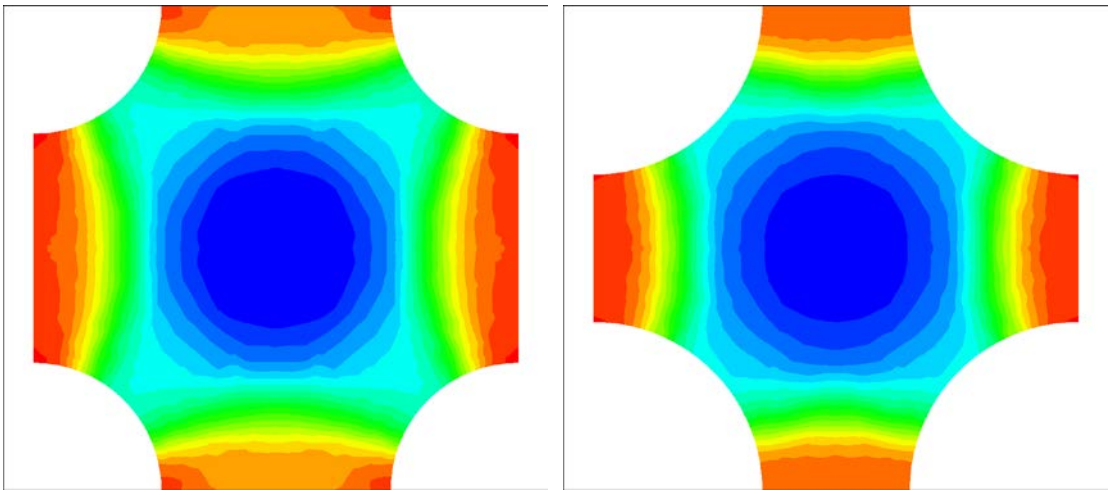

(a) (b)

Fig. 4.9—The contour of the phase distribution on cross-section at different positions.

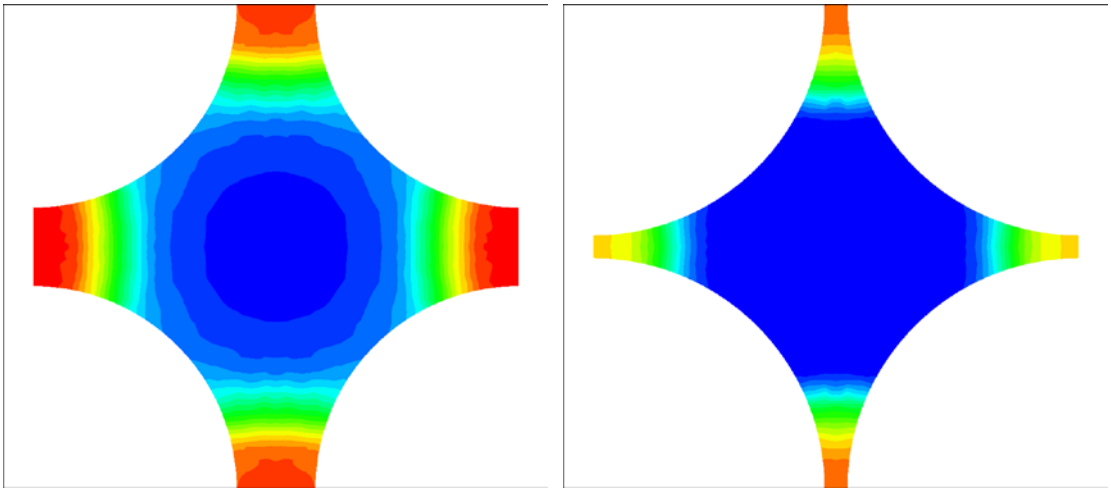

(a) (b)

Fig. 4.9—Continued.

4.4.3 Pressure Gradient, Saturation, & Relative Permeability

Fig. 4.10 shows the evolution of the pressure drop along the flow domain with time. In general, the pressure drop shows a tendency of decreasing with time, but has fluctuations.

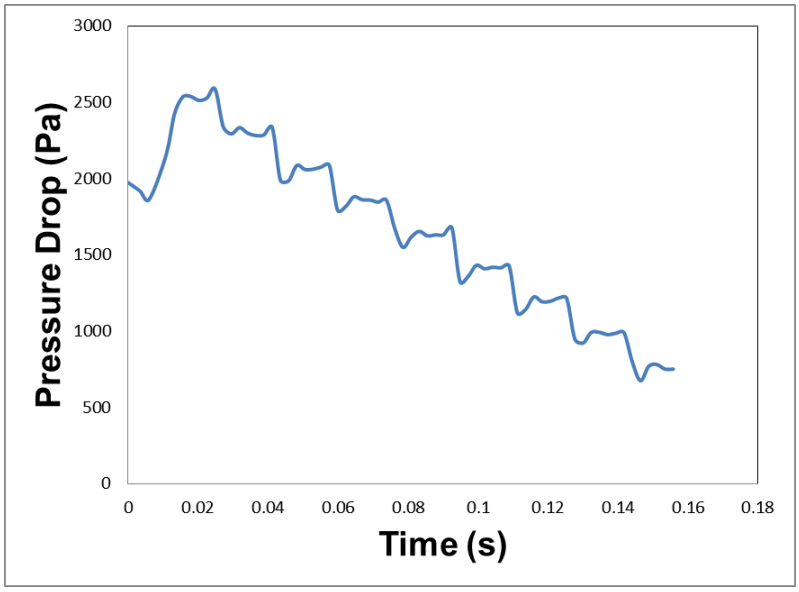

Fig. 4.10—The pressure drop variation with time.

Fig. 4.11 shows the evolution of the non-Newtonian fluid saturation in porous media with time. The saturation linearly decreases with time, because the gas inlet velocity is constant in the case. In this case, the water don't breakthrough, because the computation don't finish.

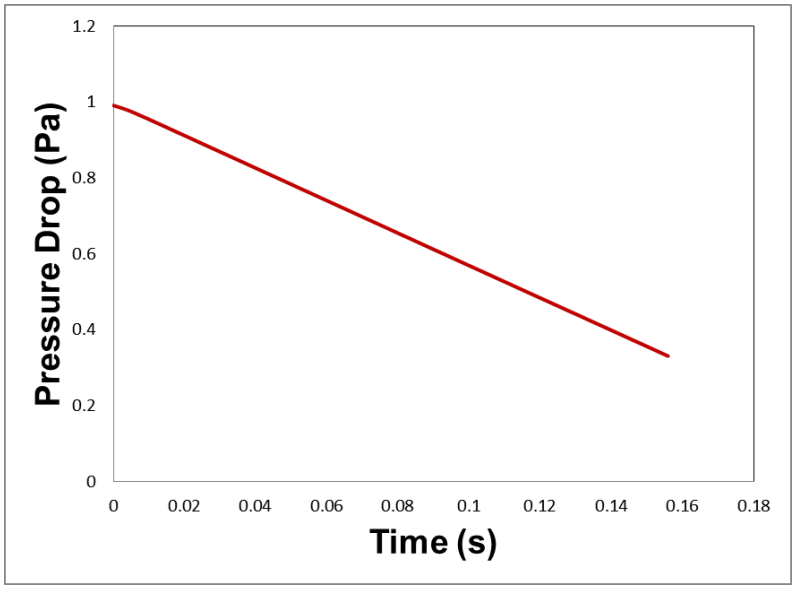

Fig. 4.11—The saturation of non-Newtonian fluid variation with time.

CHAPTER V

CONCLUSIONS AND RECOMMENDATIONS

5.1 Conclusions

Beginning with shear stress distribution and rheological equation for Herschel-Bulkley fluid, I have modeled the filter cake cleanup between two parallel conductivity cores and find that there exist three possible existing flow patterns. I set up and ran a serial of filter cake cleanup experiments to compare with mathematical model. The major purpose of this part of the research work is to examine the effect of initial yield stress on the filter cake cleanup.

At the second part of the work, we used the micro pore structure as the flow channel to numerically simulate non-Newtonian fluid flow in porous media. The numerical simulation captures the characteristics of non-Newtonian fluid flow phenomenon in channels in porous media that the experiments fail to see. We sensitivity investigated the porous-media flow behavior of Herschel-Bulkley fluids. The correlation between pressure gradient and velocity was studied by varying key parameters, such as rheological parameters, proppant packing arrangement way and proppant diameter. We also developed the mathematical model for non-Newtonian fluid flow in porous media. The correlation between capillary tube flow and porous media flow act as the criteria to determine the analytical solutions. But we recognized a popular misuse of the Kozeny equation in the derivation of flow equations for non-Newtonian fluids in capillary bundles model. Using numerical simulation results, we established the new effective radius equations, which consider the effect of rheological parameter and pressure drop.

By these effective radius equations, we successfully developed mathematical models for non-Newtonian fluids flow in porous media.

At the last part of our research, we numerically and theoretically studied the two-phase displacement flow in porous media. Non-Newtonian fluid (filter cake/original gel) is displaced by Newtonian fluid (production gas) through a proppant pack. We used the VOF model in FLUENT to simulate flow behavior of multi immiscible fluids. Based on the numerical results of unsteady-state displacement test data on a small porous media, JBN method was used to calculate the relative permeability.

Based on the comparisons and discussions above, this study reveals the following important conclusions:

1. Both of mathematical model and experiment results show that initial yield stress plays an important influence on the filter cake cleanup on fracture surfaces. The initial yield stress of non-Newtonian fluids leads to a large Flow Initiation Gradient (FIG) and make the filter cake difficulty to be cleaned up.
2. The Kozeny-Carman correlation is not appropriate for non-Newtonian fluid flow in porous media. The correlation between capillary flow and porous-media flow cannot be solved analytical. From the numerical simulation results, the fitting functions for the effective radius have been developed. The effective radius equation for a power law fluid includes the parameter of power law index. The effective radius equation for a Bingham fluid depends

on the ratio of the yield stress to the pressure drop. For a Herschel-Bulkley fluid, the function considers both parameters.

3. At the region of high velocity, for the same velocity, increasing of the power law index causes acute increasing of the pressure gradient. However, at the region of low velocity, fluid with smaller power law index needs higher pressure gradient.
4. Fluid with yield stress can flow only if the pressure gradient exceeds a value. This initiation pressure gradient linearly increases with the yield stress. But the initiation pressure gradient has an inverse linear relationship with the proppant diameter.
5. Because the viscosity of non-Newtonian fluid strongly depends on pore structure, the proppant packing arrangement is an important factor for non-Newtonian fluid flow behavior in porous media.

5.2 Recommendations

During this research, some problems still necessitate further be studied. I investigated the major effects on non-Newtonian fluid flow in porous media, like the cleanup of the filter cake on fracture wall and the residual gel between the proppants. But several aspects that I neglected may require more consideration and the results of our research should be applied in practice. In addition, a few recommendations will be list as follows:

1. I considered the most classic method of proppant packing arrangement: simple cubic, body center cubic, and face center cubic. From our results, the proppant packing arrangement way is an important factor that influents the pressure gradient. But usually the proppant packing in fracture is chaotic, but might have some regular patterns in the statistical sense. It is recommended to run some cases for randomly proppant packing or find the regular pattern. Simulation for randomly packing will require more computational capability. And it is also a challenge to CFD pre-processing, solver and post-processing software. Finding out the regular patterns in the statistical sense is another tropic in porous-media flow, but it is very meaningful. The packing arrangement should depend on the shape of the proppant, the closed pressure, the geometry of the fracture, and so on. This tropic will be another challenging issue in the future.
2. In our work, to consider the situation of the proppant having different diameter in a packing arrangement, the ratio of diameter of large proppant to small proppant is set to two. It will be more realistic if the proppant diameter in our geometry model has a characteristic distribution within a reasonable range. The characteristic distribution should come from statistical result for actual proppants product. This usually can be found on the manual from the proppant supplier.

3. The mathematical model of the filter cake and residual gel cleanup should be incorporated in any reservoir simulator to investigate the effect of gel damage on gas production. From the mathematical model in Chapter III, we have the apparent viscosity of non-Newtonian fluid for single phase flow in propped fracture. From the mathematical model in Chapter IV, we have the relative permeability of two-phase displacement in propped fracture. All models should be easily applied on the grids that stand for the propped fracture by adding a user defining function. The function can calculate the apparent viscosity or the relative permeability at every time step, based on the information on each grid, like pressure gradient, porosity and so on. If possible, we should run reservoir simulation case based on the real field condition, and then compare the results with filed production data.
4. Some reservoir problem, such as heavy oil recovery, polymer flooding, etc., belong to the class of porous-media displacement flow of non-Newtonian fluid. If heavy oil or polymer has a remarkable characteristic of non-Newtonian fluid, traditional equation of non-Newtonian fluid flow in porous media is not suitable in reservoir simulator. The modification for adding our model in reservoir flow is also not a hard work. We only need to make some change on fluid or rock property based on the information on reservoir cell.

REFERENCES

Al-Fariss, T., Pinder, K.L. 1987. Flow through porous media of a shear-thinning liquid with yield stress. *Canadian Journal of Chemical Engineering*. Volume 65, Issue 3, Pages 391-405.

ANSYS FLUENT User's Guide, Release 13.0. ANSYS Inc, Canonsburg, Pennsylvania 2010.

ANSYS GAMBIT User's Guide, Release 2.3. ANSYS Inc, Canonsburg, Pennsylvania 2006.

Apiano, F.M., Hansjoerg S., Hans J.H. and Jose S.A.J. 2009. Non-Newtonian Fluid Flow through Three-Dimensional Disordered Porous Media. *Physical Review Letters.* Volume 103, Issue 19.

Ayoub, J.A., Hutchins, R.D., Bas, F.V.D. 2006a. New Findings in Fracture Clean-up Change Common Industry Perceptions. Paper presented at the International Symposium and Exhibition on Formation Damage Control, Lafayette, Louisiana U.S.A. SPE 98746-MS.

Ayoub, J.A., Hutchins, R.D., Bas, F.V.D. 2006b. New Results Improve Fracture Cleanup Characterization and Damage Mitigation. Paper presented at the SPE Annual Technical Conference and Exhibition, San Antonio, Texas, USA. SPE 102326-MS.

Balhoff, M.T. and Miller, M.J. 2005. An Analytical Model for Cleanup of Yield-Stress Fluids in Hydraulic Fractures. *SPE Journal*. Volume 10, Issue 1, Pages 5-12.

Balhoff. M., Thompson K. E. 2004. Modeling Polymer Displacement in Hydraulic Fractures at the Pore-Scale. Paper presented at the SPE Annual Technical Conference and Exhibition, Houston, Texas, USA. SPE 90197 .

Balhoff. M., Thompson K. E. 2006. A Macroscopic Model for Shear-thinning Flow in Packed Beds based on Network Modeling. *Chemical Engineering Science*. Volume 61, Issue 2, Pages 698-719.

Belblidia, F., Tamaddon-Jahromi, H.R., Webster, M.F., and Walters, K. 2010. Computations with Viscoplastic and Viscoelastoplastic Fluids. *Rheologica Acta*. Volume 50, Issue 4, Page 343-360.

Bird, R.B., Stewart, W.E., Lightfoot, E.N. 1960. *Transport Phenomena*. First Edition. Wiley, New York.

Brackbill, J.U., Kothe, D.B., Zemach, C. 1992. A Continuum Method for Modeling Surface Tension. *Journal of Computational Physics*. Volume 100, Issue 2, Pages 335-354.

Chase, G.G., Dachavijit P. 2003. Incompressible Cake Filtration of a Yield Stress Fluid. *Separation Science and Technology*. Volume 38, Issue 4, Pages 745-766.

Christopher, R.H., Middleman, S. 1965. Power-Law Flow Through a Packed Tube. *Industrial & Engineering Chemistry Fundamentals*. Volume 4, Issue 4, Pages 422-426.

Choi, H. S., Park, H. C., Huh, C., and Kang, S. 2011. Numerical Simulation of Fluid Flow and Heat Transfer of Supercritical CO2 in Micro-porous Media. *Energy Procedia*.Volume 4, Pages 3786-3793.

Economides M.J., Nolte K.G. 2000. *Reservoir Stimulation*. Third edition. Wiley, New York.

El-Khatib, N. 2005. Immiscible Displacement of Non-Newtonian Fluids in Stratified Reservoirs. Paper presented at the SPE Middle East Oil & Gas Show and Conference, Bahrain. SPE 93394.

Ergun, S. Fluid flow through packed columns. 1952. *Chemical Engineering Progress*. Volume 48, Issue 2, Pages 89–94.

Friedel, T. 2006. Numerical Investigation on Hydraulic Fracture Cleanup and Its Impact on the Productivity of a Gas Well with a Non-Newtonian Fluid Model. Paper presented at the SPE Gas Technology Symposium, Calgary, Alberta, Canada. SPE 99445.

May, E.A., Britt, L.K., and Nolte, K.G. 1997. The Effect of Yield Stress on Fracture Fluid Cleanup Nolte, Spe, Dowell. Paper presented at the SPE Annual Technical Conference and Exhibition, San Antonio, Texas, USA. SPE 38619.

Mitsoulis, E., Galazoulas, S. 2009. Simulation of Viscoplastic Flow Past Cylinders in Tubes. *Journal of Non-Newtonian Fluid Mechanics*. Volume 158, Issue 1-3, Pages 132-141.

Nguyen, V. H., Remond, S., Gallias, J. L., Bigas, J.P. and Muller, P. 2006. Flow of Herschel-Bulkley Fluids through the Marsh Cone. *Journal of Non-Newtonian Fluid Mechanics*. Volume 139, Issue 1-2, Pages 128-134.

Nijemeisland, M., Dixon, A.G. 2004. CFD Study of Fluid Flow and Wall Heat Transfer in a Fixed Bed of Spheres. *AICHE Journal*. Volume 50, Issue 5, Pages 906-921.

Ouyang, L., Yango, T., Zhu, D. and Hill, A.D. 2011. Theoretical and Experimental Modeling of Residual Gel Filter Cake Displacement in Propped Fractures. *SPE Productoin & Operations.* Volume 27, Issue 4, Pages 363-370.

Ouyang, L., Zhu, D. and Hill, A.D. 2013. Theoretical and Numerical Simulation of Herschel-Bulkley Fluid Flow in Propped Fractures. Paper presented at the 6th International Petroleum Technology Conference, Beijing, China. IPTC 17011.

Palisch, T., Duenckel, R., and Bazan, L. 2007. Determining Realistic Fracture Conductivity and Understanding Its Impact on Well Performance – Theory and Field Examples. Paper presented at the SPE Hydraulic Fracturing Technology Conference, College Station, Texas, USA. SPE 106301.

Papanastasiou, T.C. 1987. Flows of Materials with Yield. *Journal of Rheology*. Volume 31, Issue 5, Pages 385-404.

Park, H.C. 1972. The Flow of Non-Newtonian Fluids through Porous Media. Ph.D. dissertation, Michigan State University, East Lansing, Michigan.

Samuelson, M.L. and Constien, V.G. 1996. Effects of High Temperature on Polymer Degradation and Cleanup. Paper presented at the SPE Annual Technical Conference and Exhibition, Denver, Colorado, USA. SPE 36495.

Sochi, T. 2010. Computational Techniques for Modeling Non-Newtonian Flow in Porous Media. *International Journal of Modeling, Simulation, and Scientific Computing*. Volume 1, Issue 2, Pages 239-256.

Sochi, T. 2010. Flow of Non-Newtonian Fluids in Porous. *Journal of Polymer Science Part B-Polymer Physics*. Volume 48, Issue 23, Pages 2437-2467.

Teeuw D., Hesselink F.T. and Koninklijke 1980. Power-Law Flow and Hydrodynamic Behaviour of Biopolymer Solutions in Porous Media. Paper presented at the SPE Oilfield and Geothermal Chemistry Symposium, Stanford, California, USA. SPE 8982.

Voneiff, G.W., Robinson, B.M., and Holditch, S.A. 1996. The Effects of Unbroken Fracture Fluid on Gas Well Performance. *SPE Production & Operations.* Volume 11, Issue 4, Pages 223-229.

Vradis, G.C., Protopapas, A.L. 1993. Macroscopic Conductivities for Flow of Bingham Plastics in Porous Media. *ASCE Journal of Hydraulics Engineering*. Volume 119, Issue 1, Pages 95-108.

Wang, S., Huang, Y., and Civan, F. 2006. Experimental and Theoretical Investigation of the Zaoyuan Field Heavy Oil Flow through Porous Media. *Journal of Petroleum Science & Engineering*. Volume 50, Issue 2, Pages 83-101.

Wang, Y. 2008. Simulation of Fracture Fluid Cleanup and Its Effect on Long-Term Recovery in Tight Gas Reservoirs. Ph.D. dissertation, Texas A&M University, College Station, Texas.

Wang, Y., Holditch, S.A., and Mcvay, D.A. 2008. Simulation of Gel Damage on Fracture-Fluid Cleanup and Long-Term Recovery in Tight-Gas Reservoirs. Paper presented at the SPE Eastern Regional/AAPG Eastern Section Joint Meeting, Pittsburgh, Pennsylvania, USA. SPE 117444-MS.

Xu, B., Wang, L., Hill, A.D., Zhu, D. 2011. Experimental Evaluation of Guar Fracture Fluid Filter Cake Behavior. *SPE Productoin & Operations.* Volume 26, Issue 4, Pages 381-387.

Yango, Takwe. 2011. Characterize Filter Cake Buildup under Dynamic Fluid Loss Conditions. Master thesis, Texas A&M University, College Station, Texas.

Yi, X. 2004. Model for Displacement of Herschel-Bulkley Non-Newtonian Fluid by Newtonian Fluid in Porous Media and Its Application in Fracturing Fluid Cleanup. Paper presented at the SPE International Symposium and Exhibition on Formation Damage Control, Lafayette, Louisiana, USA. SPE 86491-MS.

APPENDIX A

VELOCITY FOR THE FILTER CAKE

The velocity expression for yielded filter cake is:

$$v_{HB,yield}(r) = -\frac{(Ar-B)^{1+\frac{1}{n}}}{A\left(1+\frac{1}{n}\right)} + c_2 \tag{A.1}$$

Assuming that the filter cake does not slip on the surface of the cell, we can get the constant c_2.

$$c_2 = \frac{(AR-B)^{1+\frac{1}{n}}}{A\left(1+\frac{1}{n}\right)} \tag{A.2}$$

Using velocity continuity condition, the constant velocity for slug-like filter cake is given.

$$v_{HB,unyield}(r) = c_1 = \frac{(AR-B)^{1+\frac{1}{n}}}{A\left(1+\frac{1}{n}\right)} \tag{A.3}$$

The average velocity of the filter cake can be obtained by integrating the velocity profile through all filter cake region

$$\overline{u}_{HB} = \frac{\int_{R_G}^{R} v dr}{\int_{R_G}^{R} r dr} = \frac{\int_{R_G}^{R_{YS}} v_{HB,unyield}\, dr + \int_{R_{YS}}^{R} v_{HB,yield}\, dr}{R - R_G} \tag{A.4}$$

Here

$$\int_{R_G}^{R_{YS}} v_{HB,unyield}\,dr = \frac{(AR-B)^{1+\frac{1}{n}}}{A\left(1+\frac{1}{n}\right)}(R-R_{YS}) - \frac{(AR-B)^{2+\frac{1}{n}}}{A^2\left(1+\frac{1}{n}\right)\left(2+\frac{1}{n}\right)} \tag{A.5}$$

$$\int_{R_G}^{R_{YS}} v_{HB,yield}\,dr = \frac{(AR-B)^{1+\frac{1}{n}}}{A\left(1+\frac{1}{n}\right)}(R_{YS}-R_G) \tag{A.6}$$

So average velocity of a Herschel-Bulkley fluid flowing through a slot, including yielded and unyielded part, is shown below:

$$\overline{u}_{HB} = \frac{\int_{R_G}^{R} v dr}{\int_{R_G}^{R} r dr} = \frac{(AR-B)^{1+\frac{1}{n}}}{A\left(1+\frac{1}{n}\right)} - \frac{(AR-B)^{2+\frac{1}{n}}}{A^2\left(1+\frac{1}{n}\right)\left(2+\frac{1}{n}\right)(R-R_G)} \tag{A.7}$$

APPENDIX B

VELOCITY FOR THE HERSCHEL-BULKLEY FLUID IN TUBE

The constant velocity expression for slug-like Herschel-Bulkley fluid is:

$$u_{HB,unyield} = \frac{(AR - B)^{1+1/n}}{A(1+1/n)} \tag{B.1}$$

Here, R is the radius of the tube. This unyielded part of non-Newtonian exists in the region $0 < r < R_{YS}$. The expression for volumetric flow rate for this part is given.

$$Q_{HB,unyield} = \int_0^{R_{YS}} v_{HB,unyield}\, dr = \frac{(AR - B)^{1+1/n}}{A(1+1/n)} \pi R_{YS}^2 \tag{B.2}$$

For the yielded zone $R_{YS} < r < R$, the volumetric flow rate can be obtained by integrating the velocity profile.

$$\begin{aligned} Q_{HB,yield} &= \int_{R_{YS}}^{R} v_{HB,unyield}\, 2\pi r dr \\ &= 2\pi \int_{R_{YS}}^{R} -\frac{(Ar - B)^{1+1/n}}{A(1+1/n)} r dr + 2\pi \int_{R_{YS}}^{R} \frac{(AR - B)^{1+1/n}}{A(1+1/n)} r dr \end{aligned} \tag{B.3}$$

Here

$$2\pi\int_{R_{YS}}^{R}-\frac{(Ar-B)^{1+1/n}}{A(1+1/n)}rdr=\frac{-2\pi}{A^2(1+1/n)}\int_{R_{YS}}^{R}(Ar-B)^{1+1/n}rd(Ar-B)$$
$$=\frac{-2\pi}{A^2(1+1/n)}\left[r\frac{(Ar-B)^{2+1/n}}{2+1/n}\Bigg|_{R_{YS}}^{R}-\frac{1}{A(2+1/n)}\int_{R_{YS}}^{R}(Ar-B)^{2+1/n}d(Ar-B)\right]$$
$$=\frac{-2\pi}{A^2(1+1/n)}\left[R\frac{(AR-B)^{2+1/n}}{2+1/n}-\frac{1}{A(2+1/n)}\frac{(Ar-B)^{3+1/n}}{3+1/n}\Bigg|_{R_{YS}}^{R}\right]$$
$$=\frac{-2\pi R(AR-B)^{2+1/n}}{A^2(1+1/n)(2+1/n)}+\frac{2\pi(AR-B)^{3+1/n}}{A^3(1+1/n)(2+1/n)(3+1/n)}$$

, (B.4)

$$2\pi\int_{R_{YS}}^{R}\frac{(AR-B)^{1+1/n}}{A(1+1/n)}rdr=\frac{(AR-B)^{1+1/n}}{A(1+1/n)}\pi(R^2-R_{YS}^2) \quad \text{(B.5)}$$

So the average velocity of a Herschel-Bulkley fluid flowing through a capillary tube, including the yielded and unyielded parts, is:

$$\bar{u}_{HB}=\frac{\int_0^R v2\pi rdr}{\int_0^R 2\pi rdr}=\frac{1}{\pi R^2}\left(Q_{HB,yield}+Q_{HB,unyield}\right)$$
$$=\frac{1}{\pi R^2}\left(\begin{array}{l}\dfrac{(AR-B)^{1+1/n}}{A(1+1/n)}\pi R_{YS}^2-\dfrac{2\pi R(AR-B)^{2+1/n}}{A^2(1+1/n)(2+1/n)}\\+\dfrac{2\pi(AR-B)^{3+1/n}}{A^3(1+1/n)(2+1/n)(3+1/n)}+\dfrac{(AR-B)^{1+1/n}}{A(1+1/n)}\pi(R^2-R_{YS}^2)\end{array}\right)$$
$$=\frac{1}{\pi R^2}\left(\frac{(AR-B)^{1+1/n}}{A(1+1/n)}\pi R^2-\frac{2\pi R(AR-B)^{2+1/n}}{A^2(1+1/n)(2+1/n)}+\frac{2\pi(AR-B)^{3+1/n}}{A^3(1+1/n)(2+1/n)(3+1/n)}\right)$$
$$=\frac{(AR-B)^{1+1/n}}{A(1+1/n)}-\frac{2(AR-B)^{2+1/n}}{A^2R(1+1/n)(2+1/n)}+\frac{2(AR-B)^{3+1/n}}{A^3R^2(1+1/n)(2+1/n)(3+1/n)}$$

(B.6)

APPENDIX C

VALIDATION OF FINITE VOLUME SIMULATOR

ANSYS Fluent is one of the most popular commercial computational fluid dynamics packages for modeling fluid flow and other physical phenomena. It provides fast and accurate CFD result, flexible meshes, and powerful parallel capacity. In FLUENT, User Defined Functions allow the implementation of user models for special purpose. Therefore, FLUENT is a suitable software package for our complicated physical problem.

The finite volume method is used to solve the Navier-Stokes equations for fluid flow problems in FLUENT. In finite volume method, the computational domain is divided into lots of small computational cells. For each cell, the volume integrals of the flux and diffusion divergence in a partial differential equation are converted to surface integrals by the Gauss-divergence theorem. Two major advantage of the finite volume method are the method is conservative and easily formulated for unstructured meshes.

The general conservation equations governing the flow fluids are shown as the following.

Continuity equation

$$\frac{\partial u}{\partial x}+\frac{\partial v}{\partial y}+\frac{\partial w}{\partial z}=0 \qquad \text{(D.1)}$$

Momentum equations

$$\rho\left(u\frac{\partial u}{\partial x}+v\frac{\partial u}{\partial y}+w\frac{\partial u}{\partial z}\right)=\frac{\partial P}{\partial x}+\mu\left(\frac{\partial^2 u}{\partial x^2}+\frac{\partial^2 u}{\partial y^2}+\frac{\partial^2 u}{\partial z^2}\right) \qquad \text{(D.2a)}$$

$$\rho\left(u\frac{\partial v}{\partial x}+v\frac{\partial v}{\partial y}+w\frac{\partial v}{\partial z}\right)=\frac{\partial P}{\partial y}+\mu\left(\frac{\partial^2 v}{\partial x^2}+\frac{\partial^2 v}{\partial y^2}+\frac{\partial^2 v}{\partial z^2}\right) \quad \text{(D.2b)}$$

$$\rho\left(u\frac{\partial w}{\partial x}+v\frac{\partial w}{\partial y}+w\frac{\partial w}{\partial z}\right)=\frac{\partial P}{\partial z}+\mu\left(\frac{\partial^2 w}{\partial x^2}+\frac{\partial^2 w}{\partial y^2}+\frac{\partial^2 w}{\partial z^2}\right) \quad \text{(D.2c)}$$

To validate our numerical methodology, we studied the laminar flow of Power Law, Bingham and Herschel-Bulkley fluids in a cylindrical tube. We compared CFD predictions of the velocity field with the exact analytical solutions. In the validation cases, the straight cylindrical tube has 5 mm long and 1 mm diameter. To attain the accuracy of the velocity profile, we refine the mesh near the walls. Constant velocity boundary condition was set up at the capillary tube entrance; constant pressure boundary condition was maintained at the capillary tube exit. The velocity profiles obtained at the outlet are compared to the generally analytical expressions. **Fig. D.1-3** presents the comparison between the theoretical and numerical velocity profiles for three fluid models respectively. The line stands for the theoretical solution and the mark stands for the numerical simulation results. The numerical velocity fields accurately match the fully developed theoretical profile.

Fig. D.1 compares the velocity profiles of a Newtonian fluid, a shear-thinning fluid of 0.5 power law index and a shear-thickening fluid of 1.4 power law index. Compared with a parabolic velocity profile of Newtonian fluid, for the power law fluids, the decrease of the power law index flattens the velocity profile and reduces the maximum velocity; the increase of power law index has the opposite effect. The velocity

gradient at the center is zero. Fig. D.1 shows that the CFD prediction of velocity profile was particularly accurate for the power law fluids.

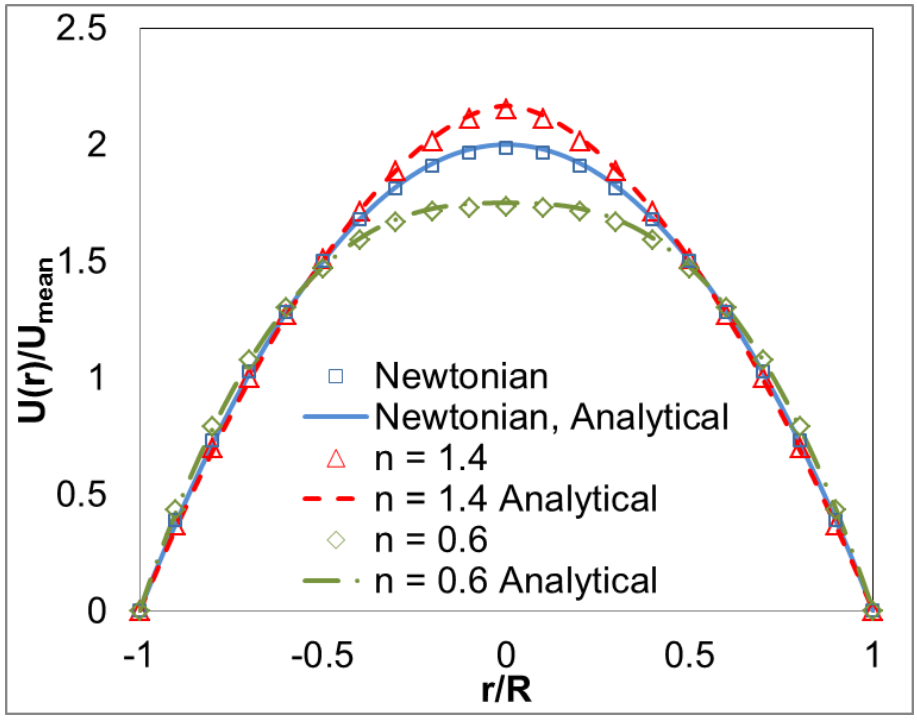

Fig. D.1—Comparison of CFD-predicted and theoretical velocity profiles for Power-Law fluids flow in capillary tube.

For Bingham fluid, we have compared the dimensionless velocity profiles for three yield stresses: 0.1 Pa, 1 Pa and 2 Pa, as given in Fig. D.2. Compared with a parabolic velocity profile of Newtonian fluid, for the Bingham fluids, an increase in the yield stress leads to an increase in the plug-like flow region and also a reduction of the maximum velocity. This means that the increasing yield stress leads to the increasing

pressure gradient for the same flow rate. Fig. D.2 shows that the CFD predictions of velocity profile were almost the same as analytical solutions for the Bingham fluids.

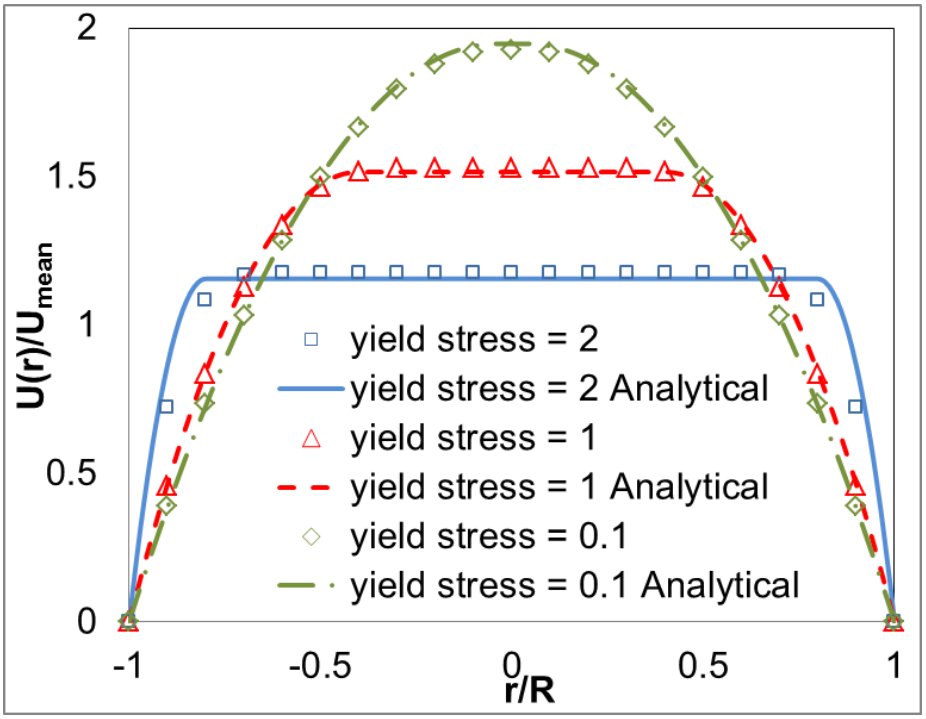

Fig. D.2—Comparison of CFD-predicted and theoretical velocity profiles for Bingham fluids flow in capillary tube.

Fig. D.3 compares the numerical simulated velocity profiles of Herschel-Bulkely fluid with the analytical solutions. For the fluids with a yield stress, Bingham and Herschel-Bulkley fluids, CFD seems to underestimate the unyielded zone slightly, but the agreement is still very good. For theoretical velocity solution, the velocity gradient is discontinuous at the juncture of the yielded and the unyielded zones. In numerical simulation, this discontinuity leads to numerical instability and divergence. The

Papanastasiou model was used to avoid this problem and might be one of the causes of the slight disagreement.

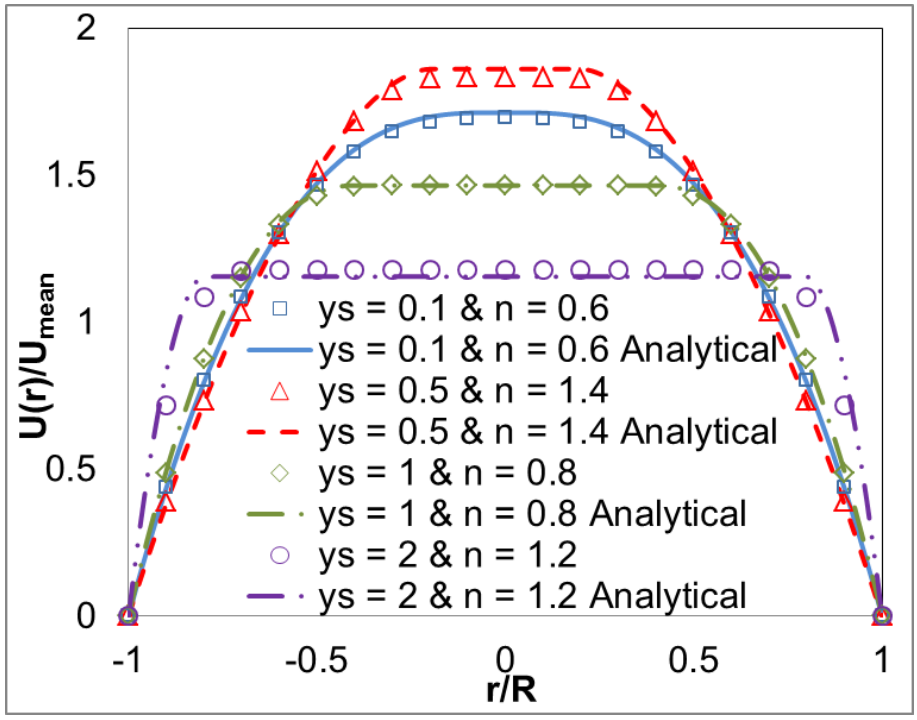

Fig. D.3—Comparison of CFD-predicted and theoretical velocity profiles for Herschel-Bulkley fluids flow in capillary tube.

Note that we give a constant velocity boundary condition at the entrance in the CFD cases and there is the same volumetric flow rate for the theoretical solution and the numerical result. For the pressure gradient between analytical and numerical result, the percentage errors are generally within 1% for all power law fluids and within 3% for fluids involving yield stress. The larger error for Bingham or Herschel-Bulkley model is probable due to the Papanastasiou model and mesh sensitiveness.

APPENDIX D

USER DEFINED FUNCTION

ANSYS FLUENT provides User Defined Function (UDF) that can be loaded with the FLUENT solver to enhance the features that follow the customer's requirement for their specific project. UDF can define customization of initialize condition, boundary condition, source terms, material properties, etc; adjustment of computed values on a once-per-iteration basis; execution at the end of each iteration. UDFs are written in the C programming language and defined using DEFINE macros and other FLUENT-provided functions. One source code file can contain multiple UDFs, like in our case. The values that are passed between the solver and UDF are specified in SI units. Before hooking the UDFs to the solver using a graphical user interface panel, UDFs need to be interpreted or compiled in FLUENT. The major difference between two methods is the interpreted UDFs cannot access the solver data using direct structure references.

In our problem, we need to implement Herschel-Bulkley-Papanastasiou model in numerical simulation cases to avoid the calculation instability. For Herschel-Bulkley fluid model, the discontinuity of the first-order derivative of the velocity at the interface of yielded and unyielded zone leads to numerical instability in CFD. Herschel-Bulkley-Papanastasiou model smoothes this discontinuity and avoid the numerical divergence. FLUENT don't provide this model, so we used the User Defined Function to realize this model in the solver. The apparent viscosity, as shown in Eq. 3.3, is derived from the Herschel-Bulkley-Papanastasiou model, and then implemented in FLUENT. The

apparent viscosity will be calculated on each cell at each iteration step. This is due to the shear stress will change all the time at the entire flow zone in our problem, so do the apparent viscosity.

In Chapter IV, the flow is transient for two phase flow problem. We want to know the relationship between the relative permeability and the gel saturation, so we need to calculate the pressure gradient and the gel saturation at any time. FLUENT can store the data of the pressure gradient at the function of "Surface Monitors", but it only can calculate the total gel volume at the entire zone after computational running. To avoid the effect of inflow and outflow, the entire calculation domain includes an entrance region before the porous media zone and an exit region after the porous media zone. We only want to sum the total volume of the gel in the porous media zone to calculate the gel saturation. Based on these factors, we write a UDF to calculate the saturation at the porous media zone.

The UDF source file is compiled and built a shared library for the resulting objects. The process needs a C program language compiler. The function for calculating the apparent viscosity of Herschel-Bulkley-Papanastasiou model is hooked through "Properties/Viscosity" at the "Create/Edit Materials" dialog box. The function for calculating the gel saturation is hooked through "Adjust" at the "User-Defined Function Hooks" dialog box. The source file has been parallelized to make it can be ran on either serial or parallel computation. The compiled library will be automatically linked to the FLUENT when the case file is read.

The UDF code is shown below:

```
/* UDF for Herschel-Bulkley fluid & calculating saturation */

#include "udf.h"


FILE *fp;


/* ********************************************** */

/* Herschel-Bulkley viscosity */

DEFINE_PROPERTY(hb_viscosity, c, t)

{

 /* Input Parameters for H-B Viscosity */

 real vis;

 real stress;

 real ys;

 real n, m;

 real k;

 real Max, Min;


 n      = 0.7;        /* Power Law Index */

 ys     = 0;          /* Initial Yield Stress */

 k      = 0.1;       /* Fluid Consistency */


 m      = 1000;
```

```
  Max     = 100000;
  Min     = 0.00000000001;

  stress  = C_STRAIN_RATE_MAG(c,t);

/************ Herschel Bulkley Fluid **********/
/* Papanastasion Model */

 vis   = ys*(1-exp(-m*stress))/stress + k*pow(stress,n-1);

  return vis;
}

/* ********************************************** */
/* Calculating Saturation */
DEFINE_ADJUST(saturate, domain)
{
  /* Calculating Parameter */
  real sumSat = 0.0;
  real sumVol = 0.0;
  real sumPre = 0.0;
  real sumAre = 0.0;
```

```
real Sat;

real Pre;

real current_time;

real x[ND_ND];

real area[ND_ND];

int  surface_thread_id = 6;  /******** Changed by Case **********/


current_time = RP_Get_Real("flow-time");


host_to_node_int_1(surface_thread_id);


/* Parameters */

#if !RP_HOST            /* Serial or Node, not Host */

  Thread  *t;

  Thread  *tface;

  Thread  **pt;

  cell_t  c;

  face_t  f;

#endif


/* Main Loop */

#if !RP_HOST            /* Serial or Node */
```

```
thread_loop_c(t, domain)
{
        pt = THREAD_SUB_THREADS(t);

        /*********************       Saturation       ********************/
        begin_c_loop_int(c, t)
        {
            C_CENTROID(x, c, t);
            /******* SC 3.36e-3 10.9455e-3 *******/
            if ( x[0] >= 3.36e-3 && x[0] <= 10.9455e-3)
                {
                        sumSat += C_VOF(c, pt[0])*C_VOLUME(c, t);
                        sumVol += C_VOLUME(c, t);
                 }
        }
        end_c_loop_int(c, t)

        /********************** Pressure **********************/
        tface = Lookup_Thread(domain, surface_thread_id);

        begin_f_loop_int(f, tface)
        {
```

```
                F_AREA(area, f, tface);
                sumPre += F_P(f, tface)*NV_MAG(area);
                sumAre += NV_MAG(area);
        }
        end_f_loop_int(f, tface)

  }
#endif

/* Perform node synchronized actions here Does nothing in Serial */
#if !RP_HOST
  /********************* Saturation **********************/
  sumSat = PRF_GRSUM1(sumSat);
  sumVol = PRF_GRSUM1(sumVol);
  /********************* Pressure  **********************/
  sumPre = PRF_GRSUM1(sumPre);
  sumAre = PRF_GRSUM1(sumAre);
#endif

Sat = sumSat/sumVol;
Pre = sumPre/sumAre;
```

```
/* Pass the node's total Saturate and Pressure to the host for averaging */
/*  #if RP_NODE */
   node_to_host_real_1(Sat);
   node_to_host_real_1(Pre);
/* #endif */

 #if !RP_NODE  /* SERIAL or HOST */
   Message("Saturation: %f Pressure: %f \n", Sat, Pre);
   /* Output to file */
   fp  = fopen("Data.txt","a");
   fprintf(fp,"%f %f %f \n", current_time, Sat, Pre);
   fclose(fp);
 #endif
}
```